# Development of alkali hexatitanate photocatalysts and co-catalysts for photocatalytic reduction of carbon dioxide by water

Xing Zhu

# Development of alkali hexatitanate photocatalysts and co-catalysts for photocatalytic reduction of carbon dioxide by water

**Xing Zhu**

**2020**

**Department of Interdisciplinary Environment**
**Graduate School of Human and Environmental Studies**
**Kyoto University**

# Preface

Global warming, the long-term rise in the average temperature, is dominantly caused by human activities since the Industrial Revolution, which has increased the number of greenhouse gases in the atmosphere, such as $CO_2$, methane, tropospheric ozone, chlorofluorocarbons, and nitrous oxide. Climate model projections summarized in the report indicated that during the 21st century the global surface temperature is likely to rise a further 0.3 to 1.7 °C in a moderate scenario, or as much as 2.6 to 4.8 °C in an extreme situation, depending on the rate of future greenhouse gas emissions. Therefore, it is urgently necessary to reduce $CO_2$ emissions and produce environmental energy.

Photocatalytic $CO_2$ reduction with water using solar energy is the desirable method for not only decreasing $CO_2$ emission, but also producing valuable chemicals that can be used directly as fuels or in further chemical syntheses. Heterogeneous photocatalysis have been studied for the reduction of $CO_2$ with water, and the products reported are formate, CO, $CH_3OH$ and $CH_4$. Among these possible reductive products from $CO_2$, the most useful product would be CO since it is a valuable chemical intermediate for further chemical syntheses and easily detachable from the aqueous reaction media to the gas phase. But, the reduction of protons ($H^+$) to $H_2$ is thermodynamically easier than that of $CO_2$ to CO. Thus, it seems especially challenging to reduce only $CO_2$ molecules selectively in an aqueous solution in principle. Recently, it was discovered that deposited Ag nanoparticles could function as the active cocatalyst for $CO_2$ reduction to form CO. In recent 40 years, many kinds of Ag-modified photocatalysts to produce CO, $H_2$ and $O_2$ have been reported, and although some developed photocatalysts exhibited high activity or high selectivity for the $CO_2$ reduction, the efficiency has not been high enough to put into practice still now.

In the present study, the author focuses on improving the activity and selectivity of photocatalytic reduction of $CO_2$ by $H_2O$ over alkali-metal hexatitanate. Four kinds of hexatitanate photocatalysts were examined and compared in the improved reaction conditions for the photocatalytic reduction of $CO_2$ by water. The effects of preparation methods, preparation conditions, cocatalyst and metal ions doping were investigated to enhance the activity and selectivity for photocatalytic reduction of $CO_2$. Notably, the author found for the first time that deposition of a Ag-Mn dual cocatalyst on a KTO photocatalyst can much improve the photocatalytic $CO_2$ reduction into CO by using $H_2O$ as an electron donor with a very high CO selectivity of 98% among the reductive products, owing to the properties of $MnO_x$ and Ag species for promoting $O_2$ and CO formation, respectively. All above work was carried out at the Graduate School of

Human and Environmental Studies, Kyoto University, Japan from 2017 to 2020 under the supervision of Prof. Hisao Yoshida.

The author expresses her sincere gratitude to Prof. Hisao Yoshida for his wise guidance, valuable suggestions, incisive comments, kind encouragement, careful reviewing of the manuscripts and constant patience throughout the whole work. And the author thanks Dr. Akira Yamamoto, assistant professor, Hisao Yoshida laboratory, Kyoto University, for his grateful guidance and valuable suggestions. The author sincerely thanks to Dr. Shota Imai, Prof. Atsuhiro Tanaka and Hiroshi Kominam at Kindai University for technical assistance with the TEM images in Chapter 4 and 5. The author is gratedful to the valuable comments from Prof. Tomoko Yoshida at Osaka City University, Prof. Tsunehiro Tanaka and Associate Prof. Kentaro Teramura at Kyoto University.

Special thanks to Prof. Setsuhisa Tanabe and Prof. Yoshiharu Uchimoto at the Graduate School of Human and Environmental Studies, Kyoto University, Japan, for their valuable comments to much improve this thesis.

The author thanks to all members, previous and current, of Hisao Yoshida laboratory and Ms, Yuri Bonnticha for her always kind assistance and encouragement. Special thanks to Shuting Li, Akihiko Anzai, Shipei Naniwa, Hitomi Imamura, Akanksha Tyagi, Kirohiro Taizo, Katsunori Isechi, Yoji Ito. The author also thanks to Rui Pang, Shuying Wang, and Zeai Huang at Tsunehiro Tanaka laboratory from Kyoto University.

XAFS measurements in this thesis were performed at NW-10C and BL-12C of the Photon Factory (KEK, Tsukuba, Japan) with approval by PF-PAC (2016G643), the author thanks all the staffs a Photon Factory (KEK, Tsukuba, Japan) for their cooperation and assistance.

Finally, the author sincerely thanks to all the family members and her friends, especially her elder sister (Yan Zhu), parents for their supports, encouragement and understanding for these three years.

Xing ZHU

17th December 2019

Kyoto, Japan

# Contents

# Chapter 1 General introduction

## 1-1 Basic Principle of photocatalytic conversion of $CO_2$ with $H_2O$

Since the 1960s, global warming is an indisputable fact, which has severely affected people's living environment and the development of human society. With the intensification of global warming and the continued growth in energy consumption, people around the world are facing more significant pressure to cut its $CO_2$ emissions down.[1–4] In addition to natural factors, social activities play a significant role in climate warming, especially anthropogenic energy-related $CO_2$ emissions. The excessive consumption of fossil fuels is accompanied by increasing challenges in energy demands and large amounts of anthropogenic $CO_2$ emissions, leading to a shortage of energy and adverse global environmental changes. Developing renewable and clean technologies for energy production has caused widespread concern in recent decades. Among various proposed technologies, since solar power is a theoretically infinite energy source, the solar-driven reduction of $CO_2$ into chemicals and fuels such as formic acid, methane or methanol has been considered as a promising approach to address the problems of global warming and energy crisis.[5]

Many studies have been dedicated to elucidating the mechanism of $CO_2$ reduction. However, most of these studies were conducted in systems utilizing metallic electrodes or homogeneous electrocatalysts. $CO_2$ is one of an extremely stable molecule and chemically inert molecules with a linear geometry, which indicates that a high energy input or appreciate catalyst is needed for the transformation of $CO_2$. Besides, carbon is in its highest oxidation state in $CO_2$ and the reduction of $CO_2$ can lead to a large variety of products with different carbon oxidation states ranging from CO, $CH_4$ to higher hydrocarbons in the gas phase, as well as various oxygenates in the liquid phase such as $CH_3OH$ and HCOOH. The free energy change for the conversion of one $H_2O$ molecule to $H_2$ and $1/2O_2$ under standard conditions is 237 kJ $mol^{-1}$. However, the reduction of $CO_2$ with $H_2O$ into hydrocarbon fuels such as CO, $CH_4$ and $CH_3OH$ is an uphill reaction with a greater positive change in the Gibbs free energy of 270 kJ $mol^{-1}$, 818 kJ $mol^{-1}$ and 702 kJ $mol^{-1}$, respectively, which makes the

**Table 1.** The main products of $CO_2$ and water reduction and the corresponding reduction potentials with reference to NHE at pH=7 in aqueous solution,25 ℃ and 1 atm gas pressure.

| Equation | Reaction | $E^0$ (V *vs.* NHE) |
|---|---|---|
| (1) | $CO_2 + e^- \rightarrow CO_2^{\cdot -}$ | −1.90 |
| (2) | $CO_2 + 2\ H^+ + 2\ e^- \rightarrow HCOOH$ | −0.61 |
| (3) | $CO_2 + 2\ H^+ + 2\ e^- \rightarrow CO + H_2O$ | −0.52 |
| (4) | $CO_2 + 4H^+ + 4\ e^- \rightarrow HCHO + H_2O$ | −0.48 |
| (5) | $CO_2 + 6H^+ + 6\ e^- \rightarrow CH_3OH + H_2O$ | −0.38 |
| (6) | $CO_2 + 8H^+ + 8e^- \rightarrow CH_4 + 2H_2O$ | −0.24 |
| (7) | $2\ H^+ + 2\ e^- \rightarrow H_2$ | −0.41 |

$CO_2$ reduction quite difficult.[6–11] Taken the reduction potential into consideration, the $CO_2$ reduction is more laborious than $H_2O$ splitting, as were shown in Table 1.

Generally, the photocatalytic $CO_2$ reduction reaction with $H_2O$ can be categorized into 4 main steps: (1) $CO_2$ adsorption on the surface of photocatalyst, (2) electron-hole pair generation by absorbing sufficient photon energy, (3) electron-hole pair separation, recombination and their migration to the photocatalyst surface and (4) $CO_2$ reduction with $H_2O$. Typically, the adsorption ability of the photocatalytic toward the $CO_2$ molecule is one of the key aspects to determine its photocatalytic $CO_2$ reduction activity. Here, the introduction of metal or metal oxide co-catalysts onto the surface of photocatalyst can significantly reduce the recombination of the electron-hole pairs or provide active sites for $CO_2$ reduction. [7,12–15] Surface modification of photocatalyst that can offer it with larger specific surface area, more surface active sites is beneficial for improving the $CO_2$ adsorption ability, or inhibit reduction sites of the $H_2$ evolution.[16–20] Moreover, tuning the surface of photocatalyst to be alkaline is also a feasible way to improve its $CO_2$ adsorption ability.[21,22] Finally, the electron-hole pairs migrating to the surface of photocatalyst, with sufficient reduction potential can be utilized for $CO_2$ reduction reactions.

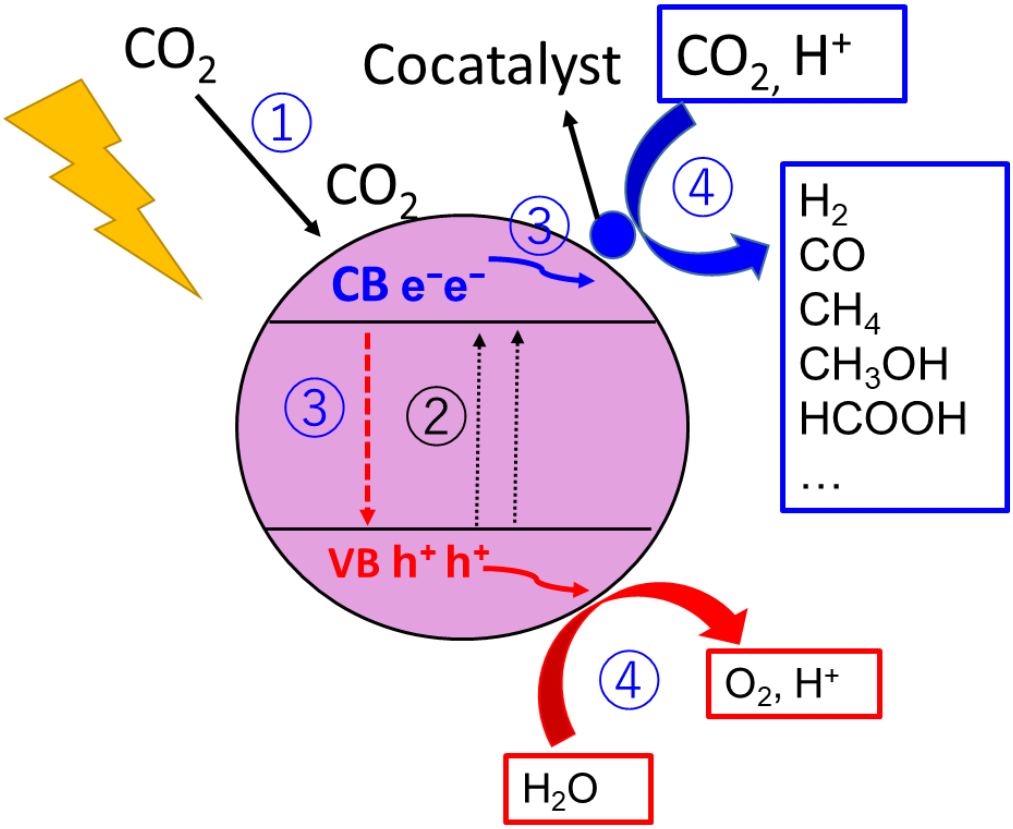


**Fig. 1** Schematic illustration of photocatalytic $CO_2$ reduction with water mechanism over a photocatalyst.

Among these possible reductive products from $CO_2$, CO is the most useful product since it is a valuable chemical intermediate for further chemical syntheses and easily-separable from the aqueous reaction media to the gas phase. In typical reaction systems, it can be assumed that two reactions competitively occur, i.e., the reduction of CO2 and protons with the photoexcited electrons proceed to form CO and H2, respectively on the reductive sites of the photocatalyst surface (Eq. 3 and 7), while the oxidation of water with positive holes into O2 and protons occurs on the oxidative sites (Eq. 8).

$$2\ H_2O + 4\ h^+ \rightarrow O_2 + 4\ H^+ \qquad (8)$$

When no other reductive products than CO and $H_2$ are observed in the reaction system, the selectivity toward CO evolution, $S_{CO}$(%), and the ratio of the consumed electron and hole, R($e^-/h^+$), can be calculated according to Eq. 9 and 10, respectively,[23,24] where the production rate of CO, $H_2$ and $O_2$ are referred to as $R_{CO}$, $R_{H2}$ and $R_{O2}$, respectively. The value of $R(e^-/h^+)$ should be unity if the photocatalytic conversion of $CO_2$ by $H_2O$ proceeds stoichiometrically.

$S_{CO}$ (%) = 100 × $R_{CO}$/ ($R_{CO}$ + $R_{H2}$) (9)

$R(e^-/h^+)$ = ($2R_{CO}$ + $2R_{H2}$)/$4R_{O2}$ (10)

## 1-2 Development of hetergenous photocatalyst for conversion of $CO_2$ into CO by $H_2O$

Although some photocatalysts have been reported for $CO_2$ photoreduction with $H_2O$, most of them suffer from low energy conversion efficiency, low selectivity, instability. The solubility of $CO_2$ in water is very low and the adsorption and activation of $CO_2$ are generally more complicated than that of $H_2O$. The redox potential of $H^+/H_2$ is more positive than that of $CO_2$/CO, so the reduction of protons ($H^+$) to $H_2$ is thermodynamically easier than that of $CO_2$ to CO. Thus, it seems especially challenging to reduce only $CO_2$ molecules selectively in an aqueous solution in principle. Therefore, the design and fabrication of highly active photocatalysts with high conversion efficiency and selectivity for $CO_2$ reduction are significantly necessary. Generally, the solutions to enhance the photocatalytic activity can be categorized into five aspects: (1) suppressing photogenerated carrier recombination; [7] Increasing specific surface areas; [25] Increasing $CO_2$ adsorption and activation; Enhancing photostability;[26,27] Loading appropriate cocatalyst or dual cocatalysts.[14,28,29] In recent decades, numerous efforts have been devoted to improving the efficiency of the surface reactions in $CO_2$ photoreduction, since the photocatalytic conversion of $CO_2$ occurs on the surface of photocatalyst.[15,30–32] Based on these considerations, the activity of photocatalytic conversion of $CO_2$ with water can be improved by following the solutions described below.

### 1-2.1 Effects of Photocatalyst

Generally, oxides or oxide/hydroxide composites containing d0(e.g., $Ti^{4+}$, $Zr^{4+}$, $Ta^{5+}$, and $Nb^{5+}$ oxides) or (e.g., $In^{3+}$, $Ga^{3+}$, and $Ge^{4+}$ oxides) cations are proper candidates for the photocatalytic conversion of $CO_2$ with $H_2O$. As was summarized in Table 2, many new semiconductor types have been investigated and efforts have been widely studied in recent years, such as $BaLa_4Ti_4O_{15}$,[12] $Ga_2O_3$,[14,20,33–35] $KCaSrTa_5O_{15}$,[19] $La_2Ti_2O_7$,[36] $Ag/CaTiO_3$, [24,37] and $Ag/SrNb_2O_6$ [23,38] so on.[39] Although some developed photocatalysts exhibited high activity or high selectivity for the $CO_2$ reduction,[14,20] the efficiency has not been high enough for

the practical application still now. Thus, it is still imperative to develop highly efficient photocatalysts for this reaction. It is noted that, in some cases, the $O_2$ evolution was not always stoichiometric both in water splitting and $CO_2$ reduction. Many reported papers had proposed the possible reasons for the nonstoichiometric formation of $O_2$, such as high overpotential required for $O_2$ evolution and some side reactions.[40,41] It has also been reported that some metal oxides (such as $IrO_2$, $RuO_2$, $CoO_x$, $MnO_x$, etc.) can act as the water oxidation cocatalyst for water splitting but rarely for $CO_2$ reduction so far.[42] Besides, the fabrication methods and conditions are also considered as important factors over the photocatalysts for $CO_2$ reduction with $H_2O$, since the morphology, crystallinity, particle size and surface areas are significant factors in reducing the defects on the surface of photocatalysts, which can decrease the recombination of photogenerated electrons and holes or increasing the functionally active sites. On the other hand, a larger specific surface area of the semiconductor is usually favorable for heterogeneous catalysis since it provides more opportunities for promoting the reaction. Thus, fine single crystals of small size with fewer defects and with a large specific surface area would be ideal for the semiconductor photocatalysts.[37,43,44]

To date, several strategies such as solid state method (SSR) and flux method have been employed to obtain the target photocatalysts. For the SSR method, it is quite challenging to obtain good samples with regular morphology and enough purity, although this method is quite simple and convenient. Flux method (molten salt method) has been studied as a conventional way to obtain large single crystals with uniform particle size, big surface areas, and fewer defects. It was reported that the flux method could enhance the photocatalytic activity for $CO_2$ reduction.[37,40,44] In the present study, the author optimized the preparation condition for examined potassium hexatitanate for the enhancement of $CO_2$ reduction with $H_2O$.

**Table 2.** Reported photocatalytic performances in photocatalytic $CO_2$ reduction with $H_2O$.

| Photocatalyst | Weight of sample (g) | Volume of water (L) | High pressure mercury Lamp (W) | CO evolution activity (μmol $h^{-1}$) | CO selectivity (%) | Ref |
|---|---|---|---|---|---|---|
| $Ag/BaLa_4Ti_4O_{15}$ | 0.3 | 0.36 | 400 | 22 | 67 | [12] |
| $Ba_2Li_{2/3}Ti_{16/3}O_{13}$ | 1.0 | 1.8 | 400 | 1.6 | 12 | [45] |
| $Ag/SrNb_2O_6$ | 0.5 | 1.0 | 400 | 36 | 96 | [23] |
| $Ag/ZnGa_2O_4/Ga_2O_3$ | 1.0 | 1.0 | 400 | 108 | 92 | [32] |
| $Ag/ ZnGa_2O_4$ | 1.0 | 1.0 | 400 | 155 | 95 | [15] |
| $Ag/Na_2Ti_6O_{13}$ | 0.3 | 0.35 | 100 | 2.8 | 82 | [40] |
| $Ag-Mn/K_2Ti_6O_{13}$ | 0.3 | 0.4 | 100 | 10 | 98 | [46] |
| $Ag/NaTaO_3$:Ba | 1.0 | 0.35 | 400 | 318 | 91 | [47] |
| $Ag/La_2Ti_2O_7$ | 0.2 | 1.0 | 400 | 5.2 | 51.4 | [36] |
| $Ag/KCaSrTa_5O_{15}$ | 0.5 | 1.0 | 400 | 97 | 87.6 | [48] |
| $Ag/ZnTa_2O_6$ | 0.5 | 1.0 | 400 | 19.3 | 43.4 | [49] |
| Ag/Mg-Al LDH/$Ga_2O_3$ | 1.0 | 1.0 | 400 | 212 | 61.7 | [30] |
| $Ag-Cr/Ga_2O_3$ | 0.5 | 1.0 | 400 | 480 | 83.8 | [14,50,51] |

## 1-2.2 Effects of Cocatalyst

The redox potential of $H^+/H_2$ is more positive than that of $CO_2/CO$, so the reduction of protons ($H^+$) to $H_2$ is thermodynamically easier than that of $CO_2$ to CO. Thus, it seems especially challenging to reduce only $CO_2$ molecules selectively in an aqueous solution in principle. Therefore, without or with proper cocatalyst always exhibited deficient activity toward CO evolution.[12,45] Deposition of cocatalysts could significantly improve the

performance of semiconductor electrodes for $CO_2$ reduction, where the co-catalysts can function as trapping sites for the electrons or providing active sites, thus promoting the charge separation and altering the selectivity of the products. Pt, NiO, Ru, and Au cocatalysts are highly effective for $H_2$ production by water splitting, and usually appear to be not active for $CO_2$ reduction.[9,52–54] Kudo lab first reported that Ag cocatalyst loaded $BaLa_4Ti_4O_{15}$ exhibited much higher selectivity toward CO evolution for the photocatalytic $CO_2$ reduction using water, which is due to separated reaction sites of reduction from oxidation, and specific loading of the Ag cocatalyst on edge.[12] As for the selectivity toward CO evolution, although it was less than 70% several years ago,[12] Doped $NaTaO_3$ ($NaTaO_3$ : A, where A ¼ Mg, Ca, Sr, Ba, or La) was reported as a highly active photocatalyst for $CO_2$ reduction to simultaneously form CO, $H_2$, and $O_2$ in aqueous solution under UV irradiation when used with a Ag cocatalyst.[47] And it has become higher such as 94% with $Ag/CaTiO_3$[24] and 96% over $Ag/SrNb_2O_6$[23] quite recently. In these years, some dual cocatalysts with proper structures including core-shell type and two separated metal/oxide particles, such as Ag/Cu,[55] $Pt/Cu_2O$,[56] $Ag/CrO_x$,[57] and Cr/Rh[58] have been proved to enhance the activity of $CO_2$ conversion or water splitting by taking advantage of the synergistic function of dual active sites for both reductive and oxidative reactions simultaneously, or the modification of the cocatalyst surface suppressing the backward reaction.[57-59] Recently, a combination of Ag and Mn was examined as a dual cocatalyst deposited on $TiO_2$ photocatalyst to promote CO formation from a mixture of $NaHCO_3$ and $H_2SO_4$ in an aqueous solution although $O_2$ evolution and selectivity toward CO evolution were not clearly mentioned.[60] In this thesis, some different types of dual cocatalysts were also deposited on the surface of KTO photocatalyst and their photocatalytic performance for $CO_2$ reduction was conducted.

### 1-2.3 Effects of surface modification

As mentioned, one of the main aspects limiting the practical application is its wide bandgap and low ability of $CO_2$ adsorption over the surface of photocatalysts. Therefore, extending the light absorption range of photocatalyst and surface modification is highly desirable. $CO_2$ can act as an electron acceptor when the electrophilic C atom interacts with the surface electron centers or Lewis basic sites.[47] Therefore, another surface modification strategy for improving $CO_2$ adsorption and activation is the introduction of basic functional sites on the surface of photocatalysts. Some solid basic hydroxides or oxides such as NaOH, MgO, CaO,

$ZrO_2$ and Ga2O3 can act as electron donors for the interaction with the carbon atom in $CO_2$.[61–63] Ye and co-workers demonstrated that the addition of MgO to the Pt−$TiO_2$ catalyst significantly increased the selectivity for $CO_2$ reduction although the rate of electron consumption for reductive reactions did not change dramatically. The presence of MgO remarkably suppressed the reduction of $H_2O$ to $H_2$ and accelerated the reduction of $CO_2$. The synergistic effect between the enhanced $CO_2$ chemisorption and electron density on the surface of MgO and Pt co-promoted $TiO_2$ is proposed to be responsible for the improvement of the selectivity for $CO_2$ reduction.

They also modified the surface of $TiO_2$ with solid NaOH and demonstrated that NaOH could promote the chemisorption, activation and photoreduction of $CO_2$.[61] Stoichiometric amounts of CO, $H_2$, and $O_2$ were evolved in the photocatalytic conversion of $CO_2$ with $H_2O$ as an electron donor using an Ag-loaded Zn-modified $Ga_2O_3$ photocatalyst. The production of $H_2$ gradually decreased with increasing amounts of Zn species from 0.1 to 10.0 mol%, whereas the evolution of CO was almost unchanged. Consequently, the selectivity toward CO evolution increased to nearly 100%. Therefore, it was demonstrated that the $ZnGa_2O_4$ layer has a particular function to suppress the reduction of $H^+$ in the photocatalytic conversion of $CO_2$ with $H_2O$ over the Ag-loaded Zn-modified $Ga_2O_3$ photocatalyst. Since the generation ratio of $H_2$ to CO can be finely tuned by using the Ag-loaded Zn-modified $Ga_2O_3$ photocatalyst, it is a promising way to produce synthesis gas through the photocatalytic conversion of $CO_2$ with $H_2O$.[32]

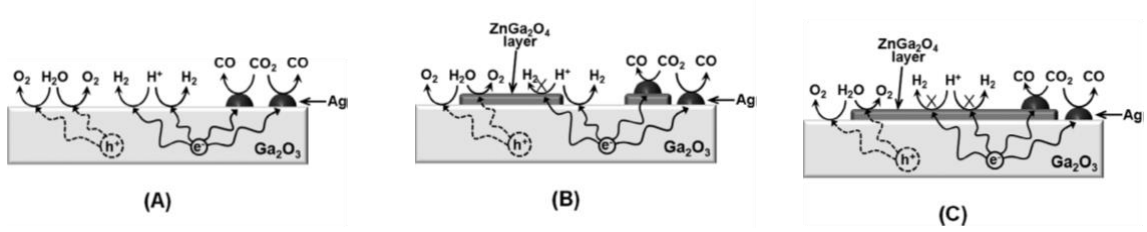


**Fig. 2** A proposed mechanism for the photocatalytic conversion of $CO_2$ in and with $H_2O$ over Ag-loaded $Ga_2O_3$ (A), Ag-loaded Zn modified $Ga_2O_3$ with a low Zn content (B), and Ag-loaded Zn-modified $Ga_2O_3$ with a high Zn content (C).[32]

In this thesis, the different metal ions were added and the performance of prepared samples was also investigated. Here, it should be mentioned that the interface between a photocatalyst and a cocatalyst is also critical for the separation and transportation of charge

carriers18 and the cocatalyst may compete with the underlying photocatalyst for light absorption. Therefore, the photocatalyst/cocatalyst structure should be appropriately designed and engineered to enhance the activity for $CO_2$ photoreduction.

## 1-2.4 Effects of reactor condition

AS compared in Table 2, It may be seen that the formation rate of CO was still low compared to some of those in the current study. Although fair comparison would be difficult due to the quite different reaction conditions such as reactor design, the lamp, light intensity, photocatalyst weight, and so on.

First, the reaction conditions should be taken into account. In these photocatalytic reactions, the formation rate of products profoundly depends on the reaction conditions including reactor design, the employed lamp and so on. We have also confirmed this matter. It is somewhat difficult to explain the correlation between the reaction conditions and the formation rate by a simple equation; for example, the rate cannot be proportional to the amount of photocatalyst and so on. Although we have optimized the photocatalyst under better reaction conditions in the present study than those in our previous study, these are still not comparable to those in other works of literature employing the bigger reactor and the higher intensity of light source. Therefore, it is unfair to compare the absolute values of the photocatalytic activity although we can compare the entire efficiency of the photocatalytic reaction system including the reactor design and the lamp.

Also, the solubility of $CO_2$ in pure $H_2O$ is only about 0.033 mol $L^{-1}$ (at 298 K under 1 atm).[64,65] It is extremely difficult to achieve an efficient photocatalytic conversion of $CO_2$ using $H_2O$ as an electron donor without extra additive. The basic buffer instead of acid additives were entirely necessary to improve the solubility of $CO_2$ on the surface of the photocatalysts for the photocatalytic conversion of $CO_2$ with $H_2O$. It was reported that $NaHCO_3$ could significantly enhance the photocatalytic activity and selectivity toward CO evolution in the conversion of $CO_2$ in aqueous solutions due to the utilization of $CO_2$ were improved considerably.[66,67] The photocatalytic activity toward CO evolution was further enhanced using a solution of ammonia or ammonium bicarbonate as a sacrifice reagent without decreasing the selectivity toward CO evolution.[68]

Additionally, the studied alkali hexatitanate might have originally low photocatalytic activity due to the property. However, the optimized sample achieved a much higher production

rate and higher selectivity to carbon monoxide than those in the previous report after the modification in the current thesis. We believe that these results clarified some critical factors for the photocatalyst design, and these studies would contribute to the development of this field, step by step.

## 1-3 Outline of the present thesis

The present thesis focused on developing high active and selectively photocatalytic conversion of $CO_2$ with $H_2O$ over alkali hexatitanate by optimization of preparation condition, dual cocatalysts and surface modification.

In chapter 2, the silver-loaded sodium titanate photocatalysts, one of which was once reported in the previous study, [44] were again examined in the improved reaction conditions for the photocatalytic reduction of carbon dioxide by water. Two points were claimed in this study. First, after testing the composition of sodium titanate ($Na_2Ti_6O_{13}$ and $Na_2Ti_3O_7$), the performance of the prepared $Ag/Na_2Ti_6O_{13}$ catalysts was much improved by optimizing several conditions such as the flux in a flux method, and the loading method and the loading amount of silver cocatalyst. Second, the reasons for the nonstoichiometric $O_2$ evolution in the initial period were clarified.

In chapter 3, after comparing four types of alkali titanates ($A_2Ti_6O_{13}$, A=Na, K, Rb, Cs), the further development of potassium hexatitanate ($K_2Ti_6O_{13}$, referred to as KTO) photocatalyst prepared in the flux method was examined. The flux method has been extensively investigated to provide fine single crystals of various sizes and morphology, which depends on the synthesis conditions. In this study, KTO samples with rod-like structure were synthesized, and the effects of preparation condition such as the fluxes, the ratio of flux and substrate, and the holding temperature, on both the structure and photocatalytic activity were investigated.

In chapter 4, we examined potassium hexatitanate ($K_2Ti_6O_{13}$, referred to as KTO), which is one of the well-known functional materials with broad applications in many fields. Here, we found for the first time that deposition of a Ag-Mn dual cocatalyst on a KTO photocatalyst can much improve the photocatalytic $CO_2$ reduction into CO by using $H_2O$ as an electron donor with a very high CO selectivity of 98% among the reductive products.

In chapter 5, the different deposition methods for loading dual cocatalysts were investigated to figure out the relationship between the $MnO_x$ and Ag cocatalyst. It was found that the core- shell structure of dual cocatalyst inhibits the activity towards $CO_2$ reduction, and the addition of $MnO_x$ cocatalyst by a simultaneous method keep the small size of Ag cocatalyst, which led to the enhancement of CO evolution.

In chapter 6, a screening tests of potassium hexatitanate modified with various metal ions were synthesized by three different methods and and examined for the $CO_2$ reduction. It was found that modification of $Sn^{4+}$, $Zr^{4+}$ and $Rb^{+}$ ions improved the activity for photocatalytic $CO_2$ reduction selectively to CO by water. Also, some alkaline-earth metals modified KTO samples were prepared and tested, and it was found that tiny addition of $Ca^{2+}$ such as 0.1 mol% could enhanced CO evolution.

## References


1 M. Shahbaz, S. A. Solarin, H. Mahmood and M. Arouri, *Econ. Model.*, 2013, **35**, 145–152.

2 K. Jeong, T. Hong and J. Kim, *Energy Build.*, 2018, **158**, 86–94.

3 B. Guo, Y. Geng, B. Franke, H. Hao, Y. Liu and A. Chiu, *Energy Policy*, 2014, **74**, 134–146.

4 H. Li, H. Mu, M. Zhang and S. Gui, *Energy*, 2012, **39**, 319–326.

5 J. L. White, M. F. Baruch, J. E. Pander, Y. Hu, I. C. Fortmeyer, J. E. Park, T. Zhang, K. Liao, J. Gu, Y. Yan, T. W. Shaw, E. Abelev and A. B. Bocarsly, *Chem. Rev.*, 2015, **115**, 12888–12935.

6 J. L. White, M. F. Baruch, J. E. Pander, Y. Hu, I. C. Fortmeyer, J. E. Park, T. Zhang, K. Liao, J. Gu, Y. Yan, T. W. Shaw, E. Abelev and A. B. Bocarsly, *Chem. Rev.*, 2015, **115**, 12888–12935.

7 J. Low, J. Yu and W. Ho, *J. Phys. Chem. Lett.*, 2015, **6**, 4244–4251.

8 X. Chang, T. Wang and J. Gong, *Energy Environ. Sci.*, 2016, **9**, 2177–2196.

9 K. Li, X. An, K. H. Park, M. Khraisheh and J. Tang, *Catal. Today*, 2014, **224**, 3–12.

10 W. Taifan, J. F. Boily and J. Baltrusaitis, *Surf. Sci. Rep.*, 2016, **71**, 595–671.

11 J. Low, B. Cheng and J. Yu, *Appl. Surf. Sci.*, 2017, **392**, 658–686.

12 K. Iizuka, T. Wato, Y. Miseki, K. Saito and A. Kudo, *J. Am. Chem. Soc.*, 2011, **133**, 20863–

20868.

13 J. Low, B. Cheng, J. Yu and M. Jaroniec, *Energy Storage Mater.*, 2016, **3**, 24–35.

14 R. Pang, K. Teramura, H. Tatsumi, H. Asakura, S. Hosokawa and T. Tanaka, *Chem. Commun.*, 2018, **54**, 1053–1056.

15 Z. Wang, K. Teramura, S. Hosokawa and T. Tanaka, *J. Mater. Chem. A*, 2015, **3**, 11313–11319.

16 L. Mino, G. Spoto and A. M. Ferrari, *J. Phys. Chem. C*, 2014, **118**, 25016–25026.

17 X. Li, H. Liu, D. Luo, J. Li, Y. Huang, H. Li, Y. Fang, Y. Xu and L. Zhu, *Chem. Eng. J.*, 2012, **180**, 151–158.

18 K. Kočí, L. Obalová, L. Matějová, D. Plachá, Z. Lacný, J. Jirkovský and O. Šolcová, *Appl. Catal. B Environ.*, 2009, **89**, 494–502.

19 Z. Huang, K. Teramura, H. Asakura, S. Hosokawa and T. Tanaka, *Catal. Today*, 2018, **300**, 173–182.

20 H. Tatsumi, K. Teramura, Z. Huang, Z. Wang, H. Asakura, S. Hosokawa and T. Tanaka, *Langmuir*, 2017, **33**, 13929–13935.

21 J. Kapica-Kozar, E. Kusiak-Nejman, A. Wanag, Ł. Kowalczyk, R. J. Wrobel, S. Mozia and A. W. Morawski, *Microporous Mesoporous Mater.*, 2015, **202**, 241–249.

22 V. Kempter, S. Krischok and O. H, *Surf. Sci.*, 2002, **510**, 69–73.

23 R. Pang, K. Teramura, H. Asakura, S. Hosokawa and T. Tanaka, *Appl. Catal. B Environ.*, 2017, **218**, 770–778.

24 A. Anzai, N. Fukuo, A. Yamamoto and H. Yoshida, *Catal. Commun.*, 2017, **100**, 134–138.

25 Y. Sun, Q. Wu and G. Shi, *Energy Environ. Sci.*, 2011, **4**, 1113–1132.

26 Y. Tang, X. Hu and C. Liu, *Phys. Chem. Chem. Phys.*, 2014, **16**, 25321–25329.

27 J. Yu, J. Jin, B. Cheng and M. Jaroniec, *J. Mater. Chem. A*, 2014, **2**, 3407–3416.

28 R. Li, H. Han, F. Zhang, D. Wang and C. Li, *Energy Environ. Sci.*, 2014, **7**, 1369–1376.

29 R. Li, F. Zhang, D. Wang, J. Yang, M. Li, J. Zhu, X. Zhou, H. Han and C. Li, *Nat. Commun.*, 2013, **4**, 1432–1437.

30 S. Iguchi, Y. Hasegawa, K. Teramura, S. Kidera, S. Kikkawa, S. Hosokawa, H. Asakura and T. Tanaka, *Sustain. Energy Fuels*, 2017, **1**, 1740–1747.

31 Z. Huang, S. Yoshizawa, K. Teramura, H. Asakura, S. Hosokawa and T. Tanaka, *ACS Omega*, 2017, **2**, 8187–8197.

32 Z. Wang, K. Teramura, Z. Huang, S. Hosokawa, Y. Sakata and T. Tanaka, *Catal. Sci. Technol.*, 2016, **6**, 1025–1032.

33 Y. X. Pan, Z. Q. Sun, H. P. Cong, Y. L. Men, S. Xin, J. Song and S. H. Yu, *Nano Res.*, 2016, **9**, 1689–1700.

34 Y. Kawaguchi, M. Akatsuka, M. Yamamoto, K. Yoshioka, A. Ozawa, Y. Kato and T. Yoshida, *J. Photochem. Photobiol. A Chem.*, 2018, **358**, 459–464.

35 T. Yoshida, N. Yamamoto, T. Mizutani, M. Yamamoto, S. Ogawa, S. Yagi, H. Nameki and H. Yoshida, *Catal. Today*, 2018, **303**, 320–326.

36 Z. Wang, K. Teramura, S. Hosokawa and T. Tanaka, *Appl. Catal. B Environ.*, 2015, **163**, 241–247.

37 H. Yoshida, L. Zhang, M. Sato, T. Morikawa, T. Kajino, T. Sekito, S. Matsumoto and H. Hirata, *Catal. Today*, 2015, **251**, 132–139.

38 S. Xie, Y. Wang, Q. Zhang, W. Deng and Y. Wang, *Chem. Commun.*, 2015, **51**, 3430–3433.

39 T. Takayama, K. Tanabe, K. Saito, A. Iwase and A. Kudo, *Phys. Chem. Chem. Phys.*, 2014, **16**, 24417–24422.

40 X. Zhu, A. Anzai, A. Yamamoto and H. Yoshida, *Appl. Catal. B Environ.*, 2019, **243**, 47–56.

41 Y. F. Li, Z. P. Liu, L. Liu and W. Gao, *J. Am. Chem. Soc.*, 2010, **132**, 13008–13015.

42 A. Kudo and Y. Miseki, *Chem. Soc. Rev.*, 2009, **38**, 253–278.

43 H. Yoshida, M. Takeuchi, M. Sato, L. Zhang, T. Teshima and M. G. Chaskar, *Catal. Today*, 2014, **232**, 158–164.

44 H. Yoshida, M. Sato, N. Fukuo, L. Zhang, T. Yoshida, Y. Yamamoto, T. Morikawa, T. Kajino, M. Sakano, T. Sekito, S. Matsumoto and H. Hirata, *Catal. Today*, 2018, **303**, 296–304.

45 L. F. Garay-Rodríguez, H. Yoshida and L. M. Torres-Martínez, *Dalt. Trans.*, 2019, **48**, 12105–12115.

46 X. ZHU, A. Yamamoto, S. Imai, A. Tanaka, H. Kominami and H. Yoshida, *Chem. Commun.*, 2019, **55**, 13514.

47 H. Nakanishi, K. Iizuka, T. Takayama, A. Iwase and A. Kudo, *ChemSusChem*, 2017, **10**, 112–118.

48 T. Takayama, A. Iwase and A. Kudo, *Bull. Chem. Soc. Jpn.*, 2015, **88**, 538–543.

49 S. Iguchi, K. Teramura, S. Hosokawa and T. Tanaka, *Catal. Sci. Technol.*, 2016, **6**, 4978–4985.

50 R. Pang, K. Teramura, H. Asakura, S. Hosokawa and T. Tanaka, *J. Phys. Chem. C*, 2019, **123**, 2894–2899.

51 R. Pang, K. Teramura, H. Asakura, S. Hosokawa and T. Tanaka, *ACS Sustain. Chem. Eng.*, 2019, **7**, 2083–2090.

52 G. Zhao, X. Huang, X. Wang and X. Wang, *J. Mater. Chem. A*, 2017, **5**, 21625–21649.

53 J. Yu, K. Wang, W. Xiao and B. Cheng, *Phys. Chem. Chem. Phys.*, 2014, **16**, 11492–11501.

54 W. Fan, Q. Zhang and Y. Wang, *Phys. Chem. Chem. Phys.*, 2013, **15**, 2632–2649.

55 Z. Chang, S. Huo, W. Zhang, J. Fang and H. Wang, *J. Phys. Chem. C*, 2017, **121**, 11368–11379.

56 Q. Zhai, S. Xie, W. Fan, Q. Zhang, Y. Wang, W. Deng and Y. Wang, *Angew. Chemie - Int. Ed.*, 2013, **52**, 5776–5779.

57 R. Pang, K. Teramura, H. Tatsumi, H. Asakura, S. Hosokawa and T. Tanaka, *Chem. Commun.*, 2018, **54**, 1053–1056.

58 K. Maeda, A. Xiong, T. Yoshinaga, T. Ikeda, N. Sakamoto, T. Hisatomi, M. Takashima, D. Lu, M. Kanehara, T. Setoyama, T. Teranishi and K. Domen, *Angew. Chemie - Int. Ed.*, 2010, **49**, 4096–4099.

59 J. Zhu, S. Pang, T. Dittrich, Y. Gao, W. Nie, J. Cui, R. Chen, H. An, F. Fan and C. Li, *Nano Lett.*, 2017, **17**, 6735–6741.

60 Z. Jiang, D. Ding, L. Wang, Y. Zhang and L. Zan, *Catal. Sci. Technol.*, 2017, **7**, 3065–3072.

61 X. Meng, S. Ouyang, T. Kako, P. Li, Q. Yu, T. Wang and J. Ye, *Chem. Commun.*, 2014, **50**, 11517–11519.

62 S. Xie, Y. Wang, Q. Zhang, W. Fan, W. Deng and Y. Wang, *Chem. Commun.*, 2013, **49**, 2451–2453.

63 S. Xie, Y. Wang, Q. Zhang, W. Deng and Y. Wang, *ACS Catal.*, 2014, **4**, 3644–3653.

64 D. A. Palmer and R. Van Eldik, *Chem. Rev.*, 1983, **83**, 651–731.

65 M. Watanabe, A. Kudo and T. Sakata, *J. Electrochem. Soc.*, 1995, **142**, L57–L59.

66 Z. Huang, K. Teramura, H. Asakura, S. Hosokawa and T. Tanaka, *J. Mater. Chem. A*, 2017, **5**, 19351–19357.

67 R. Pang, K. Teramura, H. Asakura, S. Hosokawa and T. Tanaka, *ACS Appl. Energy Mater.*, 2019, **2**, 5397–5405.

68 Z. Huang, S. Yoshizawa, K. Teramura, H. Asakura, S. Hosokawa and T. Tanaka, *ACS Sustain. Chem. Eng.*, 2018, **6**, 8247–8255.

# Chapter 2 Silver-loaded sodium titanate photocatalysts for selective reduction of carbon dioxide to carbon monoxide with water


## Abstract

To obtain more efficient photocatalyst for photocatalytic reduction of $CO_2$ with $H_2O$ and figure out the reason for nonstoichiometric $O_2$ evolution, silver-loaded sodium titanate photocatalysts were further studied in the improved reaction conditions. After preliminary tests for two kinds of sodium titanate samples with different ratio of sodium to titanium ($Na_2Ti_6O_{13}$ and $Na_2Ti_3O_7$), several sodium hexatitanate ($Na_2Ti_6O_{13}$) photocatalysts were further prepared in the flux method by changing the parameters such as the flux, the loading amount of Ag cocatalyst, and the loading method of the Ag cocatalyst. As a result, a Ag/$Na_2Ti_6O_{13}$ sample prepared in a sodium chloride flux, with 1.0 wt% of Ag cocatalyst loaded by a photodeposition method, exhibited the highest production rate (4.6 μmol $h^{-1}$) and the highest selectivity (74%) to carbon monoxide among the examined samples, which are more than 29 times higher production rate and 2.7 times higher selectivity to carbon monoxide than those in the previous report. Furthermore, although required oxygen production rate equivalent to the formation rates of the reduced products was not observed in the previous study, it was found that the developed Ag/$Na_2Ti_6O_{13}$(NaCl) photocatalyst produced enough amount of oxygen after a long induction period of 50 h in the present condition. The reasons for the insufficient oxygen formation in the initial period were also investigated and clarified, i.e., the chloride residues and the photoadsorption of $O_2$ on the surface are responsible for the insufficient $O_2$ evolution at the initial period.


## 2-1 Introduction

Photocatalytic $CO_2$ reduction with water using solar energy is the desirable method for not only decreasing $CO_2$ emission, but also producing valuable chemicals that can be used directly as fuels or in further chemical syntheses. [1–5] Heterogeneous photocatalysis have been studied for the reduction of $CO_2$ with water, and the products reported are formate, CO, $CH_3OH$ and $CH_4$. [6–14] Among these possible reductive products from $CO_2$, CO is the most useful product since it is a valuable chemical intermediate for further chemical syntheses and easily-separable

from the aqueous reaction media to the gas phase. To obtain CO as a product, Ag cocatalyst was discovered, [15] which has been widely studied in recent years, such as $Ag/BaLa_4Ti_4O_{15}$, [15] $Ag/Ga_2O_3$, [16–20] $Ag/KCaSrTa_5O_{15}$, [21] $Ag/La_2Ti_2O_7$, [22] $Ag/CaTiO_3$, [23,24] and $Ag/SrNb_2O_6$. [25,26] However, the photocatalytic activity has not been enough for the practical application. Thus, it is still imperative to develop highly efficient photocatalysts for this reaction.

In these reaction systems, it can be assumed that two reactions competitively occur, i.e., photocatalytic reduction of $CO_2$ to form CO and $O_2$ (Eq. 1) and photocatalytic water splitting into $H_2$ and $O_2$ (Eq. 2). In details, the reduction of $CO_2$ and protons with the photoexcited electrons proceed to form CO and $H_2$, respectively on the reductive sites of the photocatalyst surface (Eqs. 3 and 4), while the oxidation of water with positive holes into $O_2$ and protons occurs on the oxidative sites (Eq. 5).

$$CO_2 \rightarrow CO + 1/2\ O_2 \quad (1)$$

$$H_2O \rightarrow H_2 + 1/2\ O_2 \quad (2)$$

$$CO_2 + 2\ H^+ + 2\ e^- \rightarrow CO + H_2O \quad (3)$$

$$2\ H^+ + 2\ e^- \rightarrow H_2 \quad (4)$$

$$2\ H_2O + 4\ h^+ \rightarrow O_2 + 4\ H^+ \quad (5)$$

When no other reductive products than CO and $H_2$ are observed in the reaction system, the selectivity toward CO evolution, $S_{CO}$(%), and the ratio of the consumed electron and hole, $R(e^-/h^+)$, can be calculated according to Eqs. 6 and 7, respectively, [24,26] where the production rate of CO, $H_2$ and $O_2$ are referred to as $R_{CO}$, $R_{H2}$ and $R_{O2}$, respectively. The value of $R(e^-/h^+)$ should be unity if the two competitive reactions, Eqs. 1 and 2, take place ideally in any balance.

$$S_{CO}\ (\%) = 100 \times R_{CO} / (R_{CO} + R_{H2}) \quad (6)$$

$$R(e^-/h^+) = (2R_{CO} + 2R_{H2})/4R_{O2} \quad (7)$$

In my previous study, [27] we focused on sodium hexatitanate ($Na_2Ti_6O_{13}$) since titanium and sodium are abundant elements in the Earth's crust. The sodium hexatitanate samples were prepared by a flux method, on which Ag cocatalyst was loaded. The $Ag/Na_2Ti_6O_{13}$ photocatalyst exhibited the photocatalytic activity for the $CO_2$ reduction to CO. The photocatalyst consisted of unique rod-like fine crystal particles showing facets, and the Ag cocatalyst nanoparticles were deposited on the selected facets, especially after the

photocatalytic reaction test. In this system, however, two problems remained; one was the low activity of CO evolution with low selectivity, such as $R_{CO}$=0.16 μmol $h^{-1}$ and $S_{CO}$=27%, and the other was the uncertainty of the oxidation reaction, i.e., insufficient oxygen evolution, $R(e^-/h^+)$<1. As for the former problem, the reaction conditions should be reconsidered since we found recently that the reaction conditions, such as light intensity and $CO_2$ concentration in the reaction mixture, much affect the production rates of carbon monoxide and oxygen. [24] As for the latter problem, so far, many photocatalytic systems have faced this problem, i.e., the ratio of the consumed electron and hole $R(e^-/h^+)$ estimated from the production rates was not unity, which is not consistent to the stoichiometric ratio. Among the proposed explanations, the most convinced one would be that the difficulty of water oxidation is due to the high overpotential of $O_2$ evolution, which originates from charge trapping by surface states and slow oxygen evolution kinetics. [28–30] This is also an explanation why some photocatalytic systems for water splitting produce $H_2$ without sufficient amount of $O_2$ (or $R_{H2}/R_{O2}$>2). [31] In addition, photoadsorption of $O_2$ on the photocatalyst surface [32,33] and the competitive oxidation of water to hydrogen peroxide [34,35] are also possible in the photocatalytic reaction with water. What's more, for some special reaction systems using catalyst samples containing chloride residues originated from the catalyst preparation, such as a flux method with chloride flux, the residues of chloride may compete with oxygen evolution. Some researchers suggested that the $Cl^-$ that exists in the photocatalytic system can react with the photogenerated holes. [36,37] Li and co-workers claimed that the existence of $Cl^-$ affected both the $H_2$ evolution and $O_2$ evolution. [38] Furthermore, Iguchi et al. also reported that hypochlorous acid (HClO) was produced as an oxidation product of $Cl^-$ with the formation of reduction products such as CO and $H_2$ under photoirradiation. [39]

Thus, in the present study, the silver-loaded sodium titanate photocatalysts, one of which was once reported in the previous study, [27] were again examined in the improved reaction conditions for the photocatalytic reduction of carbon dioxide by water. Two points were claimed in this study. First, after testing the composition of sodium titanate ($Na_2Ti_6O_{13}$ and $Na_2Ti_3O_7$), the performance of the prepared Ag/$Na_2Ti_6O_{13}$ catalysts were much improved by optimizing several conditions such as the flux in a flux method, and the loading method and the loading amount of silver cocatalyst. Second, the reasons for the nonstoichiometric $O_2$ evolution in the initial period were clarified.

## 2-2 Experimental

### 2-2.1 Sample preparation

The $Na_2Ti_3O_7$ sample was prepared by a solid state reaction (SSR) method reported in the literature. [40,41] The precursors ($Na_2CO_3$ (Kishida): $TiO_2$ (rutile, Kojundo)=1:3) were mixed for 30 minutes in an alumina mortar and calcined at 1073 K for 20 h, followed by additional grinding at room temperature and heating at 1073 K for another 20 h. Although it was examined to prepare another $Na_2Ti_3O_7$ sample by a flux method, no sample showing XRD patterns was obtained.

For the preparation of another $Na_2Ti_6O_{13}$ sample in the SSR method, the precursors were mixed for 30 minutes in an alumina mortar, where the molar ratio of $Na_2CO_3$ to $TiO_2$ was 1:6. The mixture was put into an alumina crucible, heated in an electric muffle furnace with a rate of 200 K $h^{-1}$ to 1273 K, held at this temperature for 10 h, and then cooled at a rate of −100 K $h^{-1}$ to 773 K, followed by being naturally cooled to room temperature in the furnace. This sample is referred to as NTO(SSR). Several $Na_2Ti_6O_{13}$ samples were prepared also in a flux method.[27] The precursors, $Na_2CO_3$ and $TiO_2$, and a flux reagent such as NaCl, NaF, NaBr, NaI (Nacalai Tesque), or KCl (Kishida, were mixed for 20 minutes in an alumina mortar and heated in the same temperature program as mentioned above, and the solute ($Na_2Ti_6O_{13}$) to the flux in the molten mixture was 1:1. The obtained powder was thoroughly washed with hot water (353 K) for 15 minutes and filtrated, and this washing step was repeated 3 times to remove the remained residual salt, then dried at 323 K for 24 hours. The $Na_2Ti_6O_{13}$ samples prepared by different fluxes are referred to as NTO(*flux*) such as NTO(*NaCl*).

Ag cocatalyst was loaded on the sodium titanate samples by a photodeposition method (PD), a chemical reduction method (CR), or an impregnation method (IMP). In the PD method, 1 g of the $Na_2Ti_3O_7$ or $Na_2Ti_6O_{13}$ sample in 150 mL of ion-exchanged water was irradiated using a 300 W xenon lamp (PE300BUV) for 30 minutes with magnetically stirring. Then 50 mL of $CH_3OH$ and a required amount of $AgNO_3$ were added and the suspension was stirred for 30 minutes without irradiation. Based on the loading amount of Ag over different samples, it was irradiated for 2-6 hours, where the light intensity was measured to be 22 mW $cm^{-2}$ at 254 ± 10 nm in wavelength. The obtained suspension was filtrated and washed by hot water (353K) 3 times, and dried at 323 K for 24 hours. In the CR method, the $Na_2Ti_6O_{13}$ sample (1g) was

suspended in 50 mL of an aqueous solution of $AgNO_3$ (0.295 M), followed by the dropwise addition of an aqueous $NaPH_2O_2$ solution (0.295 M, 315 μL) into the suspension. After stirring the mixture at 353 K for 2 h, it was washed by ion-exchanged water, and it was filtered and dried at room temperature. In the IMP method, 1 g of the $Na_2Ti_6O_{13}$ sample was suspended in 100 mL of ion exchange water with the desired amount of $AgNO_3$, followed by evaporation at 353 K to remove water, drying for 24 h at 373 K, and calcination at 723 K for 2 h in air. The Ag-loaded NTO(*NaCl*) samples are referred to as Ag/NTO(*NaCl*,PD), Ag/NTO(*NaCl*,CR), and Ag/NTO(*NaCl*,IMP).

### 2-2.2 Characterization

The loading amount of Ag on the samples was evaluated by X-ray fluorescence analysis with an EDX-8000 (Shimadzu) using an experimentally obtained calibration curve. The crystal structure of the samples was determined by powder X-ray diffraction with a Lab X XRD-6000 (Shimazu). Morphologies of the samples were observed by scanning electron microscopy (SEM) image with a JSM-890 (JEOL). Diffuse reflectance (DR) UV-Vis spectrum was recorded by a V-670 (JASCO). The bandgap was estimated according to the Davis–Mott equation using the Kubelka–Munk function F(R∞) obtained from the diffuse-reflectance spectrum.[42] The Brunauer–Emmett–Teller (BET) specific surface area was calculated from the amount of $N_2$ adsorption at 77 K, which was measured by a Monosorb (Quantachrome).

### 2-2.3 Photocatalytic reaction test

The photocatalytic activity tests of $CO_2$ reduction with water were carried out using a bubbling-flow system with an inner-irradiation-type reaction vessel,[24] which were the most different points of the reaction conditions from those in the previous study.[27] The Ag-loaded sodium titanate sample (0.2 g) was dispersed in ion-exchanged water (350 mL) containing 0.5 M $NaHCO_3$ by magnetically stirring. Then, $CO_2$ was bubbled into the solution at a flow rate of 15 mL $min^{-1}$ without irradiation for 1.5 hours. The photocatalytic reaction was conducted using a 100 W high-pressure mercury lamp with 44 mW $cm^{-2}$ measured at 254 ± 10 nm in wavelength. The reaction temperature was 290 K. The evolution rate of the products (CO, $H_2$, and $O_2$) in the outlet from the reactor were determined by using an on-line gas chromatograph (Shimadzu, GC-8A, TCD, Shincarbon ST column, argon carrier).

### 2-2.4 Evaluation of oxidative byproducts in aqueous solution

To know whether hydrogen peroxide ($H_2O_2$) was formed or not, the aqueous solution after the

photocatalytic reaction test was sampled and the conventional starch-iodine test was examined using KI reagent and starch. Assuming that all photoformed holes were consumed to produce $H_2O_2$ in this system, the equivalent $H_2O_2$ reagent (31.9 μmol $L^{-1}$) was prepared and used as a reference.

To confirm the formation of hypochlorous acid (HClO) in the aqueous solutions after the photocatalytic reactions, a conventional DPD test was employed.[39,43,44] When the *N*-*N*-diethyl-*p*-phenylenediamine (DPD) reagent is added to a solution containing HClO, a red oxidant of DPD rapidly formed through the stoichiometric reaction. The DPD solution was prepared by dissolving 0.1 g of the DPD reagent (Wako), which is a mixture of DPD sulfate and $Na_2SO_4$, in 5.0 mL of a phosphate buffer solution (pH = 6.5). 1.0 mL of the prepared DPD solution was added to 5.0 mL of the sample solution, and was shaken for 20 s. The transmittance spectrum was measured immediately using a UV-vis spectrometer (JASCO V-670) in a transmission mode.

## 2-3 Results and discussions

### 2-3.1 Sodium titanates

Two types of sodium titanates, sodium trititanate ($Na_2Ti_3O_7$) and sodium hexatitanate ($Na_2Ti_6O_{13}$), were fabricated. Fig. 1 shows XRD patterns of the obtained samples with those from the database (ICSD#15463 for $Na_2Ti_3O_7$ [45] and ICSD#23877 for $Na_2Ti_6O_{13}$ [46]) as references. The patterns of the $Na_2Ti_3O_7$(SSR) sample and the $Na_2Ti_6O_{13}$ samples (Fig. 1a, 1b, and 1c) were consistent with the reference data, respectively. Since no diffraction lines corresponding to other impurity phases were observed, it was confirmed that two types of pure sodium titanates, $Na_2Ti_3O_7$ and $Na_2Ti_6O_{13}$, were correctly fabricated. It is noted that the distribution of the diffraction line intensity of the NTO(*NaCl*) sample prepared with the NaCl flux are different from that of the NTO(*SSR*) sample and the reference. And the intensities of some diffraction lines were also quite different, for example, the intensity of the line at 11.86° corresponding to (200) plane in the pattern of the NTO(*NaCl*) sample was much higher than that for the others, implying that the $Na_2Ti_6O_{13}$ crystals prepared by the flux method have an anisotropic morphology.

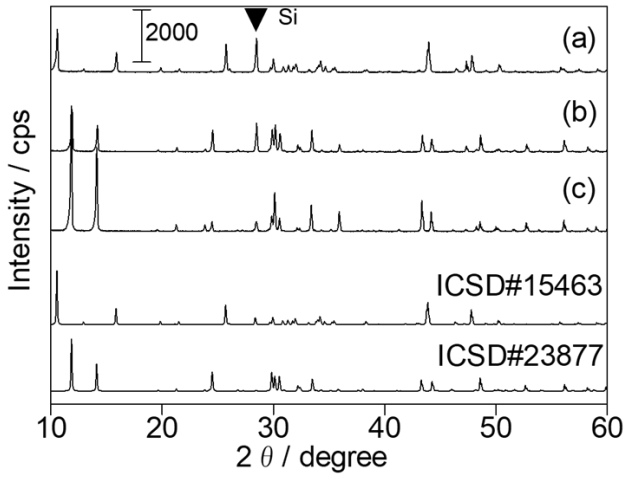


**Fig. 1** XRD patterns of the samples; (a) the $Na_2Ti_3O_7$(*SSR*) sample, (b) the NTO(*SSR*) sample, and (c) the NTO(*NaCl*) sample. Silicon powder mixed to calibrate the angle showed a diffraction indicated by a closed triangle. The patterns from the ICSD database are also shown, ICSD#15463 for $Na_2Ti_3O_7$ and ICSD#23877 for $Na_2Ti_6O_{13}$.

Fig. 2 shows the SEM images. The $Na_2Ti_3O_7$(*SSR*) sample consisted of small roundish rod-like or roundish particles with almost uniformed size less than 1 μm (Fig. 2a), while the NTO(*SSR*) sample showed more irregular shape of particles, most of which were smaller than 1 μm but some of which were much larger (Fig. 2b). On the other hand, the NTO(*NaCl*) sample consisted of anisotropic rod-like crystal structure covered with facets and crystal size was larger than 2 μm (Fig. 2c). This confirms that the molten salt can enhance the crystallization and regulate the crystal growth of each facet to form the unique morphology. It is known that this effect depends on the property of the cation such as $Na^+$, $K^+$ in the molten flux.[27]

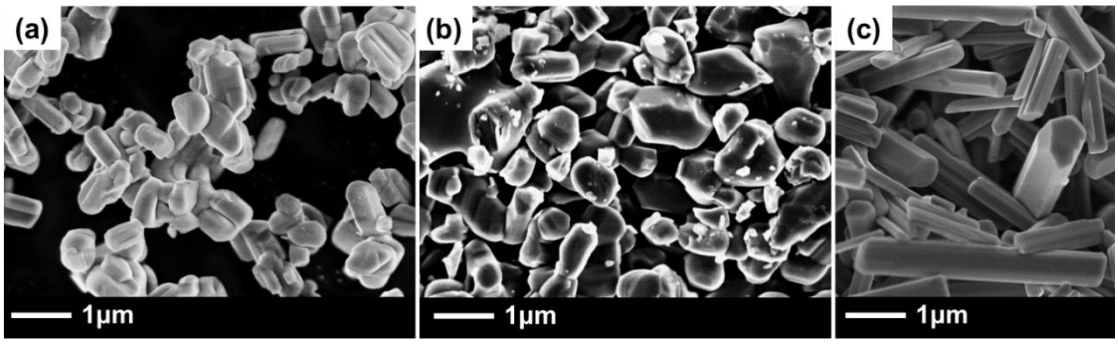


**Fig. 2** SEM images of the prepared samples; (a) the $Na_2Ti_3O_7$ (*SSR*) sample, (b) the NTO (*SSR*) sample, and (c) the NTO (*NaCl*) sample.

As shown in Table 1, the specific surface areas of the $Na_2Ti_3O_7$(*SSR*) sample, the NTO(*SSR*) sample and the NTO (*NaCl*) sample were measured to be 2.58, 3.91, and 5.17 $m^2g^{-1}$, respectively. Furthermore, Fig. 3A shows DR UV–visible spectra of these samples, which give information for the electronic band structure. The $Na_2Ti_3O_7$(*SSR*) sample showed an absorption band less than 320 nm in wavelength, while the NTO(SSR) and NTO(*NaCl*) samples showed the absorption edge at 350.7 nm and 351.2 nm, respectively. The estimated bandgap for the $Na_2Ti_3O_7$(*SSR*) sample was 3.88 eV, which was slightly bigger than 3.54 eV for the NTO(SSR) sample and 3.53 eV for the NTO(*NaCl*) sample.

**Table 1** Properties of the prepared $Na_2Ti_3O_7$ and $Na_2Ti_6O_{13}$ samples.

| Entry | Sample | Preparation method | Crystal phase[a] | Specific surface area[b] / $m^2$ $g^{-1}$ | Bandgap[c] / eV | Loading amount of Ag[d] (wt%) |
|---|---|---|---|---|---|---|
| 1 | $Na_2Ti_3O_7$(SSR) | SSR | $Na_2Ti_3O_7$ | 2.58 | 3.88 | 0.99 |
| 2 | NTO(SSR) | SSR | $Na_2Ti_6O_{13}$ | 3.91 | 3.54 | 0.99 |
| 3 | NTO(NaCl) | Flux method | $Na_2Ti_6O_{13}$ | 5.17 | 3.53 | 0.93 |

[a] Estimated by X-ray diffraction at 10–80 degree. [b] Estimated by BET method. [c] Estimated from DR UV-vis spectra. [d] Estimated by XRF measurements.

XRF measurements confirmed the loading amount of the Ag cocatalyst on these three samples by the PD method to be almost 1 wt% of Ag cocatalyst on each sample as expected (Table 1). In the DR UV-vis spectra of the Ag-loaded samples (Fig. 3B), the surface plasmon resonance (SPR) band of the Ag nanoparticles was similarly observed for the Ag/NTO(*SSR*) sample and the Ag/NTO(*NaCl*) sample, while no such band was observed for the Ag/$Na_2Ti_3O_7$ sample. This difference would originate from the state of the Ag species added on the sodium titanate samples. For the Ag/$Na_2Ti_3O_7$ sample, the bandgap was shifted from 3.88 eV to 3.49 eV, where the $Ag^+$ cations could be easy inserted and exchange to the $Na^+$ between the titanate layered structure of the $Na_2Ti_3O_7$ sample. This indicated that Ag nanoparticles exist only on the NTO samples.

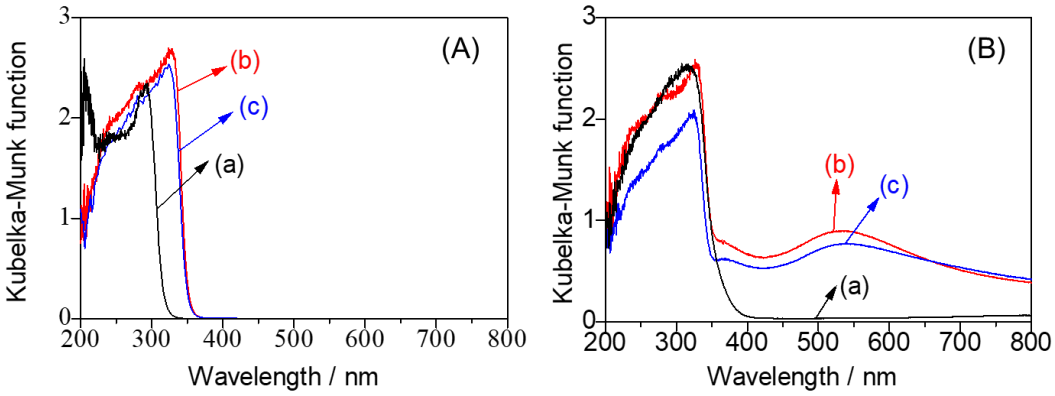


**Fig. 3** DR UV–visible spectra of the prepared samples loaded without (A) and with 1 wt% Ag cocatalyst (B), the $Na_2Ti_3O_7$(*SSR*) sample (a), the NTO(*SSR*) sample (b), and the NTO(*NaCl*) sample (c). Ag cocatalyst was loaded by the PD method.

Fig. 4 shows the results of the photocatalytic reaction tests, i.e., the time course of the formation rates of the products and the selectivity toward CO evolution ($S_{CO}$) in the photocatalytic conversion of $CO_2$ with water over the three Ag-loaded samples. The three samples exhibited the photocatalytic activity to produce CO, $O_2$ and $H_2$. First, when compared the two samples prepared by the SSR method, the Ag/$Na_2Ti_3O_7$(*SSR*) and Ag/NTO(SSR) samples (Figs. 4a and 4b), the most obvious difference between them was the product selectivity, i.e., the former exhibited high selectivity to form $H_2$ and the latter predominantly produced CO with high selectivity such as $S_{CO}$=75–90%. These samples have some different properties such as compositions, crystal structures, band structure and also the state of the Ag cocatalyst. Especially, the former exhibited no obvious SPR band while the latter clearly showed, suggesting the Ag species exist as a dispersed or oxidized form in the former sample and as nanoparticles in the latter sample. Considering the well-known function of the Ag nanoparticles as a cocatalyst to produce CO, it seems reasonable that the Ag/$Na_2Ti_3O_7$(*SSR*) sample without any Ag nanoparticles cannot produce CO and the Ag/NTO(SSR) sample can produce CO selectively.

Next, among the two $Na_2Ti_6O_{13}$ samples, the Ag/NTO(*NaCl*) sample prepared by a flux method gave the higher formation rate of both CO and $H_2$ than the Ag/NTO(SSR) sample (Fig. 4c). This shows an advantage of the flux method to give the active $Na_2Ti_6O_{13}$ photocatalyst for this photocatalytic reaction. The CO formation rate over the present Ag/NTO(*NaCl*) sample with 1 wt% of Ag cocatalyst in the present reaction condition was 3.3 μmol $h^{-1}$ at 5 h, which is ca. 10

times higher than that over the best Ag/NTO sample in the previous study. The both Ag/NTO(*NaCl*) and Ag/NTO(*SSR*) samples showed similarly high CO selectivity (Fig. 4b and 4c). This is consistent with the fact that the Ag cocatalyst nanoparticles as the cocatalyst on the NTO surface showed similar SPR band in the UV-vis spectra (Fig. 3).

On both the Ag/NTO samples prepared by the SSR method and the flux method, the formation rate of CO and $H_2$ decreased and the $S_{CO}$ increased with irradiation time, which would be due to the aggregation of the deposited Ag particles as mentioned later and also in the previous study. The $O_2$ evolution was also observed in the current reaction condition although the ratio of consumed electron and holes was not consistent, $R(e^-/h^+)>1$, which will be discussed later. According to the results in this section, further studies were carried out on the Ag/NTO samples prepared by the flux method.

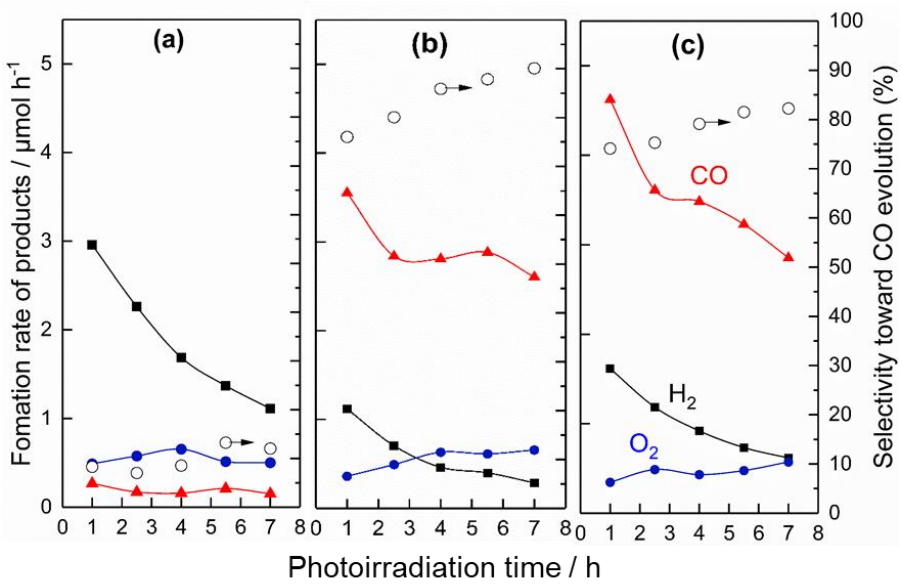


**Fig. 4** Formation rates of CO (red triangles), $H_2$ (black squares), and $O_2$ (blue circles), and the selectivity toward CO evolution (open circles) in the photocatalytic conversion of $CO_2$ with water over the prepared samples loaded with 1 wt% Ag cocatalyst loaded by the PD method, (a) the Ag/$Na_2Ti_3O_7$(*SSR*) sample, (b) the Ag/NTO(*SSR*), and (c) the Ag/NTO(*NaCl*) sample.

## 2-3.2 Sodium hexatitanate prepared by the flux method

It was well known that molten salt as a flux can regulate the crystal growth to provide a unique morphology of the crystals. In the previous study, some kinds of the salts such as LiCl, NaCl, KCl, and $CaCl_2$ were examined for the preparation of NTO samples, and it was found that the LiCl and $CaCl_2$ salts are not suitable for the preparation of $Na_2Ti_6O_{13}$ phase while only the KCl

and NaCl fluxes can promote the formation of the hexagonal rod-like crystals.[27] In order to figure out the effect of NaCl flux, another series of experiments were also conducted in this study. Four catalysts were prepared in the flux method using various fluxes such as NaF, NaCl, NaBr, and NaI. Pure $Na_2Ti_6O_{13}$ crystals were confirmed by the XRD patterns (Fig. 5) for these NTO samples except for the NTO(*NaI*) sample. It is noted that the distribution of the diffraction line intensity of the NTO(*NaI*) sample are different from those of the NTO(*NaCl*) and NTO(*NaBr*) samples and the reference, especially the ratio the intensity of the line at 11.86° corresponding to (200) plane and 14.12º corresponding to (-201) plane. In the UV spectra (Fig. 6), the NTO(*NaF*) sample exhibited a small shift of the absorption edge, and the NTO(*NaBr*) sample showed small absorbance of visible light. Furthermore, the SEM images show that the morphologies of NTO with different fluxes were quite different from each other, and it is notable that the NTO(*NaCl*) shown in Fig. 2c gave much clear morphology with uniform rod-like particles than others shown in Fig .8. This may be due to the effect of the difference in the electronegativity of the halogen atoms, i.e., 3.98, 3.16, 2.96, and 2.66 [47] for F, Cl, Br and I, respectively, or the melting point of the fluxes, i.e., 1266, 1074, 1028, and 933 K for NaF, NaCl, NaBr, NaI, respectively. Although the reason could not be clearly mentioned, it is the fact that the NaCl is quite suitable for the fabrication of the rod-like NTO particles.

Four catalysts were prepared via a flux method using sodium fluoride, sodium chloride, sodium bromide and sodium iodide. Their UV vis spectra were shown in Fig. 6. A very small shift of the absorption edge was observed for the NTO(*NaF*) sample, and a small and broad band in visible light region was also observed for the NTO(*NaBr*) sample.

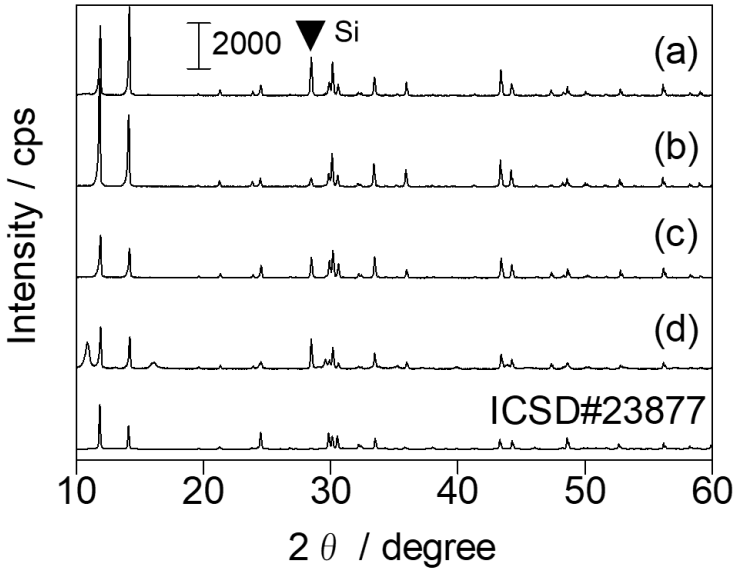


**Fig. 5.** XRD patterns of the prepared NTO samples with different flux; (a) NaF, (b) NaCl, (c) NaBr, (d) NaI, and ICSD#23877 for $Na_2Ti_6O_{13}$. Silicon powder mixed to calibrate the angle showed a diffraction indicated by a closed triangle.

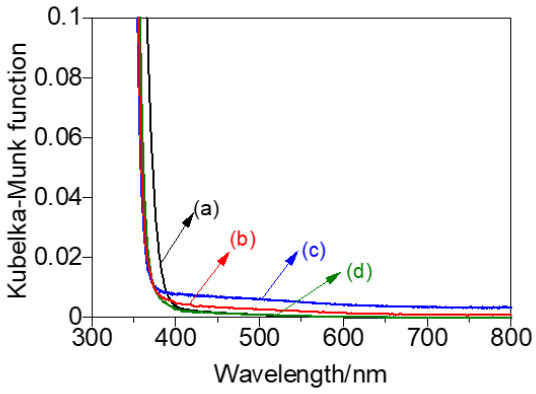


**Fig. 6** DR UV spectra of the prepared NTO samples with various flux; (a) NaF, (b) NaCl, (c) NaBr, and (d) NaI.

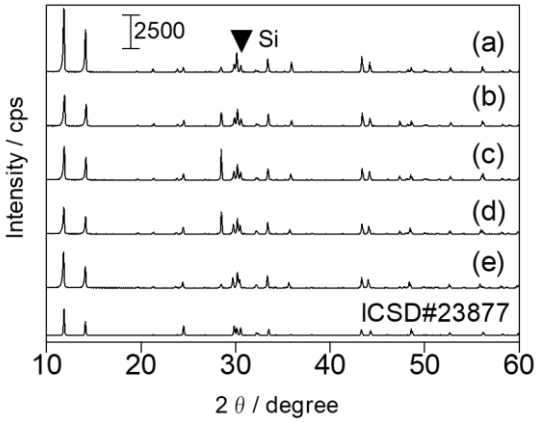


**Fig. 7** XRD patterns of the prepared NTO samples with various flux; (a) NaCl, (b) NaCl:KCl=3:1, (c) NaCl:KCl=1:1, (d) NaCl:KCl=1:3, (e) KCl, and ICSD#23877 for $Na_2Ti_6O_{13}$.

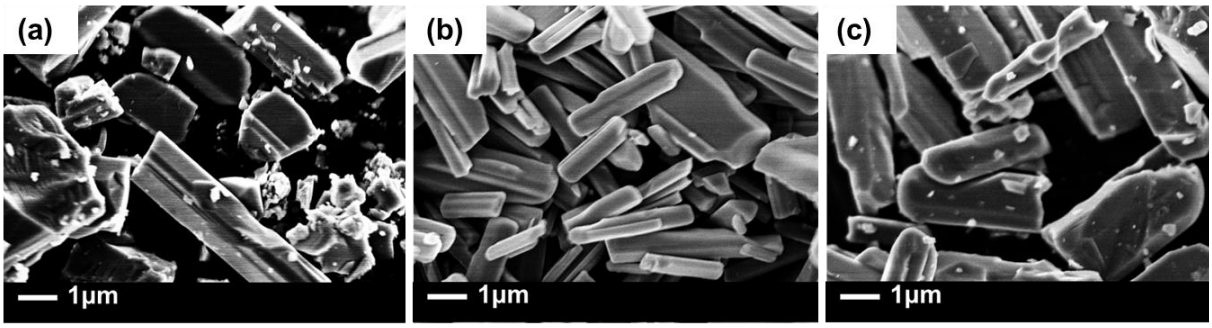


**Fig. 8** SEM images of the prepared NTO samples with various fluxes; (a) NaF, (b) NaBr, and (c) NaI.

The results of the photocatalytic activity tests of these samples loaded with Ag cocatalyst were shown in Fig. 9. It is quite clear that the sample prepared with NaCl exhibited the highest activity for CO evolution. It is also noted that the $R(e^-/h^+)$ with the sample prepared with NaCl was 4.6 at the initial reaction stage, which is much higher than other samples. This suggests that the NaCl flux may be beneficial to the preparation of the photocatalyst for CO production but the chloride anion ($Cl^-$) may be not good for sufficient oxygen evolution due to the reactivity to hole as discussed later.

In literature, it was reported that a mixture of two fluxes could enhance the activity of $Sr_2KTa_5O_{15}$ photocatalyst,[48] which motivated us to fabricate five samples with the different mixing ratio of NaCl and KCl fluxes in this study (Fig. 9). The results are mentioned in Fig. 10, the conclusion is, however, that the sample prepared with the pure NaCl flux exhibited the best photocatalytic activity among the examined NTO samples.

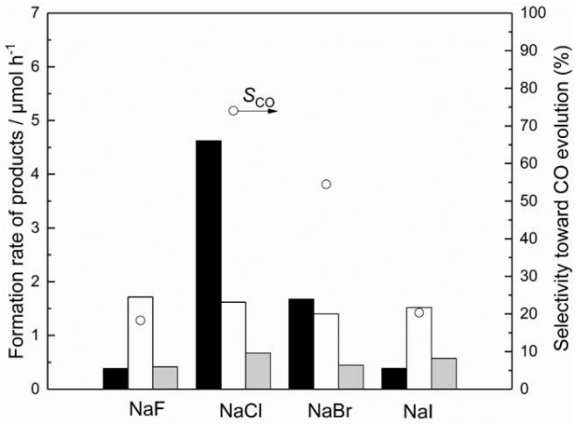


**Fig. 9** Formation rates of CO (black bar), $H_2$ (white bar), and $O_2$ (grey bar) and the $S_{CO}$ evolution (open circles) in the photocatalytic reaction tests with the Ag/NTO(*NaX*) (X: F, Cl, Br, and I) samples prepared by using various fluxes. The values were recorded after 1 hour's irradiation. Ag cocatalyst was loaded by the PD method.

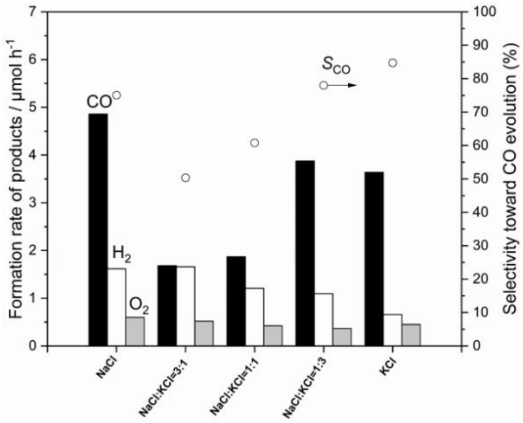


**Fig. 10** Formation rates of CO (black bar), $H_2$ (white bar), and $O_2$ (grey bar) and the $S_{CO}$ evolution (open circles) in the photocatalytic reaction tests with the Ag/NTO(*NaCl:KCl*) samples prepared by using the mixed flux consisting of different ratio of NaCl and KCl.

In this section, it was concluded the NTO sample prepared by a flux method with the pure NaCl flux is the optimized one for the reduction of $CO_2$ in the improved reaction condition. It was clarified that both the use of flux and the property of the flux much affected the shape of the particles and also the photocatalytic activity.

## 2-3.3 Ag cocatalysts

The Ag cocatalyst has been employed for the CO production in the heterogeneous photocatalytic reduction of $CO_2$ with water. The loading method and loading amount of the Ag cocatalyst have been reported to affect the state of Ag nanoparticles on the photocatalyst and

thus the photocatalytic activity and selectivity. [20,49–53] In the current study, the effects of the loading amount of Ag cocatalyst and loading method on the photocatalytic activity of the NTO(NaCl) samples for $CO_2$ conversion were investigated.

Fig. 11 shows the SEM images of the samples with different loading amount of the Ag cocatalyst prepared by the PD method. It was quite clear that the size of Ag particles became bigger with increasing the loading amount. The particle size of Ag over the 0.1wt% Ag/NTO(*NaCl*,PD), 0.5wt% Ag/NTO(*NaCl*,PD) and 1.0wt% Ag/NTO(*NaCl*,PD) samples were ca. 12–18 nm, 15–25 nm and 21–32 nm respectively. The Ag particles aggregated when the loading amount was over 1.0 wt%. In the DR UV-vis spectra Fig. 12, with the increase of the Ag loading amount, the band due to the Ag nanoparticles became larger and red-shifted, suggesting that the size of the deposited Ag particles increased, which consistent with the phenomenon observed in the SEM images.

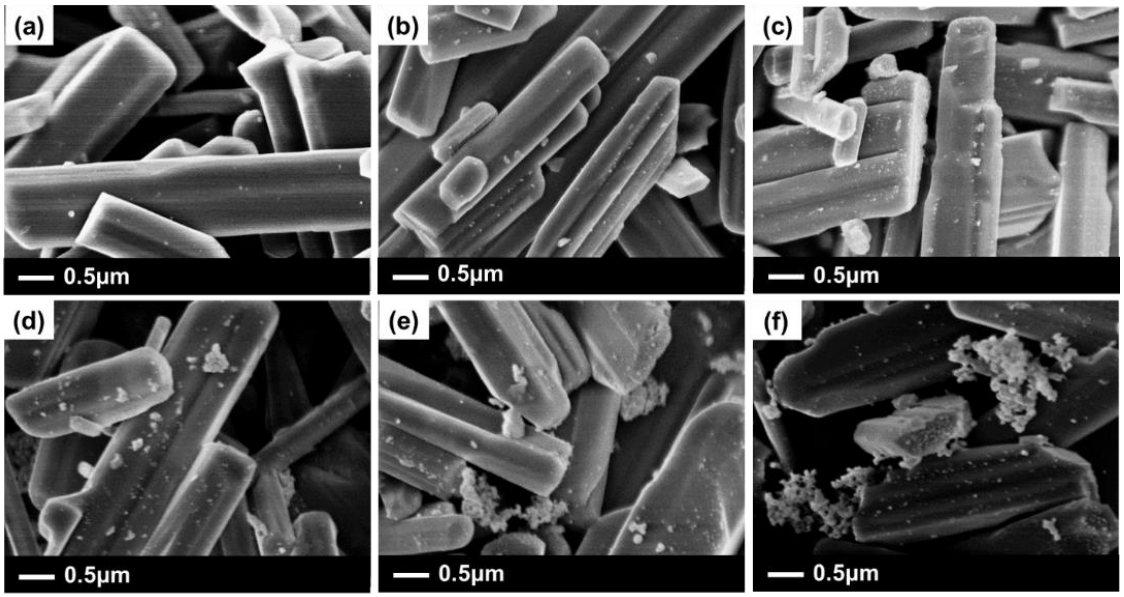


**Fig. 11** SEM images of the Ag/NTO(NaCl,PD) samples with different loading amount of Ag, (a) 0.1 wt%, (b) 0.5 wt%, (c) 1.0 wt%, (d) 2.0 wt%, (e) 3.0 wt%, and (f) 4.0 wt%, prepared by the PD method.

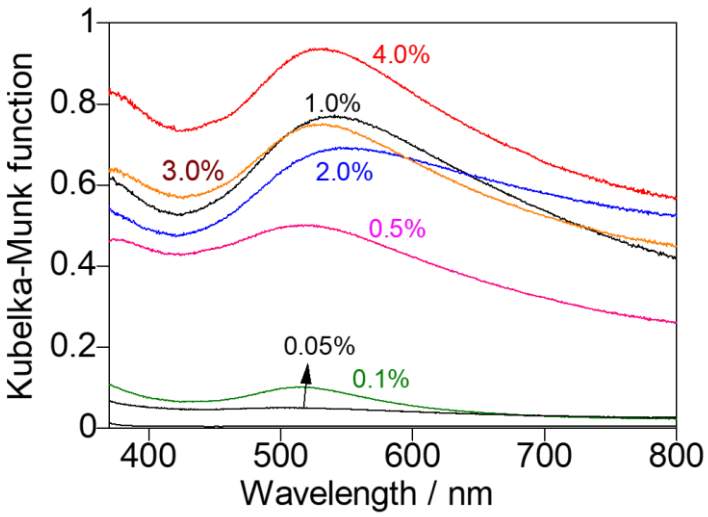


**Fig. 12** DR UV-vis spectra of the Ag/NTO(*NaCl*,PD) samples with various loading amount of Ag.

Fig. 13 shows the formation rate of the products during the photocatalytic conversion of $CO_2$ with water over the Ag/NTO(*NaCl*,PD) samples with different loading amount of Ag cocatalyst. Both the CO production rate and the $S_{CO}$ increased and with increasing the loading amounts from 0 wt% to 1.0 wt%, suggesting that the Ag cocatalyst enhances the CO formation and leads to decrease the active sites for $H_2$ evolution on the NTO surface. As a result, 1.0 wt% of Ag cocatalyst was the optimized mounts for providing the highest CO formation rate (4.6 μmol $h^{-1}$) and the highest selectivity toward CO evolution (74 %). On the other hand, the photocatalytic activity decreased above 1.0 wt% while $S_{CO}$ became constant to be 60%. This would be related to the aggregation of the Ag particles observed in the SEM images (Fig. 11), i.e., the surface area of Ag cocatalyst and its contact to the NTO surface would decrease due to the aggregation.

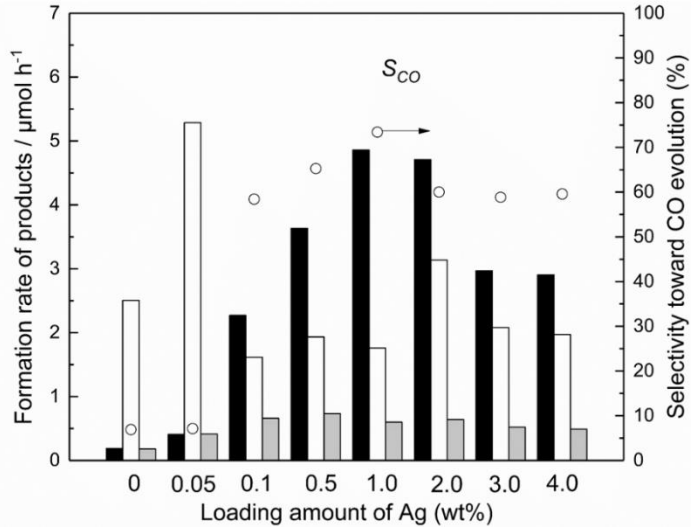


**Fig. 13** Formation rates of CO (black bar), $H_2$ (white bar), and $O_2$ (grey bar) and the $S_{CO}$ (open circles) in the photocatalytic conversion of $CO_2$ over the Ag/NTO(*NaCl*,PD) samples with different loading amount of Ag cocatalyst. The formation rates were recorded after 1 hour's irradiation. Photocatalyst powder: 0.2 g, reaction solution volume: 350 mL, additive: 0.5 M $NaHCO_3$, Ag loading method: photodeposition method, $CO_2$ flow rate: 15 mL $min^{-1}$, light source: 100-W high-pressure Hg lamp.

The SEM images of the 1 wt% Ag/NTO samples prepared by three methods are shown in Fig. 14, which were taken before and after the photocatalytic reaction tests. As synthesized, it was discovered that both the size of the Ag nanoparticles and their surface distribution on the three samples were quite different from each other (Figs. 14a, 14b, and 14c). When it was loaded by the PD method, some part of Ag nanoparticles with a size of 21–32 nm were mainly stabilized on the long facets of the rod-like crystals (Fig. 14a). During the photodeposition of Ag nanoparticles, $Ag^+$ cations are reduced by the photoexcited electron, meaning that the long facets would be the reductive facets that provide electrons predominantly. On the sample deposited by CR method, many fine Ag nanoparticles were more uniformly scattered on all the facets of the NTO crystals with the smallest size (10–15 nm) among the three samples (Fig. 14b). In this method, the adsorbed $Ag^+$ cation would be chemically reduced to form Ag nanoparticles on each facet. The IMP method provided a little larger Ag particle with a size of 70–75 nm (Fig. 14c). Probably, the procedure of drying up and calcination would make the $Ag^+$ cations and Ag oxide species get together to form larger silver oxide particles. As shown in Fig. 15A, this different phenomenon was also consistent with the DR UV-vis spectra of three samples. Characteristic bands assignable to Ag nanoparticles were observed for the

Ag/NTO(*NaCl*,CR) sample and the Ag/NTO(*NaCl*,PD) sample, but not for the Ag/NTO(*NaCl*,IMP) sample. And compared with the Ag/NTO(*NaCl*,PD) sample, the band over Ag/NTO(*NaCl*,CR) was a bit blue shifted, which indicated smaller size of Ag particles were fabricated by the CR method as shown in the SEM images (Figs. 14a and 14b).

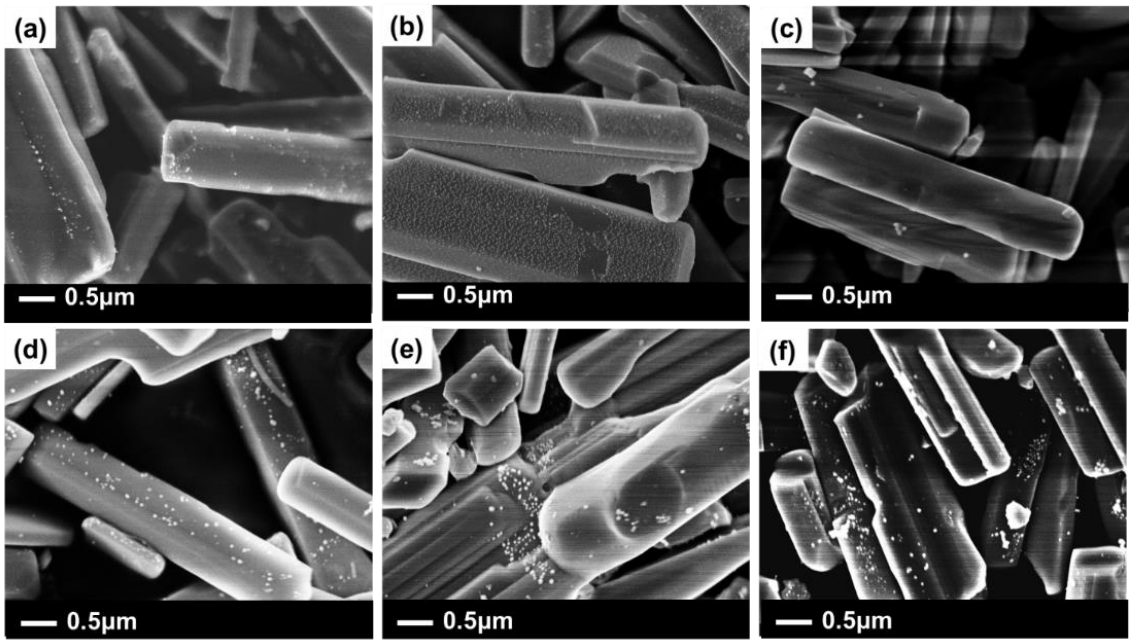


**Fig. 14** SEM images of the Ag/NTO(*NaCl*) samples prepared by (a, d) PD, (b, e) CR, and (c, f) IMP methods, (a–c) before and (d–f) after the photocatalytic reaction tests for 7 h.

After the photocatalytic reaction tests, however, the size and the distribution of the Ag particles became quite similar to each other (Figs. 10d–f), and almost similar bands assignable to Ag cocatalyst were observed for these samples (Fig. 15B). These results indicate that the Ag particles of these samples aggregated. In details, in the Ag/NTO(*NaCl*,PD) and Ag/NTO(*NaCl*,CR) samples, the particle sizes of the Ag nanoparticles became slightly larger, while the silver Ag particles were reduced and dispersed on the Ag/NTO(*NaCl*,IMP) sample. This means that the rearrangement of the Ag atoms takes place through the $Ag^0/Ag^+$ redox cycles as proposed in the previous study,[23] and this would be one of the reasons for the variation of the production rates with time during the photocatalytic reaction tests mentioned below.

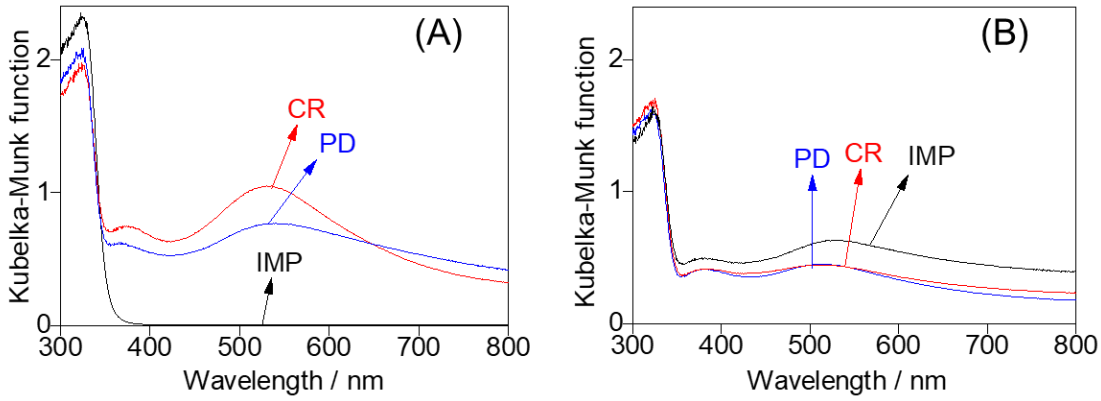


**Fig. 15** DR UV- spectra of the Ag/NTO(*NaCl*) samples loaded with 1 wt% Ag by the PD, CR, and IMP methods, recorded before (A) and after (B) photocatalytic reaction for 7 h.

Fig. 16 shows the formation rates of CO, $H_2$, and $O_2$ in the photocatalytic reaction tests for the conversion of $CO_2$ using the Ag/NTO(*NaCl*) samples, on which 1 wt% of Ag cocatalyst was loaded by the PD, CR, and IMP methods. Among the photocatalysts, the Ag/NTO(*NaCl*,PD) and Ag/NTO(*NaCl*,CR) samples exhibited higher photocatalytic activity than the Ag/NTO(*NaCl*,IMP) sample. And the CO production rate over the Ag/NTO(*NaCl*,PD) sample was 4.6 μmol $h^{-1}$ after irradiation for one hour, which was higher than the other samples. Since it is proposed that the PD method tends to form the Ag nanoparticles on the reductive facets of the rod-like NTO(*NaCl*) crystals, the Ag nanoparticles would efficiently receive the photo-excited electrons and promote the photocatalytic reduction of $CO_2$ to produce CO. The CO production rate gradually decreased from the start and became 2.8 μmol $h^{-1}$ after 7 h over the Ag/NTO(*NaCl*,PD) sample. The aggregation of Ag cocatalyst particles was one responsible reason for this deactivation. As shown in the SEM images (Fig. 10), the Ag particle sizes of the Ag/NTO(*NaCl*,PD) and Ag/NTO(*NaCl*,CR) samples became to 25-30 nm after 7 hours' reaction test, which could decrease the active sites of the Ag cocatalyst surface and the contact to the NTO surface, and thus reduce the photocatalytic activity.

In the previous reaction conditions, [27] the formation of $O_2$ was not observed initially. Even though it became actually observable 24 hours later, it was still not enough production rate compared to the formation rates of reductive products. In the present study, the $O_2$ evolution was observed even at the initial stage. However, the stoichiometric formation rate of $O_2$ was still not obtained during the initial period over the Ag/NTO(*NaCl*,PD) sample, where $R(e^-/h^+)$

was 3.0 after 7 hours' irradiation. This matter will be discussed in the next section.

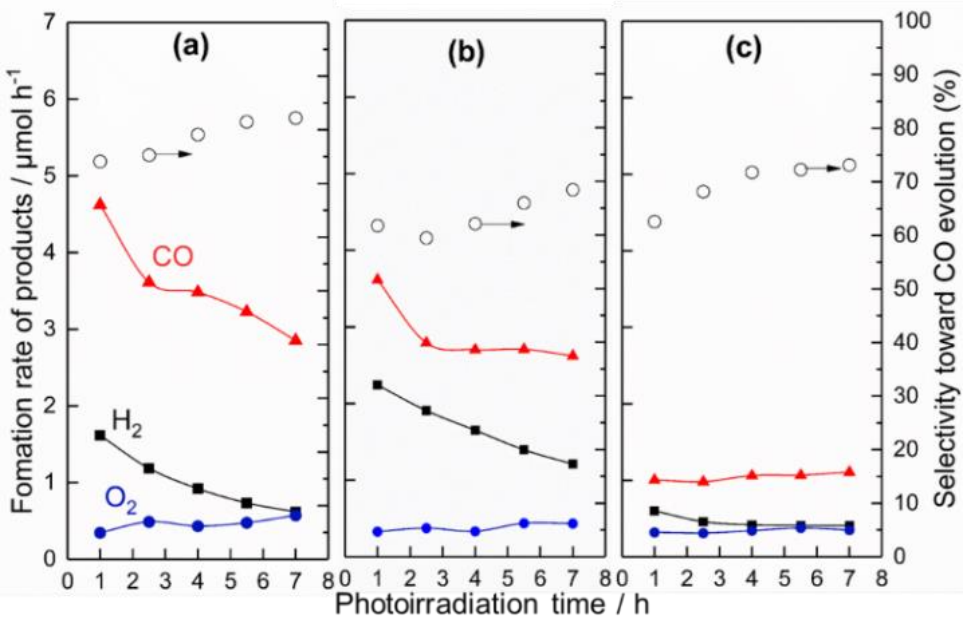


**Fig. 16** Formation rates of CO (red triangles), $H_2$ (black squares), and $O_2$ (blue circles) and the selectivity toward CO evolution (black circle) in the photocatalytic conversion of $CO_2$ with water over the Ag/NTO(*NaCl*) sample, on which 1 wt% of Ag cocatalyst was loaded by the PD (a), CR (b) and IMP (c) methods. Photocatalyst powder: 0.2 g, reaction solution volume: 350 mL, additive: 0.5 M $NaHCO_3$, Ag loading amount: 1.0 wt%, $CO_2$ flow rate: 15 mL $min^{-1}$, light source: 100-W high-pressure Hg lamp.

## 2-3.4 Oxidation reaction

The oxygen evolution reaction (OER) is one of the major challenges in the water splitting as well as $CO_2$ reduction with water. Many papers have been reported to improve the OER by combined the co-catalysts with some metal oxides such as manganese oxide, and so on.[54-59] And in literature, it is sometimes found that photocatalysts for water splitting produce only $H_2$ without enough evolution of $O_2$ ($H_2/O_2>2$). [31,60] This phenomenon may be explained by the difficulty of $O_2$ evolution due to the high overpotential of $O_2$ formation, which originates from trapping and stabilization of positive charge by the surface sites. [28-30] However, if the consumption of holes does not take place, the reductive reaction to produce CO and $H_2$ will also stop soon. Since the formation of reductive products underwent over 8 h in Fig. 16, the oxidation reaction should take place. Here, three possibilities are discussed as the reasons for this phenomenon.

The first possibility is that water might be oxidized to hydrogen peroxide [61] (Eq. 8).

$2H_2O + 2h^+ \rightarrow H_2O_2 + 2H^+$ (8)

To confirm this possibility, the starch iodine reaction test was carried out. It showed a negative result for the solution after the photocatalytic reaction test as described in the supplementary information, i.e., the color change was not observed as shown in Fig. 17. Thus, it can be mentioned that this was at least not the dominant reason.

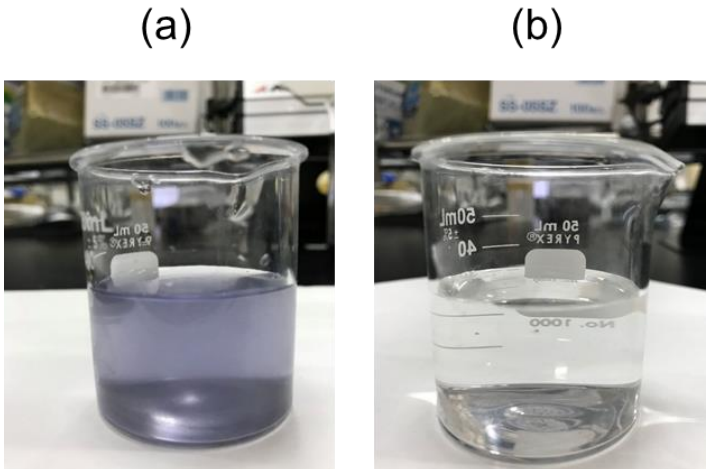


**Fig. 17** The results of the starch-iodine test for (a) the prepared reference $H_2O_2$ solution and (b) the reaction solution collected after the photocatalytic reaction test with the Ag/NTO(*NaCl*,PD) sample, on which 1.0 wt% of Ag cocatalyst was loaded.

The second possibility is that residual chloride anion ($Cl^-$) on the surface of the NTO(*NaCl*,PD) photocatalyst, originating from the NaCl flux, might react with the photoformed hole to form hypochlorite ($ClO^-$) shown in eq. 9, which competitively consume hole and reduce the oxidation of water to form $O_2$.

$Cl^- + H_2O + 2\ h^+ \rightarrow ClO^- + 2H^+$ (9)

$2ClO^- + h\nu\ (\lambda < 400\ nm) \rightarrow O_2 + 2Cl^-$ (10)

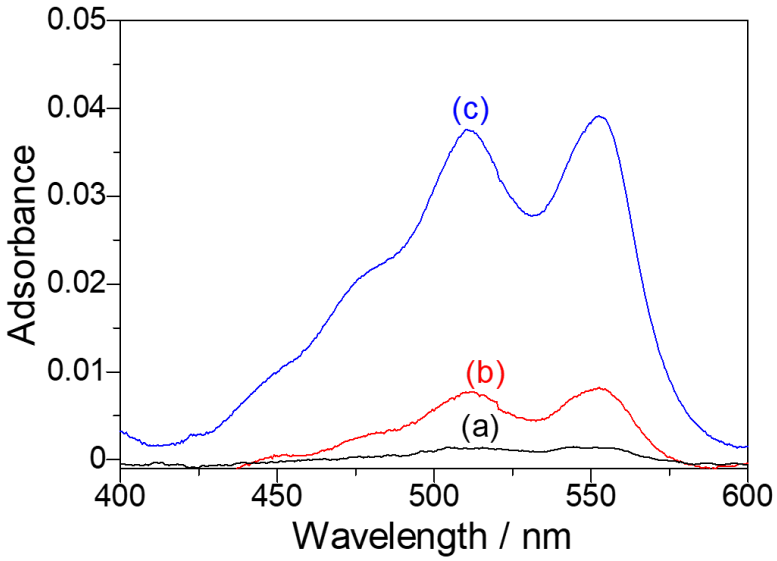


**Fig. 18** Absorption spectra of the resulting solutions for the DPD tests to confirm HClO in (a) distilled water, (b) the reaction solution collected after the photocatalytic reaction test with the Ag/NTO(*SSR*,PD), and (c) that with the Ag/NTO(*NaCl*,PD) sample. The loading amount of Ag for each sample was 1.0 wt%.

Fig. 18 shows the absorption spectra of the resulting solutions for the DPD tests [39] to confirm the formation of HClO during the reaction tests, which were obtained after the photocatalytic reaction tests carried out with the Ag/NTO(*SSR*,PD) sample and the Ag/NTO(*NaCl*,PD) sample, and the distilled water as a reference. For the solution from the reaction test with the Ag/NTO(*NaCl*,PD) sample showed quite higher absorbance in 515 nm than that from the test with the Ag/NTO(*SSR*,PD) sample. This indicates that hypochlorous anion $ClO^-$ was produced in the reaction test with the Ag/NTO(*NaCl*,PD) sample. Therefore, it was found that the chloride anion $Cl^-$ remaining as a residue was photocatalytically oxidized to $ClO^-$, which competitively consumed the photoformed holes on the Ag/NTO(*NaCl*,PD) photocatalyst. After photoirradiation for 7 hours, the amount of $ClO^-$ was 0.8 μmol, which was calculated using the standard curve reported in the literature.

Thus, it was clarified that $Cl^-$ residue was oxidized to $ClO^-$, which competitively consumed holes to reduce the formation of $O_2$. The detected amount of $ClO^-$, calculated by the standard curve reported in the literature,[42] was quite small (0.8 μmol) after 7 hours' irradiation. This may be due to the decomposition of hypochlorite ($ClO^-$) shown in the eq. 10 since the high-pressure mercury lamp was used in the current system. With the increasing concentration of $ClO^-$ in the

solution, the reaction rate of eq.9 would decrease while the rate of eq.10 would increase. And when the reaction rate of the eq. 10 increased to a half of that of the eq. 9, the stoichiometric amount of $O_2$ was supposed to be produced in the current system.

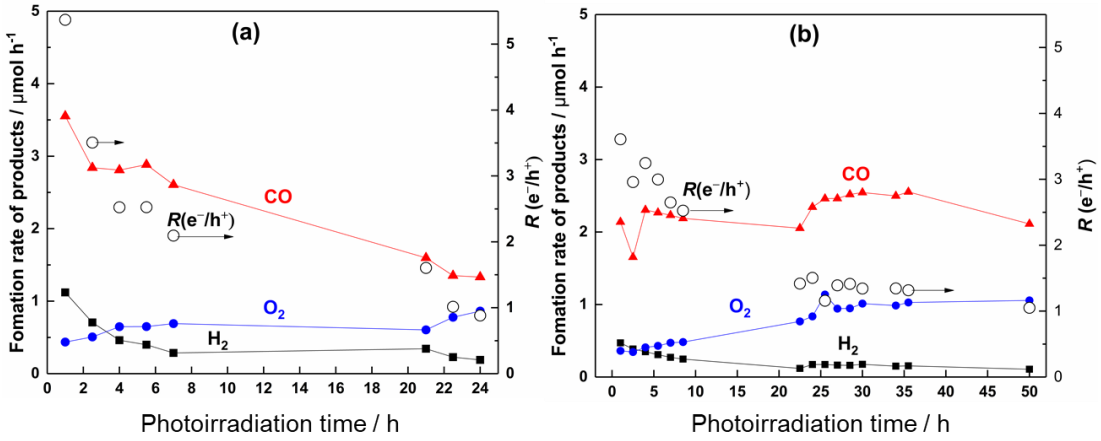


**Fig. 19** Formation rates of CO (red triangles), $H_2$ (black squares), and $O_2$ (blue circles) and the $R(e^-/h^+)$] (open circle in the photocatalytic conversion of $CO_2$ with water by using (a) the Ag/NTO(*SSR*,PD) sample and (b) the Ag/NTO(*NaCl*,PD) sample. Photocatalyst powder: 0.2 g, reaction solution volume: 350 mL, additive: 0.5 M $NaHCO_3$, Ag loading method: photodeposition method, $CO_2$ flow rate: 15 mL $min^{-1}$, light source: 100-W high-pressure Hg lamp.

The third possibility is that the produced $O_2$ might be adsorbed on the surface of catalysts to some extent especially under photoirradiation, since the photoadsorption of oxygen on $TiO_2$ was reported.[32,33] Fig. 19 shows the formation rates of CO, $H_2$, and $O_2$ and the consumed $e^-/h^+$ ratio, $R(e^-/h^+)$, in the photocatalytic conversion of $CO_2$ over the two samples, Ag/NTO(*SSR*,PD) and Ag/NTO(*NaCl*,PD). Even in the case of the reaction test with the Ag/NTO(*SSR*,PD) sample, the $O_2$ evolution increased with irradiation time, and the $R(e^-/h^+)$ became to be 1.0 after 22.5 hours. Since this sample should be free from chloride anion, the initially insufficient $O_2$ evolution could be explained by not the oxidation of chloride anion but the photoadsorption of $O_2$ on the surface of catalysts. After 22.5 hours, the $O_2$ photoadsorption on the surface would be saturated and no more photoadsorption would take place.

Even for the Ag/NTO(*NaCl*,PD) samples, the ratio of $e^-/h^+$ became gradually close to be 1.0 after about 50 hours. In this state, not only the $O_2$ photoadsorption but also the composition of the chloride ($Cl^-$) should be taken into consideration. The concentration of hypochlorite ($ClO^-$) anion would also become constant in the reaction solution to give $O_2$ evolution.

As a summary of this section, two possible reasons for the non-stoichiometric amount of $O_2$ evolution can be proposed as follows, i.e., the oxidation of chloride residues and the photoadsorption of $O_2$ on the surface.

## 2-4 Conclusion

In this study, two remained problems in the previous work, one of which is low activity toward CO evolution and low selectivity, and the other is nonstoichiometric $O_2$ evolution, were much improved and explained, respectively.

First, it was found that the Ag/NTO sample, with 1.0 wt% of Ag cocatalyst loaded by a photodeposition method, exhibited the highest CO production rate (4.6 μmol $h^{-1}$) and the highest CO selectivity (74%) among the examined samples in the current reaction conditions. These values are more than 29 times higher production rate and more than 2.7 times higher selectivity than those obtained in the previous study, which would originate from the optimization of the photocatalyst and the improved reaction conditions. In addition, among three Ag/NTO samples, on which 1.0 wt% of the Ag cocatalyst nanoparticles were loaded by different methods, the Ag/NTO sample provided by the PD method gave the highest activity and selectivity for $CO_2$ reduction. Since the PD method tends to form the metallic Ag nanoparticles on the reductive facets of the rod-like NTO crystals, which can efficiently promote the CO evolution.

Second, although the evolution rate of $O_2$ was not enough in the induction period, it increased with time and reached to the stoichiometric formation ratio of the oxidative and reductive products after a long time, such as 24 or 50 h, depending on the samples. Furthermore, it was confirmed that the chloride residues and the photoadsorption of $O_2$ on the surface are responsible for the insufficient $O_2$ evolution less than stoichiometric ratio among the products at the initial period.

## References


1 M. Mikkelsen, M. Jørgensen and F. C. Krebs, *Energy Environ. Sci.*, 2010, **3**, 43–81.

2 J. L. White, M. F. Baruch, J. E. Pander, Y. Hu, I. C. Fortmeyer, J. E. Park, T. Zhang, K. Liao, J. Gu, Y. Yan, T. W. Shaw, E. Abelev and A. B. Bocarsly, *Chem. Rev.*, 2015, **115**, 12888–12935.

3 B. Kumar, M. Llorente, J. Froehlich, T. Dang, A. Sathrum and C. P. Kubiak, *Annu. Rev. Phys. Chem.*, 2012, **63**, 541–569.

4 X. Chang, T. Wang and J. Gong, *Energy Environ. Sci.*, 2016, **9**, 2177–2196.

5 J. Low, J. Yu and W. Ho, *J. Phys. Chem. Lett.*, 2015, **6**, 4244–4251.

6 M. Halmann, *Nature*, 1978, 275, 115–116.

7 M. Asadi, B. Kumar, A. Behranginia, B. A. Rosen, A. Baskin, N. Repnin, D. Pisasale, P. Phillips, W. Zhu, R. Haasch, R. F. Klie, P. Král, J. Abiade and A. Salehi-Khojin, *Nat. Commun.*, 2014, **5**, 1–8.

8 J. C. Hemminger, R. Carr and G. A. Somorjai, *Chem. Phys. Lett.*, 1978, **57**, 100–104.

9 S. N. Habisreutinger, L. Schmidt-Mende and J. K. Stolarczyk, *Angew. Chemie - Int. Ed.*, 2013, **52**, 7372–7408.

10 T. Arai, S. Sato, T. Kajino and T. Morikawa, *Energy Environ. Sci.*, 2013, **6**, 1274–1282.

11 S. Sato, T. Arai, T. Morikawa, K. Uemura, T. M. Suzuki, H. Tanaka and T. Kajino, *J. Am. Chem. Soc.*, 2011, **133**, 15240–15243.

12 O. Ishitani|, C. Inoue, Y. Suzuki and T. Ibusuki, *J. Photochem. Photobiol. A Chem.*, 1993, **72**, 269–271.

13 A. Nakada, T. Nakashima, K. Sekizawa, K. Maeda and O. Ishitani, *Chem. Sci.*, 2016, **7**, 4364–4371.

14 S. C. Roy, O. K. Varghese, M. Paulose and C. A. Grimes, *ACS Nano*, 2010, **4**, 1259–1278.

15 K. Iizuka, T. Wato, Y. Miseki, K. Saito and A. Kudo, *J. Am. Chem. Soc.*, 2011, **133**, 20863–20868.

16 M. Yamamoto, T. Yoshida, N. Yamamoto, T. Nomoto, Y. Yamamoto, S. Yagi and H. Yoshida, *J. Mater. Chem. A*, 2015, **3**, 16810–16816.

17 N. Yamamoto, T. Yoshida, S. Yagi, Z. Like, T. Mizutani, S. Ogawa, H. Nameki and H. Yoshida, *e-Journal Surf. Sci. Nanotechnol.*, 2014, **12**, 263–268.

18 M. Yamamoto, T. Yoshida, N. Yamamoto, H. Yoshida and S. Yagi, *e-Journal Surf. Sci. Nanotechnol.*, 2014, **12**, 299–303.

19 H. Tatsumi, K. Teramura, Z. Huang, Z. Wang, H. Asakura, S. Hosokawa and T. Tanaka, *Langmuir*, 2017, **33**, 13929–13935.

20 R. Pang, K. Teramura, H. Tatsumi, H. Asakura, S. Hosokawa and T. Tanaka, *Chem. Commun.*, 2018, **54**, 1053–1056.

21 T. Takayama, K. Tanabe, K. Saito, A. Iwase and A. Kudo, *Phys. Chem. Chem. Phys.*, 2014, **16**, 24417–24422.

22 Z. Wang, K. Teramura, S. Hosokawa and T. Tanaka, *Appl. Catal. B Environ.*, 2015, **163**, 241–247.

23 H. Yoshida, L. Zhang, M. Sato, T. Morikawa, T. Kajino, T. Sekito, S. Matsumoto and H. Hirata, *Catal. Today*, 2015, **251**, 132–139.

24 A. Anzai, N. Fukuo, A. Yamamoto and H. Yoshida, *Catal. Commun.*, 2017, **100**, 134–138.

25 S. Xie, Y. Wang, Q. Zhang, W. Deng and Y. Wang, *Chem. Commun.*, 2015, **51**, 3430–3433.

26 R. Pang, K. Teramura, H. Asakura, S. Hosokawa and T. Tanaka, *Appl. Catal. B Environ.*, 2017, **218**, 770–778.

27 H. Yoshida, M. Sato, N. Fukuo, L. Zhang, T. Yoshida, Y. Yamamoto, T. Morikawa, T. Kajino, M. Sakano, T. Sekito, S. Matsumoto and H. Hirata, *Catal. Today*, 2018, **303**, 296–304.

28 Y. F. Li, Z. P. Liu, L. Liu and W. Gao, *J. Am. Chem. Soc.*, 2010, **132**, 13008–13015.

29 A. Vojvodic and J. K. Nørskov, *Science (80-. ).*, 2011, **334**, 1355–1356.

30 Z. Fang and D. A. Dixon, *J. Phys. Chem. A*, 2013, **117**, 3539–3555.

31 R. Abe, *J. Photochem. Photobiol. C Photochem. Rev.*, 2010, **11**, 179–209.

32 T. Berger, M. Sterrer, O. Diwald and E. Knözinger, *ChemPhysChem*, 2005, **6**, 2104–2112.

33 R. I. Bickley and F. S. Stone, *J. Catal.*, 1973, **31**, 389–397.

34 A. Izgorodin, E. Izgorodina and D. R. MacFarlane, *Energy Environ. Sci.*, 2012, **5**, 9496–9501.

35 O. C. Compton and F. E. Osterloh, *J. Phys. Chem. C*, 2009, **113**, 479–485.

36 M. Krivec, R. Dillert, D. W. Bahnemann, A. Mehle, J. Štrancar and G. Dražić, *Phys. Chem. Chem. Phys.*, 2014, **16**, 14867–14873.

37 P. Calza and E. Pelizzetti, *Pure Appl. Chem.*, 2001, **73**, 1839–1848.

38 L. Huang, R. Li, R. Chong, G. Liu, J. Han and C. Li, *Catal. Sci. Technol.*, 2014, **4**, 2913–2918.

39 S. Iguchi, K. Teramura, S. Hosokawa and T. Tanaka, *Phys. Chem. Chem. Phys.*, 2015, **17**, 17995–18003.

# Chapter 3 Enhancement of selective reduction carbon dioxide with water by controlling the shape of potassium hexatitanate by a flux method


## Abstract

To achieve a more efficient system for photocatalytic reduction of carbon dioxide with water, silver-loaded alkali titanate photocatalyst were studied in the improved reaction conditions. After comparing four types of alkali titanates ($A_2Ti_6O_{13}$, A=Na, K, Rb, Cs), the further development of potassium hexatitanate ($K_2Ti_6O_{13}$: KTO) photocatalyst prepared by the flux method was examined. The flux method has been extensively investigated to provide fine single crystals of various sizes and morphology, which depends on the synthesis conditions. In this study, KTO samples of rod-like structure with high crystallinity were synthesized, and the effects of preparation condition such as the fluxes, the ratio of flux and substrate, and the holding temperature on both the structure and photocatalytic activity were investigated. As a result, the Ag/KTO sample consisting of the suitable size of rod-like KTO crystals prepared at 1273 K with holding time of 10 h gave the highest activity for CO evolution and the highest selectivity toward CO (96%).


## 3-1 Introduction

Alkali-metal hexatitanate, $A_2Ti_6O_{13}$ (where A =Na, K, Rb, Cs.), consisting of a tunnel or layer structure, are a set of well-known functional materials with wide applications in many fields such as electrochemistry, [1,2] ion exchange, [3–5] and photocatalyst.[6–9] Among the alkali-metal titanates, potassium hexatitanate (KTO) whiskers exhibit excellent thermal insulating properties and high chemical stability. Because of the tunnel structure of KTO, the potassium ions lie in the centre and are enclosed by other atoms, which leads to the fact that they cannot escape outside and are isolated from the external environment.

Given a specific photocatalytic material, controlling charge separation and migration is critical because the band structure and crystallographic character of each semiconducting material

are unique. The movement of excited electrons and holes, and thus the photocatalytic activity, can be greatly affected by the crystallinity, particle size, and doping. Higher crystallinity and smaller particle sizes are desirable for charge migration toward surface active sites before recombination, which can be controlled by the different synthesis methods and conditions.

To date, several strategies have been employed to obtain the KTO whiskers, such as calcination,[10–12] flux growth, [6,13,14] hydrothermal,[15,16] sol-gel method [17,18] and et.al. The flux method has been extensively investigated to provide fine single crystals of various size and morphology among the above-mentioned methods, which depends on the synthesis conditions.[19] In principle, the crystal growth can proceed in a mixture of solute and molten salt especially during gentle variation of the state of the molten salt mixture, that is, with decreasing amount of molten salt or temperature to reduce the solubility. Thus, in recent years, this method has been applied to synthesize micro or nanosized various inorganic crystals as photocatalysts, e.g., $Na_2Ti_6O_{13}$,[20,21] $Na_2Ti_3O_7$,[22] $K_2Ti_6O_{13}$,[6,23] $CaTiO_3$,[24,25] $La_2Ti_2O_7$,[26,27] and $Sr_2KTa_5O_{15}$[28,29] for water splitting or $CO_2$ reduction in aqueous solution. Most of them were well crystallized, and it is considered that the crystal having various facets or structured surface would be advantageous for the photocatalytic reaction since the photoexcited electrons and holes generated in the crystallites might go to a different surface, which would decrease the frequency of electron–hole recombination.[30,31] Such surfaces would separate the reductive or oxidative sites, and they could reduce the recombination rate of active holes and electrons and increase the number of valuable holes and electrons, which lead to the enhancement of the photocatalytic activity.

In recent years, the photoreduction of $CO_2$ with water into organic compounds by using photocatalysts has been widely studied. Heterogeneous photocatalysis have been studied for the reduction of $CO_2$ with water to produce formate, CO, $CH_3OH$ and $CH_4$,[32–40] and it was discovered the Ag cocatalyst nanoparticles could function as the active sites for $CO_2$ reduction to form CO.[31] In recent years, many kinds of Ag-modified photocatalysts to produce CO, $H_2$ and $O_2$ have been reported, such as $Ag/BaLa_4Ti_4O_{15}$, [31] $Ag/Ga_2O_3$, [41–43] $Ag/KCaSrTa_5O_{15}$,[44] $Ag/La_2Ti_2O_7$, [45] and $Ag/CaTiO_3$,[24,25] $Ag/SrNb_2O_6$,[46,47] $Ag/Na_2Ti_6O_{13}$.[20,21] However, many reported photocatalysts exhibit low activity or low selectivity for the photocatalytic conversion of $CO_2$ by $H_2O$, thus it is still far to this technique put into practice.

In these reaction systems, the reduction of $CO_2$ and protons with the photoexcited electrons

proceed to form CO and $H_2$, respectively on the reductive sites of the photocatalyst surface (Eqs. 1 and 2), while the oxidation of water with positive holes into $O_2$ and protons occurs on the oxidative sites (Eq. 3).

$$CO_2 + 2\ H^+ + 2\ e^- \rightarrow CO + H_2O \quad (1)$$

$$2\ H^+ + 2\ e^- \rightarrow H_2 \quad (2)$$

$$2\ H_2O + 4\ h^+ \rightarrow O_2 + 4\ H^+ \quad (3)$$

When no other reductive products than CO and $H_2$ are observed in the reaction system, the selectivity toward CO evolution, $S_{CO}$(%), and the ratio of the consumed electron and hole, $R(e^-/h^+)$, can be calculated according to Eqs. 4 and 5, respectively, [25,47], where the production rate of CO, $H_2$ and $O_2$ are referred to as $R_{CO}$, $R_{H2}$ and $R_{O2}$, respectively. The value of $R(e^-/h^+)$ should be unity if the two competitive reactions, Eqs. 1, 2 and 3, take place ideally in any balance.

$$S_{CO}\ (\%) = 100 \times R_{CO}/\ (R_{CO} + R_{H2}) \quad (4)$$

$$R(e^-/h^+) = (2R_{CO} + 2R_{H2})/4R_{O2} \quad (5)$$

Thus, in the present study, four kinds of hexatitanate titanate photocatalysts, two of which were once reported in our previous study, [20,21,48] were examined and compared in the improved reaction conditions for the photocatalytic reduction of $CO_2$ by $H_2O$. After comparing four types of alkali titanates ($A_2Ti_6O_{13}$, A=Na, K, Rb, Cs), the further development of potassium hexatitanate ($K_2Ti_6O_{13}$: KTO) photocatalyst prepared in the flux method was examined. The flux method has been extensively investigated to provide fine single crystals of various sizes and morphology, which depends on the synthesis conditions. In this study, KTO rod-like structure were synthesized, and the effects of preparation condition such as the fluxes, the ratio of flux and substrate, and the holding temperature, on both the structure and photocatalytic activity were investigated.

## 3-2 Experimental

### 3-2.1 Photocatalyst preparation

Alkali titanate ($A_2Ti_6O_{13}$) samples except the $Cs_2Ti_6O_{13}$ sample were prepared by a flux method.[20] For the flux method for the $K_2Ti_6O_{13}$ samples, the precursors, $K_2CO_3$ (Kishida) and $TiO_2$ (rutile, Kojundo), and a flux reagent such as LiCl, NaCl, $CaCl_2$ (Nacalai Tesque) or KCl (Kishida) were mixed, where the molar ratio of $K_2CO_3$ to $TiO_2$ was 1:6. And various ratio (*x*

[mol%]) of flux was calculated, *x* [mol%] = 100 × (amount of a flux [mol])/(amount of $A_2Ti_6O_{13}$ [mol]+ amount of a flux [mol]). The mixture was put into a alumina crucible, heated in an electric muffle furnace with a rate of 200 K $h^{-1}$ to 1073-1573 K, held at this temperature for 1, 3, 5, 10, 15 h, and then cooled at a rate of −100 K $h^{-1}$ to 773 K, followed by being naturally cooled to room temperature in the furnace. The obtained powder was thoroughly washed with hot water (353 K) for 4 times to remove the residual salt, then dried at 323 K for 24 hours. For the SSR method of the $K_2Ti_6O_{13}$ and the $Cs_2Ti_6O_{13}$ sample, the precursors were mixed for 30 minutes in an alumina mortar and fabricated in the same heating program as mentioned above. These samples are referred to as ATO(*flux*) and ATO(*SSR*), respectively.

Ag cocatalyst was loaded on the surface by a photodeposition method (PD). In the PD method, 1 g of the $A_2Ti_6O_{13}$ sample in 100 mL of ion-exchanged water was irradiated using a 300 W xenon lamp (PE300BUV) for 2 hours with magnetically stirring, where the light intensity was measured to be 22 mW $cm^{-2}$ at 254 ± 20 nm in wavelength. Then the obtained solution was washed and filtrated for 3 times and dried at 323 K for 24 hours.

### 3-2.2 Characterization

The loading amount of Ag on the samples was evaluated by X-ray florescence analysis with a EDX-8000 (Shimadzu) using an experimentally obtained calibration curve. The crystal structure of the samples was determined by powder X-ray diffraction with Lab X XRD-6000 (Shimazu). Morphologies of the samples were observed by scanning electron microscopy (SEM) image with JSM-890 (JEOL). Diffuse reflectance UV-Vis spectrum was recorded by a V-670 (JASCO). The Brunauer-Emmett-Teller (BET) specific surface area was calculated from the amount of $N_2$ adsorption at 77 K, which was measured by a Monosorb (Quantachrome).

### 3-2.3 Photocatalytic reaction

The photocatalytic activity test of $CO_2$ reduction was carried out using a flow system with an inner-irradiation-type reaction vessel [25]. The Ag-loaded $A_2Ti_6O_{13}$ sample (0.2 g) was dispersed in ion-exchanged water (350 mL) containing 0.5 M $NaHCO_3$, and suspended by magnetically stirring. The photocatalytic activity tests of $CO_2$ reduction were also carried out over the KTO samples loaded with Ag cocatalysts, in which the $CO_2$ flow rate was 15 mL $min^{-1}$.The $H_2$, $O_2$, and CO products in the outlet from the reactor were detected by using an on-line chromatograph (Shimadzu, GC-8A, TCD, Shincarbon ST column, Ar gas carrier).

## 3-3 Results and Discussions

### 3-3.1 Alkali hexatitanate

In the present study, four kinds of pure alkali hexatitanate, sodium hexatitanate (NTO), potassium hexatitanate (KTO), rubidium hexatitanate (RTO) were fabricated by a flux method, and NaCl flux was used as a flux. However, it turned out that the diffraction lines of these four samples corresponding to NTO reference dates in XRD patterns(Fig.1). This indicated that the NaCl flux could react with raw materials easily. The SEM images showed that the NTO(*NaCl*), KTO(*NaCl*), RTO(*NaCl*), and CTO(*NaCl*) samples consisted of similar roundish rod-like particles (Fig. 1a, b c and d), while the particles of KTO(KCl) sample were more uniform consisted of shortest particles. On the other hand, due to the formation of the NTO photocatalyst.

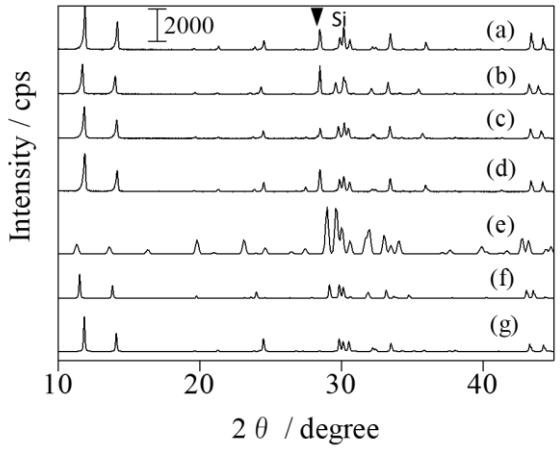


**Fig. 1** XRD patterns of prepared $A_2Ti_6O_{13}$ samples, (a) NTO(*NaCl*); (b)KTO(*NaCl*); (c) RTO(*NaCl*); (d)CTO(*NaCl*) and ICSD#23878 for $Rb_2Ti_6O_{13}$(e) and ICSD#25712 for $K_2Ti_6O_{13}$(f) and ICSD#23877 for $Na_2Ti_6O_{13}$(g).

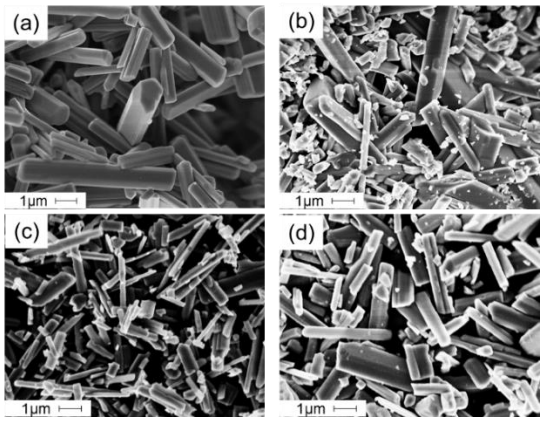


**Fig.2** SEM images of the prepared $A_2Ti_6O_{13}$ samples by the flux method with the NaCl flux, (a) NTO(*NaCl*); (b)KTO(*NaCl*); (c) RTO(*NaCl*); (d)CTO(*NaCl*).

From the above result, the NaCl flux was not suitable for all alkali hexatitanate preparation. Therefore, another flux was considered to be used in this study, and four kinds of pure alkali hexatitanate, NTO(*NaCl*), KTO(*KCl*), and RTO(*RbCl*) were successfully fabricated by a flux method, and cesium hexatitanate (CTO) was prepared by the solid state method due to the involved flux could easily to react with the precursors. Fig. 1 shows XRD patterns of the

obtained samples with those from the database (ICSD#23877 for $Na_2Ti_6O_{13}$(e), ICSD#25712 for $K_2Ti_6O_{13}$(f) and ICSD#23878 for $Rb_2Ti_6O_{13}$(g)) as references. The patterns of the prepared NTO(*NaCl*), KTO(*KCl*), and RTO(*RbCl*) samples (Fig. 3a, b, and c) were consistent with the reference data, respectively. Since no diffraction lines corresponding to other impurity phases were observed, it was confirmed that these three types of alkali hexatitanate were correctly fabricated by the flux method. In terms of the CTO, neither the NaCl nor the CsCl flux could be used to fabricate the pure CTO sample, which may be due to the layer structure of CTO sample. But the CTO sample was successfully prepared via a SSR method reported in previous research, and as was shown in Fig. 1d, the XRD patterns of the prepared CTO sample were consistent with the data reported in previous research.[7,49]

Fig. 2 shows the SEM images. The NTO(*NaCl)*, KTO(*KCl*), and RTO(*RbCl*) samples consisted of similar roundish rod-like particles (Fig. 4a, b, and c), while the particles of KTO(*KCl*) sample were more uniform and consisted of shortest particles. On the other hand, the CTO(*SSR*) sample consisted of irregular shape of particles, most of which were smaller than 1 μm (Fig. 4d). This confirms that the molten salt can enhance the crystallization and regulate the crystal growth of each facet to form the unique morphology for alkali hexatitanate.

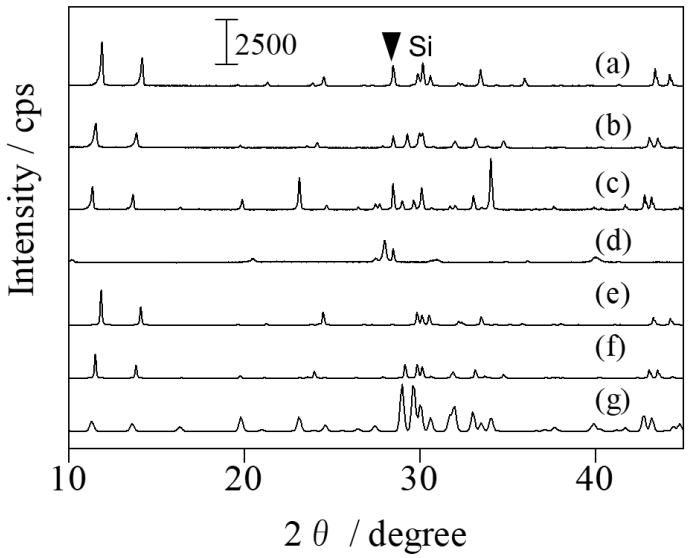


**Fig. 3** XRD patterns of prepared $A_2Ti_6O_{13}$ samples; (a) $Na_2Ti_6O_{13}$(*NaCl*), (b) $K_2Ti_6O_{13}$ (*KCl*), (c)$Rb_2Ti_6O_{13}$ (*RbCl*) and $Cs_2Ti_6O_{13}$ (*SSR*). Silicon powder mixed to calibrate the angle showed a diffraction indicated by a closed triangle. The patterns from the ICSD database are also shown, ICSD#23877 for $Na_2Ti_6O_{13}$(e) , ICSD#25712 for $K_2Ti_6O_{13}$(f) and ICSD#23878 for $Rb_2Ti_6O_{13}$(g).

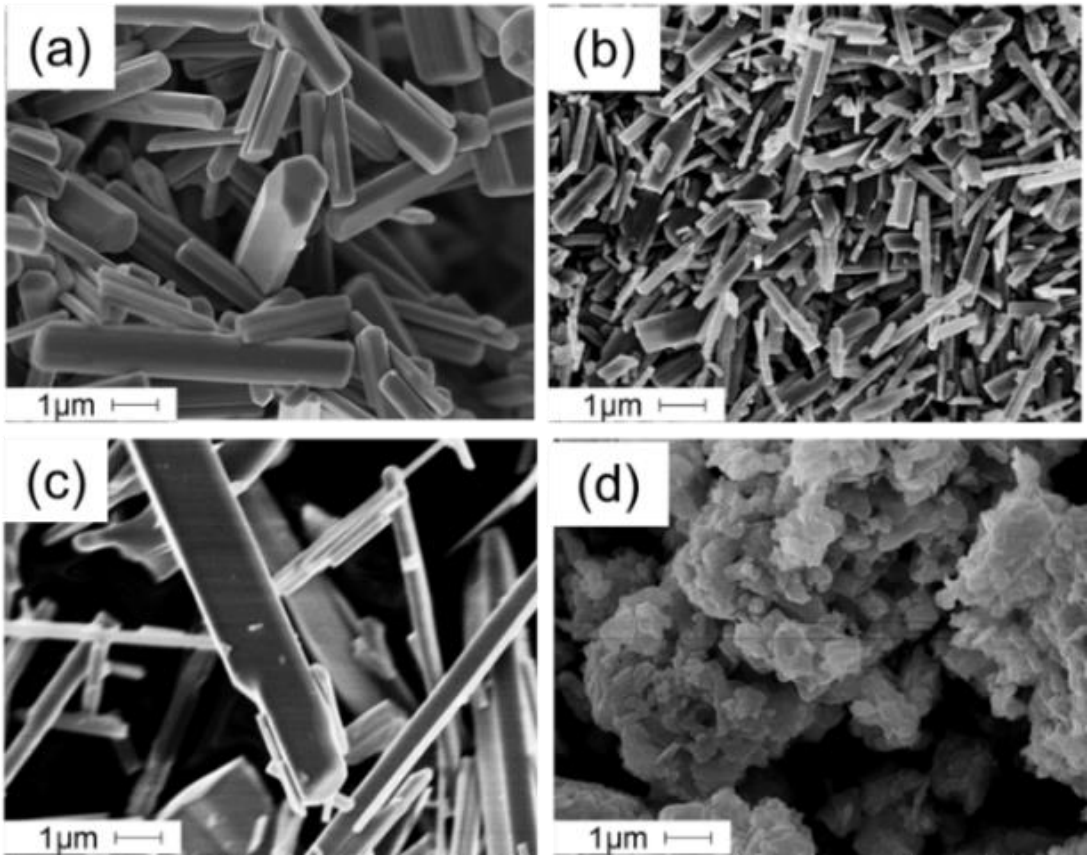


Fig. **4** DR UV-vis spectra(B) of prepared ATO samples; (a) NTO (*NaCl*), (b) KTO (*KCl*), (c)RTO (*RbCl*) and CTO (*SSR*).

In Fig. 5, the activity tests of pure alkali hexatitanates on $CO_2$ reduction were conducted over the Ag-loaded samples, where Ag cocatalyst was loaded by a PD method. Among them, compared with the RTO and CTO, the NTO and KTO samples loaded with 1.0 wt% Ag cocatalyst exhibited the higher activity for CO evolution with higher selectivity, and the 1.0 wt% Ag/KTO sample gave both the highest activity for CO evolution and the highest selectivity toward CO evolution. Therefore, further studies were focused on the KTO samples.

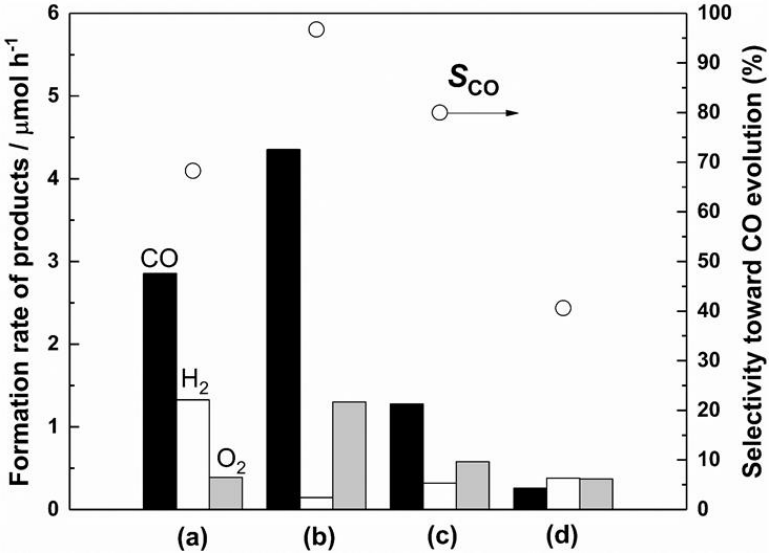


**Fig. 5** Formation rates of CO (black bar), $H_2$ (white bar), and $O_2$ (grey bar) and the $S_{CO}$ evolution (open circles) of prepared ATO samples, (a) NTO (*NaCl*), (b) KTO (*KCl*), (c)RTO (*RbCl*) and CTO (*SSR*).

## 3-3.2 Potassium hexatitanate

It was well known that molten salt as flux can regulate the crystal growth to provide a unique morphology of the crystals. In the previous study, some kinds of the salts such as LiCl, NaCl, KCl, and $CaCl_2$ were examined for the preparation of NTO samples, and it was found that the LiCl and $CaCl_2$ salts are not suitable for the preparation of $Na_2Ti_6O_{13}$ phase while only the KCl and NaCl fluxes can promote the formation of the hexagonal rod-like crystals. [20] Four catalysts were prepared by a flux method using various fluxes such as LiCl, NaCl, KCl, and $CaCl_2$. As was shown in Fig.6, some impure XRD patterns of prepared samples except the KTO(*KCl*) sample were also observed. For KTO(*NaCl*) sample, a right shift of patterns was observed, which was due to the formation of NTO instead of KTO photocatalyst, and for KTO($CaCl_2$) and KTO(*LiCl*), apart from the existence of $TiO_2$ patterns, some other impurities such as $CaTiO_3$ and $Li_xTi_{1-y}O_2$ Were also observed. The above results indicated that the raw materials used for the KTO fabrication were quite easy to react with other fluxes, which then led to the formation impurity.

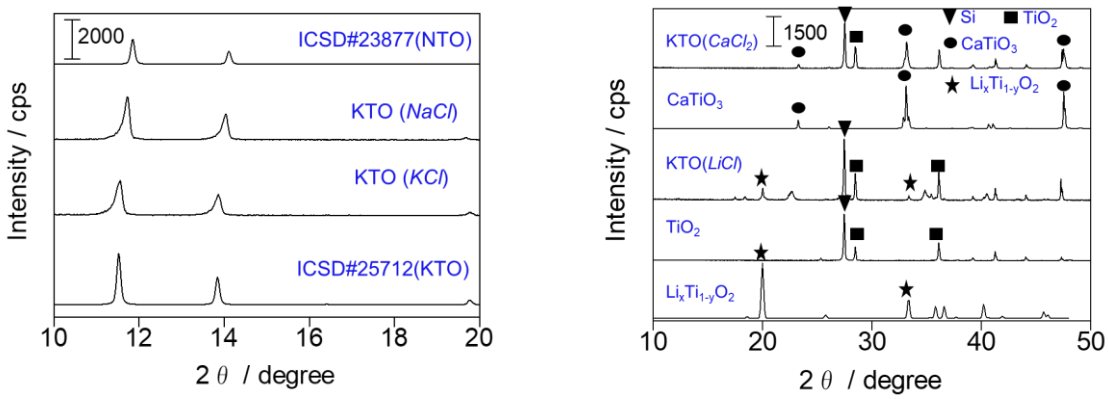


**Fig. 6** XRD patterns of prepared $K_2Ti_6O_{13}$ samples with different fluxes and some references.

The Fig. 7A showed the SEM images of these prepared samples, the rod like structure was observed over the samples, where the NaCl and KCl were used as the fluxes, since both NTO and KTO photocatalyst fabricated with proper flux were reported to form the rob like particles in our previous study.[6,20] While the morphologies of KTO(*LiCl*) and KTO(*$CaCl_2$*) were quite different. The reason could be that the fluxes, LiCl and $CaCl_2$, could react with the precursors, which indicated some impurities were produced.

The results of the photocatalytic activity tests of these samples loaded with Ag cocatalyst were shown in Fig. 7B. Compared with other three samples, the KTO(*KCl*) sample exhibited the highest activity for CO evolution, since only KCl flux could be used to prepare KTO samples without any impurity. In this section, it was concluded that the KTO sample prepared by a flux method with the pure KCl flux is the optimized one for the reduction of $CO_2$ in the improved reaction condition.

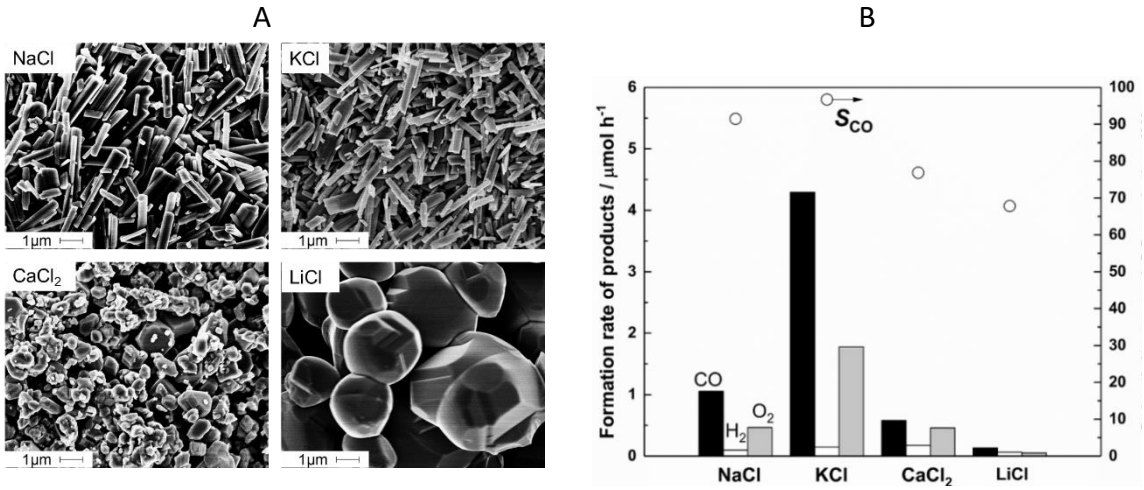


**Fig. 7** SEM images(A) and photocatalytic activity(B) of the prepared $K_2Ti_6O_{13}$ samples by a flux method with the different flux, CO (black bar), $H_2$ (white bar), and $O_2$ (grey bar) and the $S_{CO}$ evolution (open circles).

The concentration ratio of used fluxes was proved to affect the morphologies and activities of the samples.[48,50] Therefore, five samples prepared with different ratios of fluxes and the sample prepared by SSR method were compared and their activities were investigated in this section. The concentration of fluxes does not have an impact on the XRD patterns(Fig.8), but does have an impact on the morphology of the KTO samples. Fig. 9A shows SEM images of six prepared KTO samples. The morphology of the samples drastically varied with the flux concentration from 10% to 90%. In the KTO (10%) sample (Fig. 9A), there are heterogeneous granular polygonal-like particles similar to those in the KTO(*SSR*) (Fig. 9A). In the KTO (50%) sample, a small amount of short rod-like particles were observed. It is notable that the KTO samples prepared with the high concentration of fluxes consisted of fine, straight and long rod-like crystals dominantly. With increasing flux concentration, the KTO particles became more rod-like as well as the increase of length of particles, and the surface area of these samples was increased. From the results of the photocatalytic tests of $CO_2$ reduction in Fig. 9B, it was concluded that the rod-like particles were beneficial to the CO evolution, since the activity of prepared samples was enhanced when the particles became more rod-like. However, the CO evolution decreased when the concentration of KCl fluxes was higher than 70%; even the KTO samples consisted of quite fine rod-like particles. In this case, the suitable length of KTO was considered to be important for CO evolution.

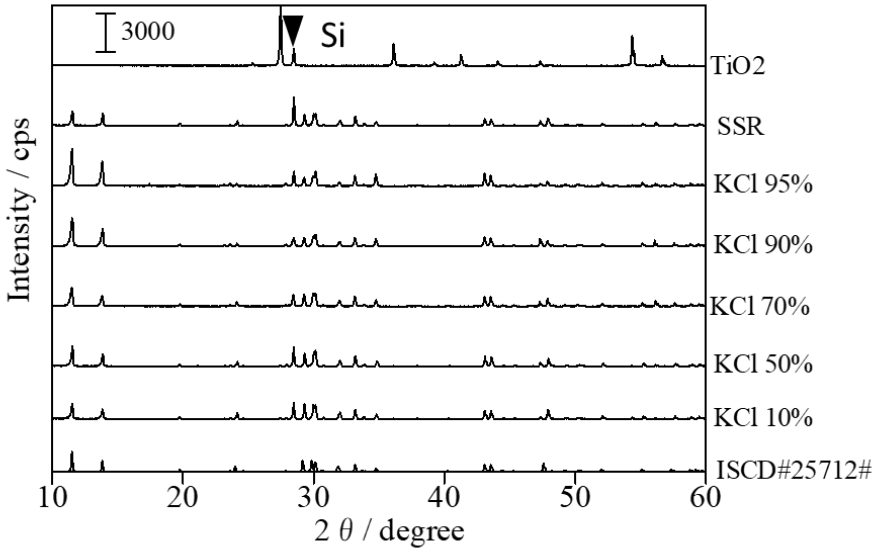


**Fig. 8** XRD patterns of prepared $K_2Ti_6O_{13}$ samples with different ratio of the KCl flux.

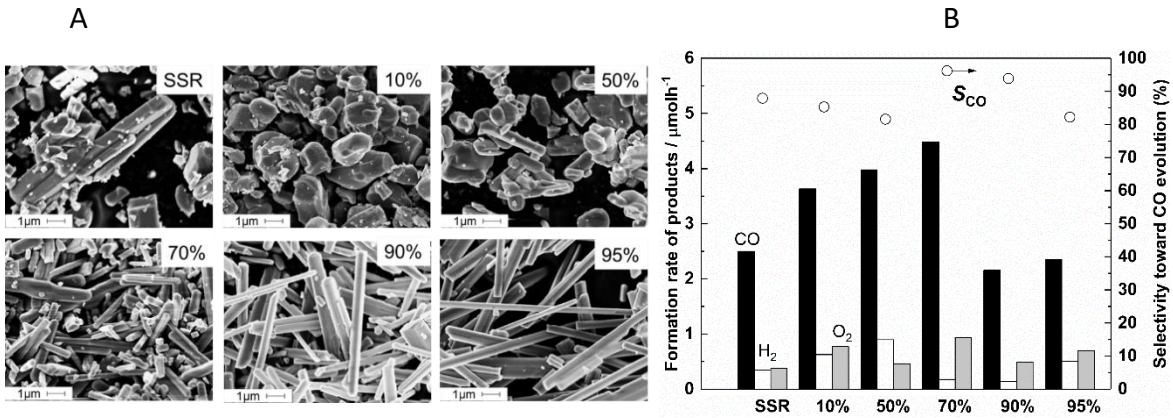


**Fig. 9** SEM images(A) and photocatalytic activity(B) of prepared KTO samples by a flux method with different molar ratio x of potassium chloride, where x [mol%] = 100 × (amount of KTO a flux [mol]) / (amount of KTO[mol] + amount of a flux [mol]), Formation rates of CO (black bar), $H_2$ (white bar), and $O_2$ (grey bar) and the $S_{CO}$ evolution (open circles).

Besides the effect of different fluxes and the ratio of involved fluxes, some researches [48,51,52] were done to discover that the morphologies and components of products are determined by the calcination condition, such as calcined temperature, calcined time and cooling rate, et.al. However, the relation between the morphology and photocatalytic activity is still unclear and difficult to explain. In the current study, several samples were prepared by a flux method at different holding temperature. As for the and the reaction tests were carried out to investigate the photocatalytic activity of $CO_2$ reduction. The results of XRD patterns were shown in the Fig. 10, and it was found that the samples prepared at the 1073 K or high than 1473 K did not

consisted of pure KTO but with the mixture of rutile $TiO_2$. This may be due to the incomplete reaction at low temperature and instability of KTO at high temperature. And the same phenomena of was observed in the DR UV-vis spectra, the spectra of $TiO_2$ was observed over the samples calcined at too high (≥1473 K) or too low (≤1073 K) temperature.

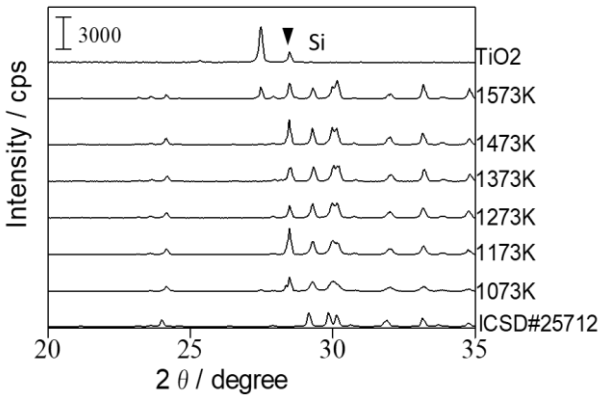


**Fig. 10** XRD patterns of prepared KTO samples by a flux method at different holding temperature.

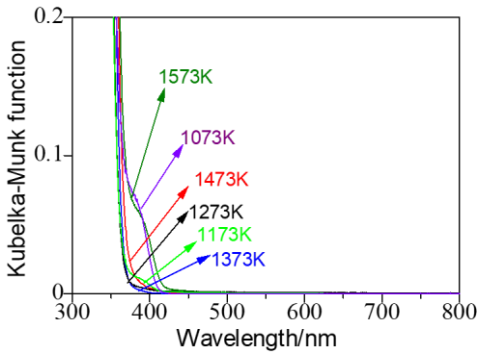


**Fig. 11** DR UV-vis spectra of prepared KTO samples by a flux method at different holding temperature.

The SEM pictures were shown in Fig. 12A, it was very clear that the particle sizes of the prepared samples became bigger as the increase of the holding temperature. In detail, both length and width were increased, and for the sample prepared at 1473 K and 1573 K, some small particles were also observed, which could arise from the existence of rutile $TiO_2$. In Fig. 6B, the photocatalytic tests' results showed that the holding temperature affected not only the morphologies of potassium hexatitanate but also the activity for $CO_2$ reduction. With the increase of the calcination temperature, the CO evolution first increased, then decreased. And the sample c prepared at 1273K exhibited not only the higher CO evolution but also the $O_2$ evolution; this may be due to the effect of morphologies of prepared KTO samples, which also was mentioned that the rod-like particles were beneficial to enhancing the photoreduction of $CO_2$ in our previous report.

A B

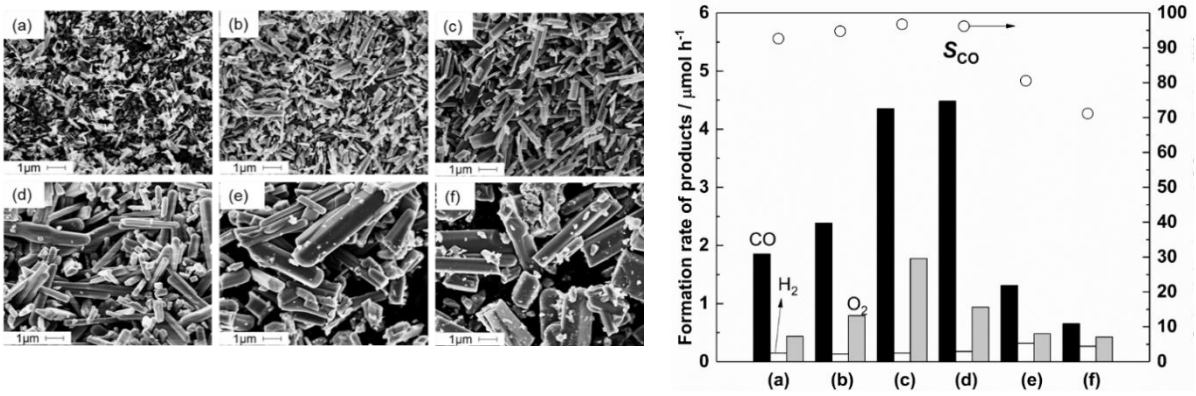


**Fig. 12** SEM images (A) and photocatalytic activity (B) of CO (black bar), $H_2$ (white bar), and $O_2$ (grey bar) and the $S_{CO}$ evolution (open circles) over the prepared KTO samples by a flux method at different holding temperature, (a)1073 K, (b)1173 K, (c)1273 K, (d)1373 K, (e)1473 K and (f)1573 K.

The effect of different calcined time, one of the important factors,[28] was also investigated in the current study. As were shown in Fig. 13 and 14, it was found 10 hours is the most suitable calcined time for the crystals to grow, and no $TiO_2$ was observed over the KTO sample calcined for 10 hours. While some impurity spectra corresponded to the $TiO_2$ was observed over other sample in Fig. 14. In Fig.15, the SEM images showed that the very similar rod like particles were fabricated, but the KTO sample calcined for 10 h consisted of quite uniform particles, and this may be one reason for its highest photocatalytic activity for $CO_2$ reduction with $H_2O$ shown in Fig. 16.

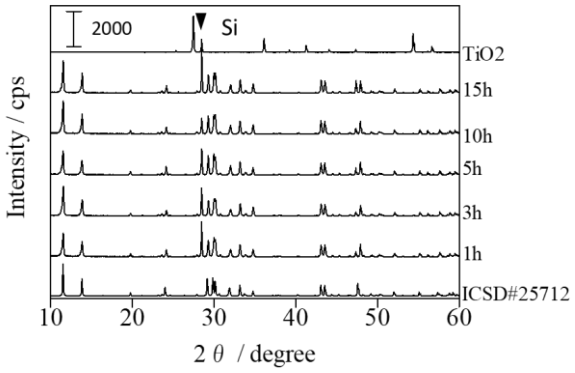


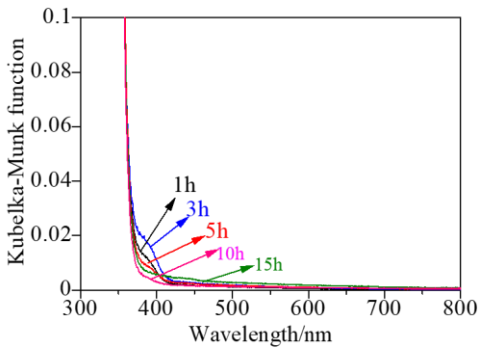


**Fig. 13** XRD patterns of prepared KTO samples by a flux method at different holding temperature.

**Fig. 14** DR UV-vis spectra of prepared KTO samples by a flux method at different holding temperature.

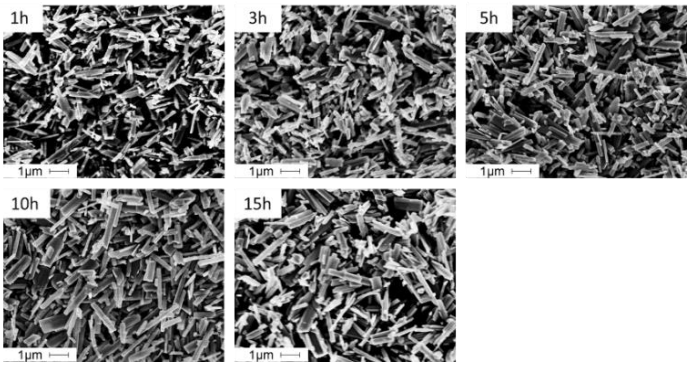


**Fig. 15** SEM images of the prepared KTO samples by a flux method at different cooling rate.

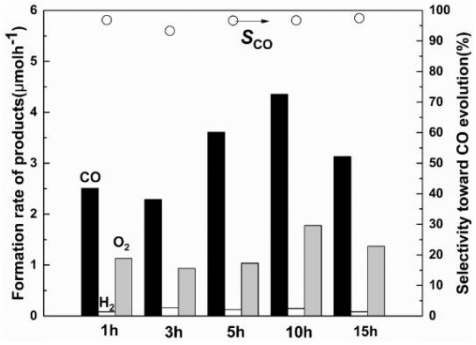


**Fig. 16** photocatalytic activity of CO (black bar), $H_2$ (white bar), $O_2$ (grey bar) and the $S_{CO}$ evolution (open circles) over the prepared KTO samples by a flux method at different cooling rate.

The cooling rate was reported to affect the growth of crystal as well in our previous studies,[6,20] and it was suggested: the solutes, $K_2CO_3$ and $TiO_2$, should be once thoroughly dissolved in enough amount of molten salt, and then the crystallization of $K_2Ti_6O_{13}$ would take place during the cooling step due to the decreasing solubility of the solutes in the flux. It is expected that this dissolution-crystallization process would provide the hexagonal rod-like crystal naturally with fewer defects and fewer crystallites boundaries. As were shown in Fig. 17 and 18, when the cooling rate varied from −25K/h to −200K/h, the morphologies of prepared samples were not obviously different from each other, and the sample prepared by a flux method with −100K/h cooling rate exhibited the highest activity, although it is still difficult to explain the reason exactly.

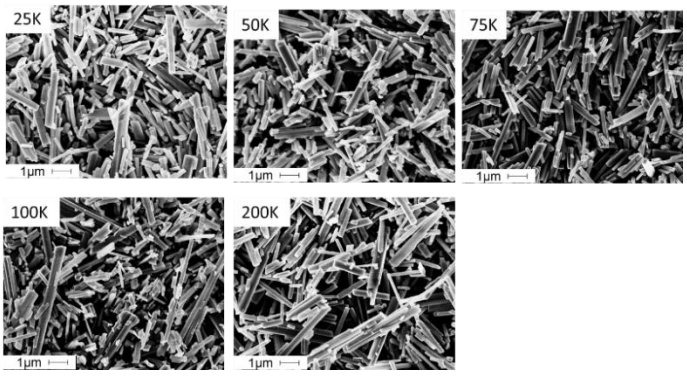


**Fig. 17** SEM images of the prepared KTiO samples by a flux method at different cooling rate.

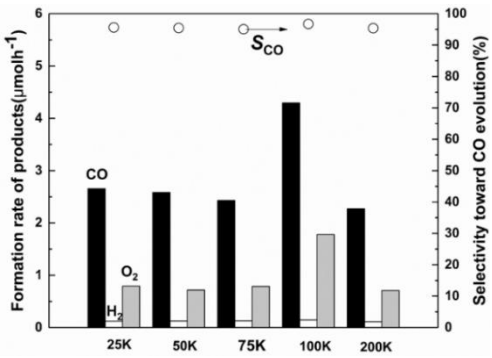


**Fig. 18** photocatalytic activity of CO (black bar), $H_2$ (white bar), $O_2$ (grey bar) and the $S_{CO}$ evolution (open circles) over the prepared KTO samples by a flux method at different cooling rate.

## 3.3 Ag cocatalyst

The state and local structure of the dual cocatalyst were estimated by using X-ray absorption fine structure (XAFS). Fig. 19 shows Ag K-edge X-ray absorption near edge structures (XANES) of the prepared samples and two reference samples. The absorption edges (25519 eV) in the spectra of the Ag/KTO samples before and after reaction were consistent with that of Ag foil (25519 eV) but different from that of $Ag_2O$ (25521 eV). This indicates that the metallic Ag nanoparticles are dispersed on the surface of KTO samples.

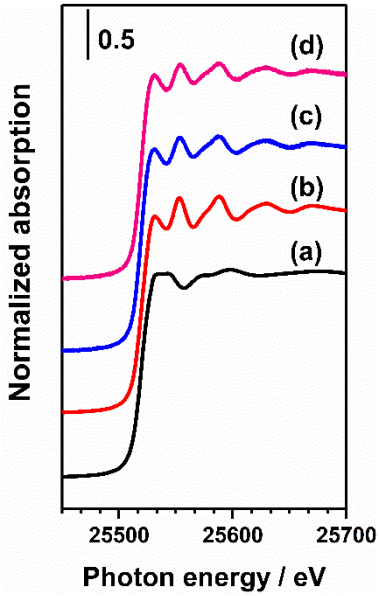


**Fig. 19** Ag K-edge XANES of (a) $Ag_2O$, (b) Ag foil, (c) Ag/KTO_before reaction, and (d) Ag/KTO_after reaction.

The mophology of the prepared samples was recorded by SEM and TEM shown Fig. 20. For bare KTO sample (Fig. 20a), very clear facets were observed. For the Ag/KTO sample (Fig. 20b), Ag nanoparticles were found to deposit on the long facets of the KTO sample, and Ag nanoparticles with the average size of ca. 15 nm were observed(Fig. 20c).

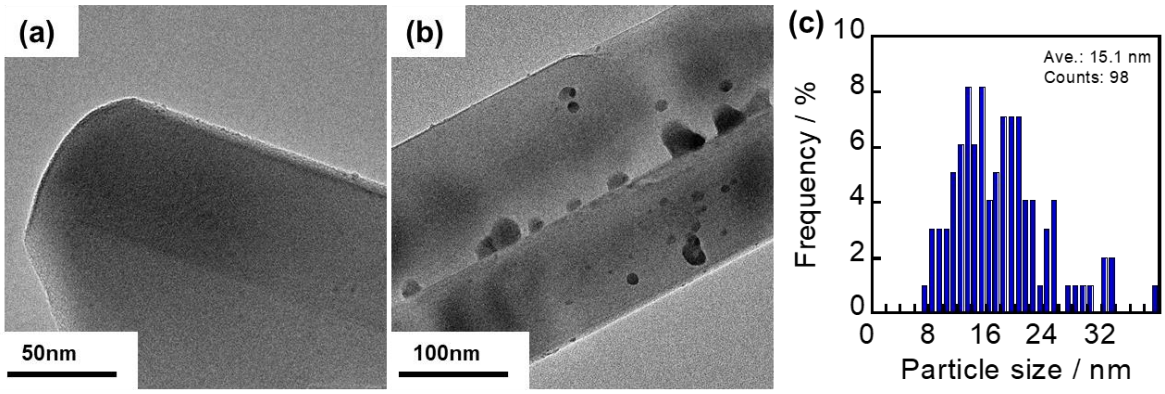


**Fig. 20** TEM images of the prepared samples, (a) bare KTO, (b) Ag/KTO, and (c) size dirtibution of Ag cocatalyst of Ag/KTO.

## 3-3.3 Correlation between photocatalytic activity, aspect ratio and surface area

It was believed that the hexagonal rod-like crystals might be highly active for the photocatalysis since they have the proper surfaces and fewer defects, and the aspect ratio or crystallize size

of some active facets are very significant. Thus, the correlation between the photocatalytic activity with aspect ratio and crystallize size were analyzed in this study, however, the results shown in Fig. 21 indicated that no strong relationship was found in this case. However, the average length and width were ca. 1.25 μm and ca. 0.25 μm of the optimized KTO sample according to the SEM images, respectively1.

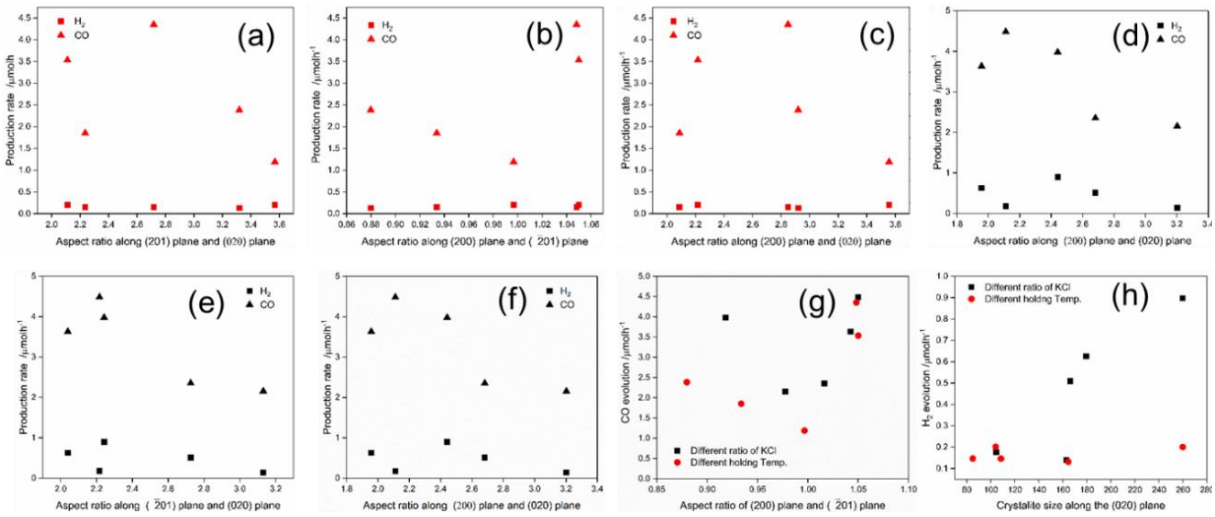


**Fig. 21** Correlation between formation rate of CO and $H_2$ and aspect ratio, or crystallize size of some facets, (a)-(c) samples prepared at different holding temperature, (d)-(f) samples prepared with different ratio of KCl flux, (g) summary of these two groups.

As was discussed in the previous part, the photocatalytic reactions occurred on the surface of photocatalyst. Here too small surface area could limit the number of active electrons and holes and cannot provide enough active sites for the target reaction, while too large surface area could lead to the increase of recombination of photogenerated electrons and holes, which lead to the decrease of photocatalytic activity. The correlation between the surface area and the CO evolution rate over two prepared sample groups was also built in Fig. 22, and it was found that the optimized surface area was around 4 $m^2g^{-1}$, samples with the surface area lower than or high than this value exhibited lower activity.

The time course of $CO_2$ reduction over the KTO sample prepared under the optimized condition with 1 wt% loading amount of Ag cocatalyst was shown in Fig. 23, the Ag/KTO sample consisting of the suitable size of rod-like KTO crystals prepared at 1273 K with holding time of 10 h gave the highest activity for CO evolution and the highest selectivity toward CO (96%),

with the moderately high $O_2$ evolution rate after the induction period, the ratio of $e^-/h^+$ became closed to unity (1.3) after 4 h. This is superior to the $Na_2Ti_6O_{13}$ crystals of similar rod-like structure.[23]

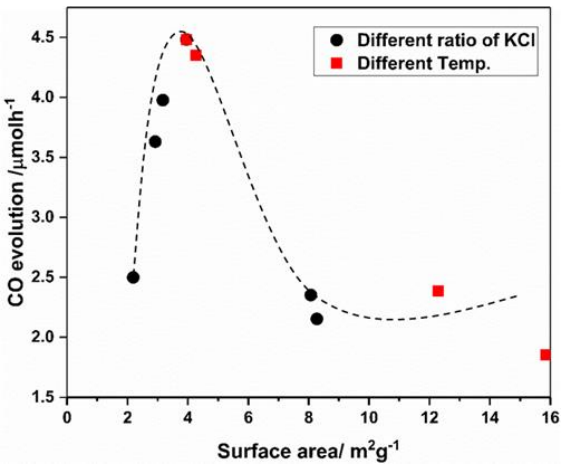


**Fig. 22** The correlation of the surface area and formation rate of CO of prepared samples.

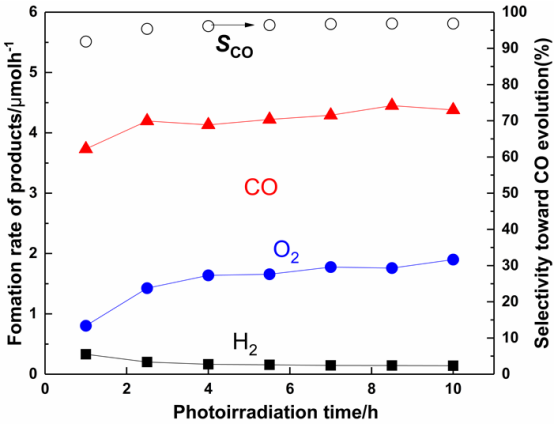


**Fig. 23** The time course of the KTO sample prepared under the optimized condition loaded with 1 wt% Ag cocatalyst by a PD method.

## 3-4 Conclusion

As a summary in this section, after comparing four types of alkali titanates, the further development of potassium hexatitanate photocatalyst prepared in the flux method was examined. KTO samples prepared with different ratios of KCl flux gave quite different morphology of crystals, and the KTO sample prepared with 70% KCl consisting of rod-like particles showed higher activity than the others. With the increase of holding temperature, both the length and size of KTO particles increased, and when the holding temperature was at 1523 K and higher or holding time is less than 5 h, $TiO_2$ particles were observed as an impurity phase in SEM images, which gave negative effect on the photocatalytic activity of the $CO_2$ reduction. As a result, the metallic Ag loaded KTO sample consisting of the suitable size of rod-like KTO crystals prepared at 1273 K with holding time of 10 h gave the highest activity for CO evolution and the highest selectivity toward CO (96%), which is superior to the $Na_2Ti_6O_{13}$ catalyst of similar rod-like structure. In addition, although the $Na_2Ti_6O_{13}$ catalyst showed a long induction period to produce oxygen with enough production rate compared to that expected

from the production rates of CO and $H_2$ in our previous study, the KTO sample produced expected amount of $O_2$ after only a shorter induction period, i.e., the ratio of $e^-/h^+$ became close to 1 after 4 h.

## References


1 B. L. Wang, Q. Chen, J. Hu, H. Li, Y. F. Hu and L. M. Peng, *Chem. Phys. Lett.*, 2005, **406**, 95–100.

2 Q. Zhang, Y. Guo, K. Guo, T. Zhai and H. Li, *Chem. Commun.*, 2016, **52**, 6229–6232.

3 Y. Cao, K. Zhu, J. Du, J. Liu and J. Qiu, *Res. Chem. Intermed.*, 2015, **41**, 4851–4859.

4 K. Byrappa, S. Gali, B. M. R. Wanklyn, A. B. Kulkarni, S. K. Patil and G. Narendranath, *J. Mater. Sci. Lett.*, 1990, **9**, 898–900.

5 J. C. Pérez-Flores, F. García-Alvarado, M. Hoelzel, I. Sobrados, J. Sanz and A. Kuhn, *Dalt. Trans.*, 2012, **41**, 14633–14642.

6 H. Yoshida, M. Takeuchi, M. Sato, L. Zhang and T. Teshima, *Catal. Today*, 2014, **232**, 158–164.

7 A. Kudo and T. Kondo, *J. Mater. Chem.*, 1997, **7**, 777–780.

8 C. Y. Xu, J. Wu, P. Zhang, S. P. Hu, J. X. Cui, Z. Q. Wang, Y. D. Huang and L. Zhen, *CrystEngComm*, 2013, **15**, 3448–3454.

9 S. Ogura, M. Kohno, K. Sato and Y. Inoue, *Appl. Surf. Sci.*, 1997, **121**–**122**, 521–524.

10 J. K. Lee, K. H. Lee and H. Kim, *J. Mater. Sci.*, 1996, **31**, 5493–5498.

11 G. L. Li, G. H. Wang and J. M. Hong, *Mater. Res. Bull.*, 1999, **34**, 2341–2349.

12 N. Bao, X. Feng, X. Lu and Z. Yang, *J. Mater. Sci.*, 2002, **37**, 3035–3043.

13 L. Xu and L. Cheng, *Mater. Charact.*, 2010, **61**, 245–248.

14 Q. Wang, S. Guan and B. Li, *Catal. Sci. Technol.*, 2017, **7**, 4064–4078.

15 T. Zhang, Q. Chen and L. M. Peng, *Adv. Funct. Mater.*, 2008, **18**, 3018–3025.

16 Y. HAKUTA, K. SHIMOYACHI, H. HAYASHI and K. ARAI, *J. Ion Exch.*, 2003, **14**, 393–396.

17 S. O. Kang, H. S. Jang, Y. Il Kim, K. B. Kim and M. J. Jung, *Mater. Lett.*, 2007, **61**, 473–477.

18 M. A. Siddiqui, V. S. Chandel and A. Azam, *Appl. Surf. Sci.*, 2012, **258**, 7354–7358.

19 J. P. Remeika, *J. Am. Chem. Soc.*, 1954, **76**, 940–941.

20 H. Yoshida, M. Sato, N. Fukuo, L. Zhang, T. Yoshida, Y. Yamamoto, T. Morikawa, T. Kajino, M. Sakano, T. Sekito, S. Matsumoto and H. Hirata, *Catal. Today*, 2018, **303**, 296–304.

21 X. Zhu, A. Anzai, A. Yamamoto and H. Yoshida, *Appl. Catal. B Environ.*, 2019, **243**, 47–56.

22 C. Y. Xu, J. Wu, P. Zhang, S. P. Hu, J. X. Cui, Z. Q. Wang, Y. D. Huang and L. Zhen, *CrystEngComm*, 2013, **15**, 3448–3454.

23 X. ZHU, A. Yamamoto, S. Imai, A. Tanaka, H. Kominami and H. Yoshida, *Chem. Commun.*, DOI:10.1039/c9cc06038c.

24 H. Yoshida, L. Zhang, M. Sato, T. Morikawa, T. Kajino, T. Sekito, S. Matsumoto and H. Hirata, *Catal. Today*, 2015, **251**, 132–139.

25 A. Anzai, N. Fukuo, A. Yamamoto and H. Yoshida, *Catal. Commun.*, 2017, **100**, 134–138.

26 D. Arney, B. Porter, B. Greve and P. A. Maggard, *J. Photochem. Photobiol. A Chem.*, 2008, **199**, 230–235.

27 Q. Wang, T. Hisatomi, Y. Moriya, K. Maeda and K. Domen, *Catal. Sci. Technol.*, 2013, **3**, 2098–2103.

28 Z. Huang, K. Teramura, S. Hosokawa and T. Tanaka, *Appl. Catal. B Environ.*, 2016, **199**, 272–281.

29 Z. Huang, S. Yoshizawa, K. Teramura, H. Asakura, S. Hosokawa and T. Tanaka, *ACS Omega*, 2017, **2**, 8187–8197.

30 T. Ohno, K. Sarukawa and M. Matsumura, *New J. Chem.*, 2002, **26**, 1167–1170.

31 K. Iizuka, T. Wato, Y. Miseki, K. Saito and A. Kudo, *J. Am. Chem. Soc.*, 2011, **133**, 20863–20868.

32 M. Halmann, *Nature*, 1978, 275, 115–116.

33 M. Asadi, B. Kumar, A. Behranginia, B. A. Rosen, A. Baskin, N. Repnin, D. Pisasale, P. Phillips, W. Zhu, R. Haasch, R. F. Klie, P. Král, J. Abiade and A. Salehi-Khojin, *Nat. Commun.*, 2014, **5**, 1–8.

34 J. C. Hemminger, R. Carr and G. A. Somorjai, *Chem. Phys. Lett.*, 1978, **57**, 100–104.

35 S. N. Habisreutinger, L. Schmidt-Mende and J. K. Stolarczyk, *Angew. Chemie - Int. Ed.*, 2013, **52**, 7372–7408.

36 T. Arai, S. Sato, T. Kajino and T. Morikawa, *Energy Environ. Sci.*, 2013, **6**, 1274–1282.

37 S. Sato, T. Arai, T. Morikawa, K. Uemura, T. M. Suzuki, H. Tanaka and T. Kajino, *J. Am. Chem. Soc.*, 2011, **133**, 15240–15243.

38 O. Ishitani|, C. Inoue, Y. Suzuki and T. Ibusuki, *J. Photochem. Photobiol. A Chem.*, 1993,

**72**, 269–271.

39 A. Nakada, T. Nakashima, K. Sekizawa, K. Maeda and O. Ishitani, *Chem. Sci.*, 2016, **7**, 4364–4371.

40 S. C. Roy, O. K. Varghese, M. Paulose and C. A. Grimes, *ACS Nano*, 2010, **4**, 1259–1278.

41 M. Yamamoto, T. Yoshida, N. Yamamoto, H. Yoshida and S. Yagi, *e-Journal Surf. Sci. Nanotechnol.*, 2014, **12**, 299–303.

42 N. Yamamoto, T. Yoshida, S. Yagi, Z. Like, T. Mizutani, S. Ogawa, H. Nameki and H. Yoshida, *e-Journal Surf. Sci. Nanotechnol.*, 2014, **12**, 263–268.

43 M. Yamamoto, T. Yoshida, N. Yamamoto, T. Nomoto, Y. Yamamoto, S. Yagi and H. Yoshida, *J. Mater. Chem. A*, 2015, **3**, 16810–16816.

44 T. Takayama, K. Tanabe, K. Saito, A. Iwase and A. Kudo, *Phys. Chem. Chem. Phys.*, 2014, **16**, 24417–24422.

45 Z. Wang, K. Teramura, S. Hosokawa and T. Tanaka, *Appl. Catal. B Environ.*, 2015, **163**, 241–247.

46 S. Xie, Y. Wang, Q. Zhang, W. Deng and Y. Wang, *Chem. Commun.*, 2015, **51**, 3430–3433.

47 R. Pang, K. Teramura, H. Asakura, S. Hosokawa and T. Tanaka, *Appl. Catal. B Environ.*, 2017, **218**, 770–778.

48 H. Yoshida, M. Takeuchi, M. Sato, L. Zhang, T. Teshima and M. G. Chaskar, *Catal. Today*, 2014, **232**, 158–164.

49 I. E. Grey, I. C. Madsen, J. A. Watts, L. A. Bursill and J. Kwiatkowska, *J. Solid State Chem.*, 1985, **58**, 350–356.

50 Z. Huang, K. Teramura, H. Asakura, S. Hosokawa and T. Tanaka, *Catal. Today*, 2018, **300**, 173–182.

51 N. Bao, X. Feng, X. Lu and Z. Yang, *J. Mater. Sci.*, 2002, **37**, 3035–3043.

52 N. Bao, X. Feng, L. Shen and X. Lu, *Cryst. Growth Des.*, 2002, **2**, 437–442.

# Chapter 4 A silver-manganese dual cocatalyst for selective reduction of carbon dioxide into carbon monoxide over a potassium hexatitanate photocatalyst with water


## Abstract

A Ag-Mn dual cocatalyst deposited on a $K_2Ti_6O_{13}$ photocatalyst significantly enhances photocatalytic $CO_2$ reduction into CO by water with extremely high selectivity such as 98% by using $H_2O$ as an electron donor, owing to the properties of Ag and $MnO_x$ species for promoting CO and $O_2$ formation, respectively.


## 4-1 Introduction

In recent years, the photocatalytic reduction of $CO_2$ with water into useful compounds has been widely studied to achieve less $CO_2$ emission for global environmental issues and utilization of $CO_2$ as a carbon source. Various heterogeneous photocatalysts have been reported for the reduction of $CO_2$ with water to produce formate, CO, $CH_3OH$, and $CH_4$.[1-4] Among these possible reductive products from $CO_2$, the most useful product would be CO since it is a valuable chemical intermediate for further chemical syntheses and easily separable from the aqueous reaction media to the gas phase.

In the typical photocatalytic $CO_2$ reduction system in aqueous solution, two reactions competitively can occur, i.e., photocatalytic reduction of $CO_2$ to form CO and photocatalytic water splitting into $H_2$ and $O_2$, where the reductive products are CO and $H_2$, respectively, and the common oxidative product is $O_2$.[5]

But, the redox potential of $H^+/H_2$ is more positive than that of $CO_2/CO$, so the reduction of protons ($H^+$) to $H_2$ is thermodynamically easier than that of $CO_2$ to CO. Thus, it seems especially challenging to reduce only $CO_2$ molecules selectively in an aqueous solution in principle. Recently, it was discovered that deposited Ag nanoparticles could function as the active cocatalyst for $CO_2$ reduction to form CO.[5] Recently, many kinds of Ag-modified photocatalysts to produce CO, $H_2$ and $O_2$ have been reported, such as $Ag/BaLa_4Ti_4O_{15}$,[5] $Ag/Ga_2O_3$,[6-8] $Ag/La_2Ti_2O_7$,[9] and so on.[10-12] Although some developed photocatalysts exhibited high activity

or high selectivity for the $CO_2$ reduction,[13,14] the efficiency has not been high enough to put into practice still now. As for the selectivity toward CO evolution, although it was less than 70% several years ago,[5] it has become higher such as 94% with $Ag/CaTiO_3$[15] and 96% over $Ag/SrNb_2O_6$[16]quite recently. It is noted that, in some cases, as was discussed in our previous paper,[17]the $O_2$ evolution was not always stoichiometric both in water splitting and $CO_2$ reduction. Many reported papers had proposed the possible reasons for the nonstoichiometric formation of $O_2$, such as high overpotential required for $O_2$ evolution and some side reactions.[17-22] It has also been reported that some metal oxides (such as $IrO_2$, $RuO_2$, $CoO_x$, $MnO_x$, etc.) can act as the water oxidation cocatalyst for water splitting but rarely for $CO_2$ reduction so far.[23,24]

In these years, some dual cocatalysts with proper structures including core-shell type and two separated metal/oxide particles, such as Ag/Cu,[25] $Pt/Cu_2O$,[26] $Ag/CrO_x$,[27] and Cr/Rh[28] have been proved to enhance the activity of $CO_2$ conversion or water splitting by taking advantage of the synergistic function of dual active sites for both reductive and oxidative reactions simultaneously, or the modification of the cocatalyst surface suppressing the backward reaction.[27-29] Recently, a combination of Ag and Mn was examined as a dual cocatalyst deposited on $TiO_2$ photocatalyst to promote CO formation from a mixture of $NaHCO_3$ and $H_2SO_4$ in an aqueous solution although $O_2$ evolution and selectivity toward CO evolution were not clearly mentioned.[30]

In the present study, we examined potassium hexatitanate ($K_2Ti_6O_{13}$, referred to as KTO), which is one of the well-known functional materials with wide applications in many fields such as, electrochemistry,[31,32] ion exchange,[33] and photocatalyst,[34-37] and has been modified with each typical cocatalyst to be studied as a photocatalyst for steam reforming of methane,[34] water splitting,[35,36] and dye degradation.[37] Here, we found for the first time that deposition of a Ag-Mn dual cocatalyst on a KTO photocatalyst can much improve the photocatalytic $CO_2$ reduction into CO by using $H_2O$ as an electron donor with a very high CO selectivity of 98% among the reductive products.

# 4-2 Experimental

## 4-2.1 Photocatalyst preparation

Potassium titanate ($K_2Ti_6O_{13}$, KTO) sample was prepared by a flux method.[17] The precursors,

$K_2CO_3$ (Kishida) and $TiO_2$ (rutile, Kojundo), and a flux reagent KCl (Kishida) were mixed, where the molar ratio of $K_2CO_3$ to $TiO_2$ was 1:6, and that of KTO to KCl was 3:7. The mixture was put into a platinum crucible, heated in an electric muffle furnace with a rate of 200 K $h^{-1}$ to 1273 K, held at this temperature for 10 h, and then cooled down at a rate of −100 K $h^{-1}$ to 773 K, followed by being naturally cooled to room temperature in the furnace. The obtained powder was thoroughly washed with hot water (353 K, 500 mL) for 15 minutes and filtrated, and this washing step was repeated 4 times to remove the residual salt, then dried at 323 K for 24 hours.

Dual cocatalysts were loaded on the surface by a facile simultaneous photodeposition (PD) method.[27] Here, 1 g of the $K_2Ti_6O_{13}$ sample was dispersed in 400 mL of ion-exchanged water containing a required amount of precursors ($AgNO_3$, $Cr(NO_3)_2$, $Mn(NO_3)_2$, $Co(NO_3)_2$, and $Ni(NO_3)_2$, $PdCl_2$, $HAuCl_4$), and a bubbling flow of Ar gas was used to exclude the air for 1 hour before photoirradiation. Then the suspension was photoirradiated from a 100 W high-pressure Hg lamp with a bubbling flow of Ar gas for 3 h, followed by filtration and drying at room temperature.

## 4-2.2 Characterization

The loading amount of cocatalyst on the samples was evaluated by X-ray florescence analysis with an EDX-8000 (Shimadzu) using each experimentally obtained calibration curve, where the samples loaded by an impregnation method were used as references. Even if the desired amount of the source compound was used, the actually loaded amount of cocatalyst was much less than the desired value for some elements such as Cr, Mn, Co, and Ni, which would be very sensitive to the conditions. The samples are referred to as Ag(*x*)-M(*y*)/KTO, where *x* and *y* mean the actual loading amount of Ag and M (wt %) determined by XRF.

The crystal structure of the samples was determined by powder X-ray diffraction with a Lab X XRD-6000 (Shimazu). Morphologies of the samples were observed by scanning electron microscopy (SEM) with a JSM-890 (JEOL). Images of transmission electron microscopy (TEM) and scanning transmission electron microscopy (STEM) were taken by a JEOL JEM-2100F at 200 kV in the Joint Research Center of Kindai University. The sample was dispersed in methanol, dropped onto a carbon-coated copper grid, and dried at ambient temperature for 5 h. Diffuse reflectance UV-Vis spectrum was recorded by a V-670 (JASCO). Ag and Mn K-edge X-ray absorption fine structure (XAFS) were measured at NW-10C and BL-12C of the Photon Factory

(KEK, Tsukuba, Japan), respectively. Most of the samples including the references were measured in a transmission mode, while the Mn K-edge XAFS spectra of the Mn(0.15)/KTO and Ag(1.0)-Mn(0.09)/KTO samples were measured in a fluorescence mode due to the extremely low amount of Mn species.

### 4-2.3 Photocatalytic reaction

The photocatalytic activity test of $CO_2$ reduction with water was carried out using a flow system with an inner-irradiation-type reaction vessel,[15] as was shown in Fig. 1. Typical reaction conditions are as follows: The photocatalyst powder sample (0.3 g) was dispersed in ion-exchanged water (400 mL) containing 0.5 M $NaHCO_3$ (pH=7), and suspended by magnetically stirring. Then, $CO_2$ was bubbled into the solution at a flow rate of 30 mL $min^{-1}$ without irradiation for 1.5 hours. The photocatalytic reaction was conducted using a 100 W high-pressure mercury lamp. The light intensity was measured to be 22 mW $cm^{-2}$ at a detecting wavelength of 254±10 nm. The reaction temperature was set at 290 K with cooling water. The amount of the products ($H_2$, $O_2$, and CO) in the outlet gas from the reactor were determined by using an on-line gas chromatograph (Shimadzu, GC-8A, TCD, a Shincarbon ST column, argon carrier). In most cases, CO, $H_2$ and $O_2$ were produced under photoirradiation.

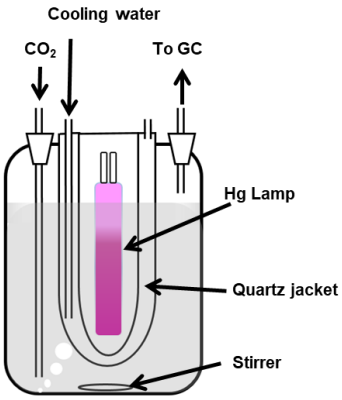


**Fig. 1** The reactor set−up for the photocatalytic reaction test for $CO_2$ reduction with water under photoirradiation.

## 4-3 Result and Discussion

### 4-3.1 XRD and SEM image of potassium hexatitanate

Fig. 2 shows XRD patterns of the obtained KTO sample and a $K_2Ti_6O_{13}$ reference from a database (ICSD#25712). The XRD pattern of the prepared KTO sample was consistent with that

of the reference. It gives a correct diffraction pattern and no diffraction lines corresponding to other impurity phases, confirming that the prepared potassium hexatitanate was correctly fabricated by the flux method. The SEM image revealed that the samples consisted of rod-like crystals (Fig. 3), confirming that the molten salt flux can enhance the crystallization and regulate the crystal growth of each facet to form the unique hexagonal rod-like morphology of alkali hexatitanates.[35] The bandgap of the bare KTO was estimated to be 3.56 eV by a diffuse reflectance (DR) UV-visible spectrum and the Davis–Mott equation.[38]

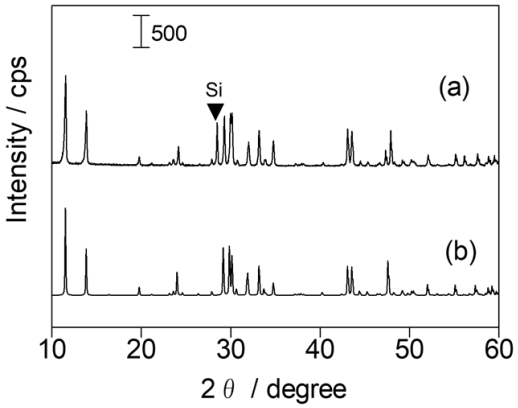


**Fig. 2** XRD patterns of (a) the prepared KTO sample and (b) a reference data #25712 from ICSD database for $K_2Ti_6O_{13}$. A closed triangle indicates a diffraction from silicon powder mixed with the KTO sample to calibrate the angle.

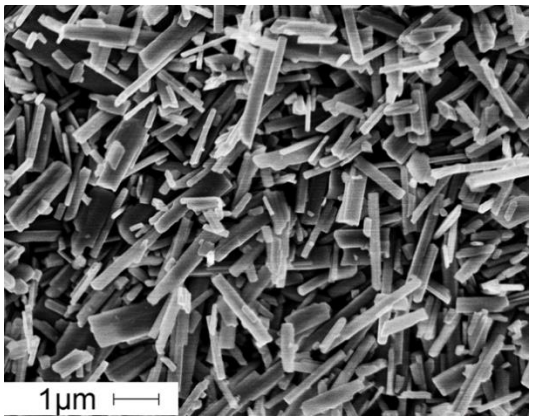


**Fig. 3** SEM image of the prepared KTO sample.

## 4-3.2 Photocatalytic reaction tests

Since no other reductive products than CO and $H_2$ were observed, the selectivity toward CO evolution, $S_{CO}(\%) = 100 \times R_{CO}/(R_{CO} + R_{H2})$, and the ratio of the consumed electron and hole, $R(e^-/h^+) = (R_{CO} + R_{H2})/2R_{O2}$, were calculated,[17] where $R_{CO}$, $R_{H2}$, and $R_{O2}$ present the production rate of CO, $H_2$, and $O_2$, respectively. The results of photocatalytic reaction tests over eight samples loaded with different cocatalysts were shown in Fig. 4. The Ag(1.0)/KTO sample produced CO with high selectivity ($S_{CO}$=94.8%). The samples with the Ag-Pd, Ag-Au, or Ag-Cu dual cocatalyst produced $H_2$ preferably, and other samples with the Ag-Cr, Ag-Ni, Ag-Co, or Ag-Mn dual cocatalyst formed predominantly CO with high selectivity more than 85%. As was well known, the precious metal cocatalysts, such as Pd and Pt cotatalyst,[39] are very beneficial to

the $H_2$ evolution, while the transition metal oxide cocatalysts such as $MnO_x$ and $CrO_x$ exhibit high activity for $O_2$ evolution.[40,41] In the current study, only the Ag(1.0)-Mn(0.09)/KTO sample exhibited higher CO formation rate than the Ag(1.0)/KTO sample, with the highest selectivity ($S_{CO}$=97.2%). In the present study the cocatalysts were loaded by a photodeposition method and the real loading amount of $CrO_x$, $CoO_x$ and NiOx were very limited. Thus, the deposition method and the amount of cocatalysts deposited are supposed to the possible reasons for low activity. This remains further possibilities that other transition metal oxide species might exhibit high performance after each optimization.

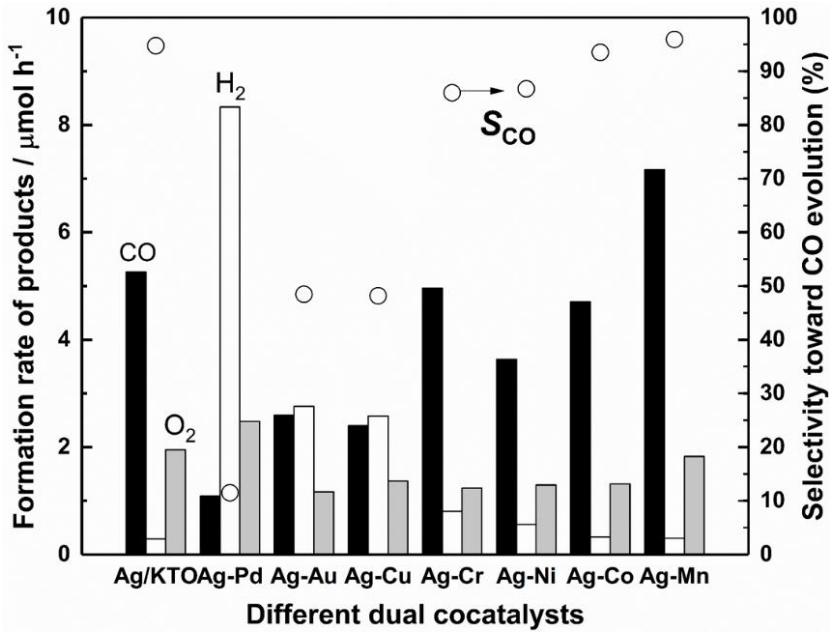


**Fig. 4** Formation rates of CO (black bar), $H_2$ (white bar), and $O_2$ (grey bar) and the $S_{CO}$ (open circles) in the photocatalytic $CO_2$ reduction with $H_2O$ over the prepared KTO samples, (a) Ag(1.0)/KTO, (b) Ag(1.0)-Pd(1.0)/KTO, (c) Ag(1.0)-Au(0.85)/KTO, (d) Ag(1.0)-Cu(1.0)/KTO, (e) Ag(1.0)-Cr(0.006)/KTO, (f) Ag(1.0)-Ni(0.02)/KTO, (g) Ag(1.0)-Co(0.02)/KTO, and (h) Ag(1.0)-Mn(0.09)/KTO.

The photocatalytic reaction tests were conducted for the Ag-Mn/KTO samples with different Ag loading amount (Fig. 5). Although the same amount of Mn was added, the actually loaded amount of Mn was varied with the loading amount of Ag cocatalyst. It was found that the formation rate of CO first increased then decreased with the increasing loading amount of Ag cocatalyst. The samples with moderate loading amount in the range of 0.5–2.0 wt% of Ag and 0.10-0.13 wt% of Mn (Fig. 5, e–g) exhibited high photocatalytic activity for CO evolution. When the Ag loading amount is more than 2 wt%, the Ag particles would aggregate and the

photocatalytic activity of $CO_2$ reduction would decrease.

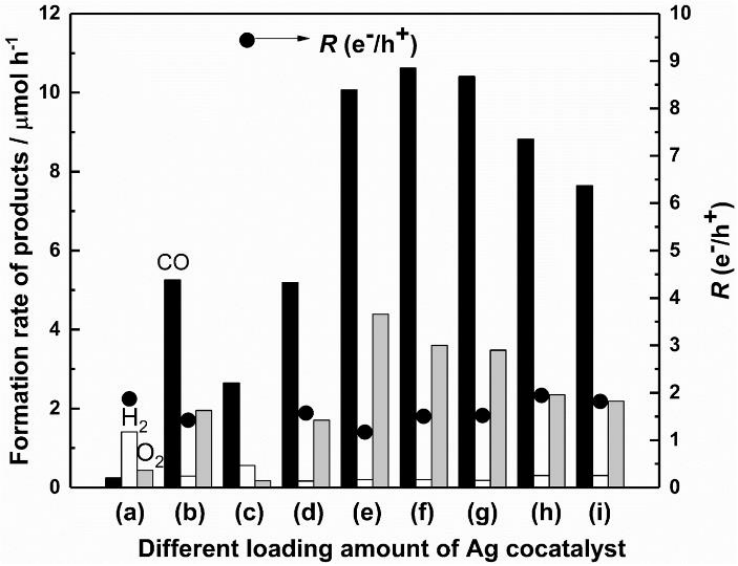


**Fig. 5** Formation rate of CO, $H_2$, and $O_2$ and $R(e^-/h^+)$ in the photocatalytic $CO_2$ reduction over the Ag-Mn/KTO samples loaded with different amount of Ag cocatalyst, (a) bare KTO, (b) Ag(1.0)/KTO, (c) Ag(0.1)-Mn(0.21)/KTO, (d) Ag(0.3)-Mn(0.14)/KTO, (e) Ag(0.5)-Mn(0.13)/KTO, (f) Ag(1.0)-Mn(0.12)/KTO, (g) Ag(2.0)-Mn(0.10)/KTO, (h) Ag(3.0)-Mn(0.07)/KTO and (i) Ag(4.0)-Mn(0.06)/KTO.

The photocatalytic reaction tests were conducted for the Ag-Mn/KTO samples with different Mn loading amount (Fig. 6). It was found that the formation rate of CO first increased then decreased with the increasing loading amount of Mn cocatalyst, and the samples of the Mn loading amount in the range 0.12-0.14 wt% (Fig. 6, d and e) exhibited high formation rates of CO and $O_2$ with high selectivity such as 98%. Here, when the amount of $MnO_x$ is low, the enhancement of $O_2$ evolution was not enough, although the activity was improved. When a large amount of Mn was loaded, the $MnO_x$ species would aggregate and the photocatalytic activity would decrease. According to the optimization of the Ag and Mn loading amount (Fig. 5 and 6), it was found that the optimum loading amounts were in the range of 0.5–2.0 wt% for Ag and 0.10–0.13 wt% for Mn, and the Ag(1.0)-Mn(0.12)/KTO sample exhibited the highest CO production rate (10.6 μmol $h^{-1}$) with very high selectivity ($S_{CO}$=98.2%). It is noted that the selectivity toward CO evolution was the highest among the published data so far.

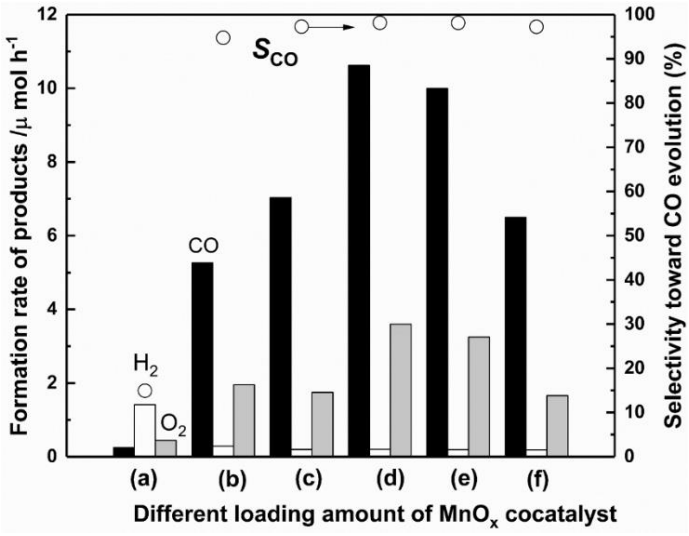


**Fig. 6** Formation rate of CO, $H_2$, and $O_2$ and $S_{CO}$(%) in the photocatalytic $CO_2$ reduction over the Ag -Mn/KTO samples loaded with different Mn loading amount, (a) bare KTO, (b) Ag(1.0)/KTO, (c) Ag(1.0)-Mn(0.09)/KTO, (d) Ag(1.0)-Mn(0.12)/KTO, (e) Ag(1.0)-Mn(0.14)/KTO, and (f) Ag(1.0)-Mn(0.17)/KTO.

**Table 1** Results of some blank tests for the photocatalytic $CO_2$ reduction with $H_2O$ under different conditions.

| Entry | conditions | Formation rate of products / μmol $h^{-1}$ | | | $S_{CO}$(%) [b] |
|---|---|---|---|---|---|
| | | CO | $H_2$ | $O_2$ | |
| 1 | standard conditions [a] | 10.07 | 0.20 | 4.39 | 98.2 |
| 2 | without irradiation | 0.00 | 0.00 | 0.00 | – |
| 3 | without photocatalyst | 0.81 | 0.91 | 0.17 | 47.1 |
| 4 | without $NaHCO_3$ | 0.99 | 0.75 | 0.00 | 56.9 |
| 5 | without $CO_2$ | 1.63 | 0.19 | 0.75 | 89.6 |

[a] Photocatalyst: the Ag(0.5)-Mn(0.13)/KTO sample, 0.3 g, reaction solution volume: 0.4 L, additive: 0.5 M $NaHCO_3$, $CO_2$ flow rate: 30 mL $min^{-1}$, light source: a 100 W high pressure Hg lamp. [b] Selectivity to CO, $S_{CO}$(%) = 100 × $R_{CO}$/ ($R_{CO}$ + $R_{H2}$), where $R_{CO}$ and $R_{H2}$ are the production rate of CO and $H_2$, respectively.

Further, the Ag(0.5)-Mn(0.13)/KTO sample realized an efficient $O_2$ evolution giving an almost ideal redaction/oxidation products ratio with high activity (Fig. 5). Fig. 7 shows a time course

of the reaction test with the Ag(0.5)-Mn(0.13)/KTO sample. The initial high production rate of CO would originate from the initial state of well-dispersed Ag cocatalyst particles. Although the $O_2$ evolution was insufficient in the induction period, which may be due to photoadsorption of $O_2$ on the photocatalyst surface or some competitive side reactions.[17-20] But it gradually increased with irradiation time and the stoichiometric production of CO and $O_2$ was continuously observed for 24 hours, revealing the equivalent consumption of photoexcited electrons and holes, i.e. $R(e^-/h^+)=1.1$.

The blank tests confirmed that the CO molecules predominantly originated from molecular $CO_2$ (Table 1). From these results, it was proved that the dual Ag-Mn cocatalyst could enhance the photocatalytic $CO_2$ reduction to CO.

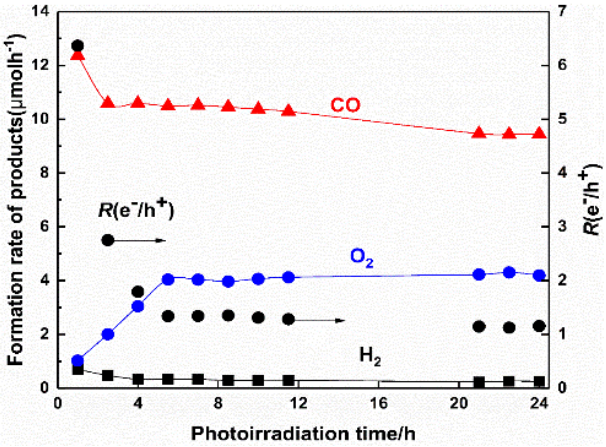


Fig. **7** Time course of the production rates of CO, $H_2$, and $O_2$, and $R(e^-/h^+)$ with the Ag(0.5)-Mn(0.13)/KTO sample in the photocatalytic $CO_2$ reduction test.

To clarify the effects and roles of the Ag-Mn dual cocatalyst, four samples, the bare KTO, Mn/KTO, Ag/KTO, and Ag-Mn/KTO samples, were examined as follows. As for the photocatalytic activity (Fig. 8), the Mn(0.15)/KTO sample exhibited similar or lower activity to produce both CO and $H_2$ compared with the bare KTO sample, demonstrating that the Mn cocatalyst cannot work solely. On the other hand, the formation rate of CO was strongly enhanced by loading the Ag cocatalyst and further improved with the Ag-Mn dual cocatalyst, confirming the obvious contribution of Ag cocatalyst and the further contribution of the dual cocatalyst for the $CO_2$ reduction. The CO evolution rate with the Ag(1.0)-Mn(0.12)/KTO sample was 42 times higher than those with both the bare KTO and Mn(0.15)/KTO samples, and almost 2 times higher than that with the Ag(1.0)/KTO sample.

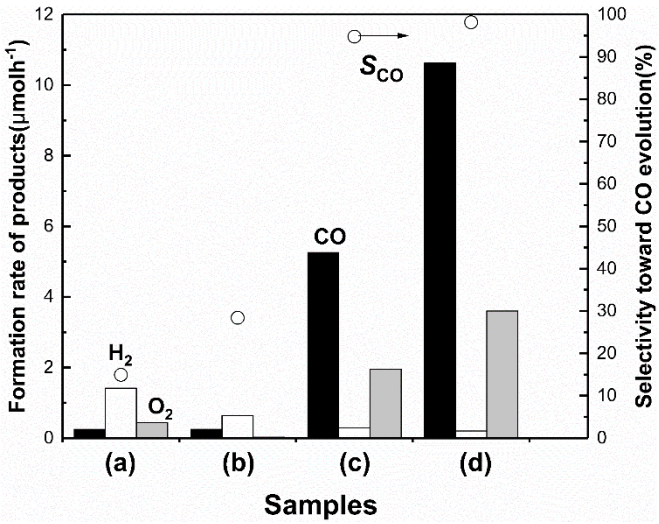


**Fig. 8** Formation rate of products in the photocatalytic $CO_2$ reduction with $H_2O$ over the various samples; (a) KTO, (b) Mn(0.15)/KTO, (c) Ag(1.0)/KTO, and (d) Ag(1.0)-Mn(0.12)/KTO. Photocatalyst: 0.3 g, reaction solution volume: 0.4 L, additive: 0.5 M $NaHCO_3$, $CO_2$ flow rate: 30 mL $min^{-1}$, light source: a 100 W high pressure Hg lamp.

The stability and durability of the sample were repeatedly confirmed for two time under the same condition (Fig. 7 and 9). The first run is shown in Fig. 7 and the second one (reused test) is presented below as Fig. 9. Also in the second run, almost the same formation rates of CO and $H_2$ were achieved, while there was a slight loss by a ca.10% $O_2$ evolution activity. This may due to the ca.15% loss of both Ag and $MnO_x$ cocatalyst, which was confirmed by the XRF.

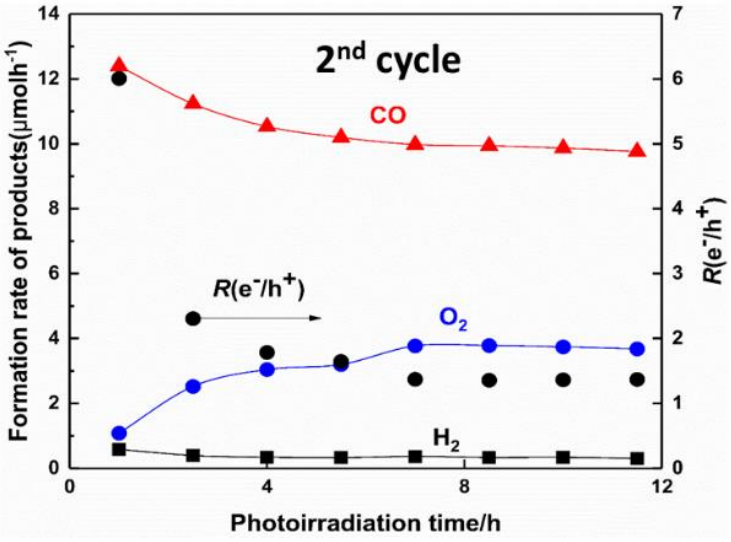


**Fig. 9** Time course of the production rates of CO, $H_2$, and $O_2$, and $R(e^-/h^+)$ with the Ag(0.5)-Mn(0.13)/KTO sample in the photocatalytic $CO_2$ reduction test as the second run after the first run shown in Fig. 7.

### 4-3.3 Diffuse reflectance UV visible spectra

DR UV-visible spectra of the four samples are shown in Fig. 10. In the spectrum of the Mn(0.15)/KTO sample (Fig. 10b), a broad and very week absorption band was observed, which is consistent with the fact that transition metal oxide such as manganese oxide usually shows grey color. Although the assignment of the small band observed at around 390 nm for the Ag(1.0)/KTO sample was not clarified yet (Fig. 10c), it may originate from the interaction of Ag species with the surface of KTO in the absence of the surface modification with Mn species. Other explanations are mentioned in the main text. Both the Ag(1.0)/KTO sample and the Ag(1.0)-Mn(0.09)/KTO sample (Fig. S8c and S8d) showed clearly a large broad band assignable to localized surface plasmon resonance (LSPR) of Ag nanoparticles at almost the same position around the 530 nm, suggesting that Ag nanoparticles were present on the KTO surface, and they would be almost similar state irrespective of the presence of the Mn species.

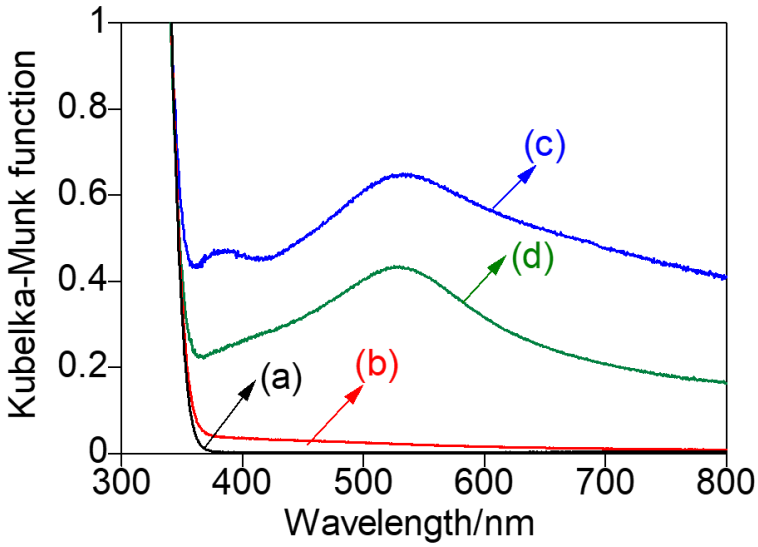


**Fig. 10** DR UV-vis spectra of the prepared samples, (a) bare KTO, (b) Mn(0.15)/KTO, (c) Ag(1.0)/KTO, and (d) Ag(1.0)-Mn(0.09)/KTO.

### 4-3.4 EXAFS spectra

The state and local structure of the dual cocatalyst were investigated by using X-ray absorption fine structure (XAFS). Fig. 11A shows Ag K-edge X-ray absorption near edge structures (XANES) of the prepared samples and two reference samples. The absorption edges (25519 eV) in the spectra of the photocatalyst samples were consistent with that of Ag foil (25519 eV) but different from that of $Ag_2O$ (25521 eV), and the spectral feature of XANES for the photocatalyst

samples is similar to that for Ag foil. The Fourier transforms of EXAFS spectra also showed almost the same feature for the photocatalyst samples and Ag foil (Fig. 12). These facts indicate that the Ag species loaded on the surface in both the Ag(1.0)/KTO and Ag(1.0)-Mn(0.09)/KTO samples were metallic. Thus, it was revealed that the coexistence of Mn species did not vary the metallic state of Ag cocatalyst.

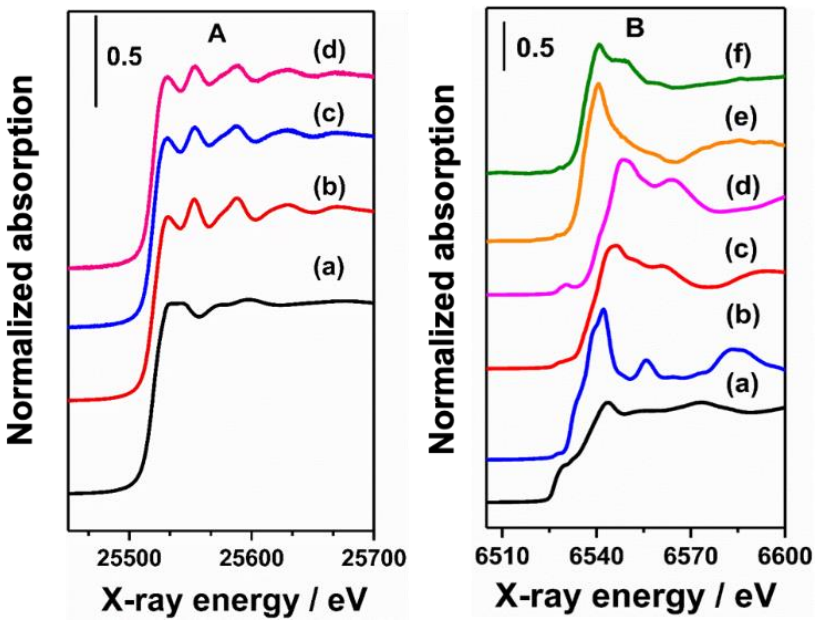


**Fig. 11** [A] Ag K-edge XANES of (a) $Ag_2O$, (b) Ag foil, (c) Ag(1.0)/KTO, and (d) Ag(1.0)-Mn(0.09)/KTO, and [B] Mn K-edge XANES of (a) Mn foil, (b) MnO, (c) $Mn_2O_3$, (d) $MnO_2$, (e) Mn(0.15)/KTO, and (f) Ag(1.0)-Mn(0.09)/KTO.

Fig. 12B shows Mn K-edge XANES of the prepared samples and some reference compounds such as Mn foil, MnO, $Mn_2O_3$, and $MnO_2$. The absorption edges for the prepared samples were not strictly consistent with those for the references, meaning that the Mn species deposited on the photocatalyst samples had different local structures from these typical manganese oxides. In detail, the edge position of the spectra for the Mn(0.15)/KTO and Ag(1.0)-Mn(0.09)/KTO samples (Fig. 12Be and 12Bf) were close to that for $Mn_2O_3$ (Fig.12Bc). However, the main peak position for the two samples was close to that for MnO (Fig. 12Bb) and the second peak at the post edge for the Ag(1.0)-Mn(0.09)/KTO sample was close to that for the main peak for $MnO_2$ (Fig. 12Bd). The Fourier transforms of EXAFS spectra of the photocatalyst samples also showed different features from those of the reference oxides (Fig. 13). Thus, the Mn species deposited on the KTO surface would have the unique local structures, suggesting

that they are not aggregated as a single phase of manganese oxide particles but well dispersed on the surface with unique local structure and valences.

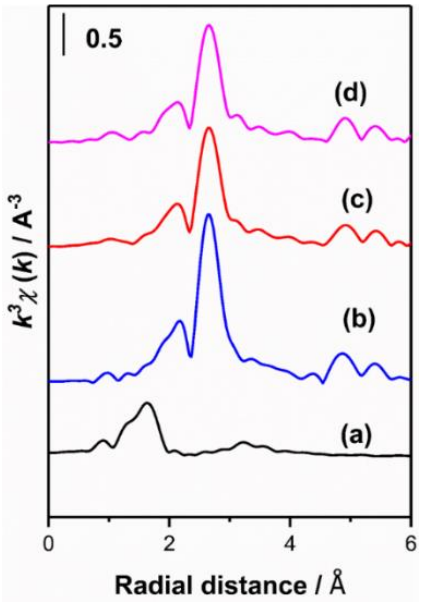


**Fig. 12** Fourier-transforms of Ag K-edge EXAFS spectra of (a) $Ag_2O$, (b) Ag foil, (c) the Ag(1.0)/KTO sample, and (d) the Ag(1.0)-Mn(0.09)/KTO sample.

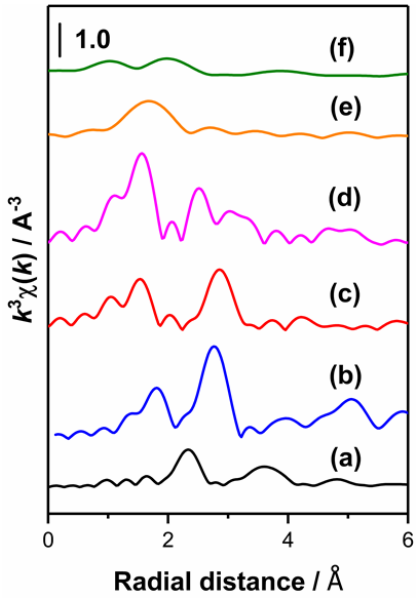


**Fig. 13** Fourier-transforms of Mn K-edge EXAFS spectra of (a) Mn foil, (b) MnO, (c) $Mn_2O_3$, (d) $MnO_2$, (e) the Mn(0.15)/KTO sample, and (f) the Ag(1.0)-Mn(0.09)/KTO sample.

## 4-3.5 SEM images, TEM images and TEM-EDS mappings

SEM images of the Ag(1.0)/KTO and Ag(1.0)-Mn(0.12)/KTO samples show the presence of additional particles on the KTO crystals, although it is difficult to distinguish the Ag and Mn species on the latter sample (Fig. 14).

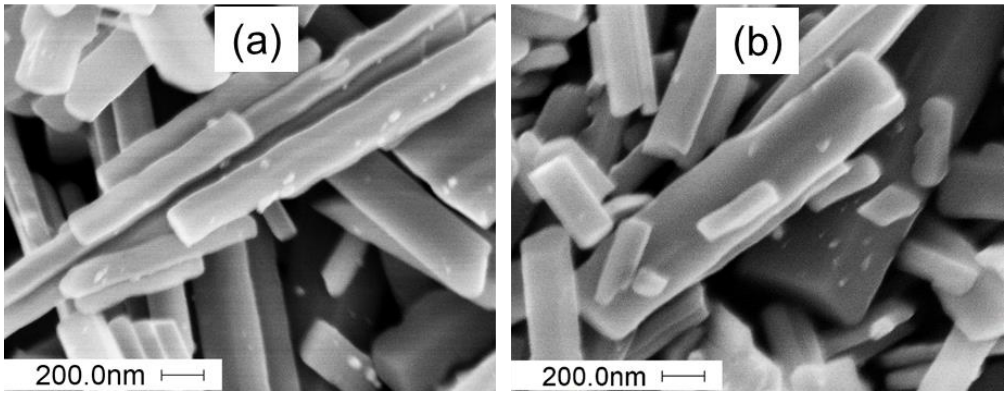


**Fig. 14** SEM images of (a) the Ag(1.0)/KTO sample, and (b) the Ag(1.0)-Mn(0.09)/KTO sample.

TEM images of the above four samples were shown in Fig. 15. Comparing the Mn(0.15)/KTO sample (Fig. 15b) with the bare KTO sample (Fig. 15a), no nanoparticles were found to deposit on the surface of the KTO sample, and no Mn species were detected by EDS mapping due to the low loading amount. However, as mentioned above, it was believed that the Mn species were well dispersed on the surface. For the Ag(1.0)/KTO sample (Fig. 15c and 15c') and the Ag(1.0)-Mn(0.12)/KTO sample (Fig. 15d and 15d'), Ag nanoparticles with the size less than 20 nm were observed.

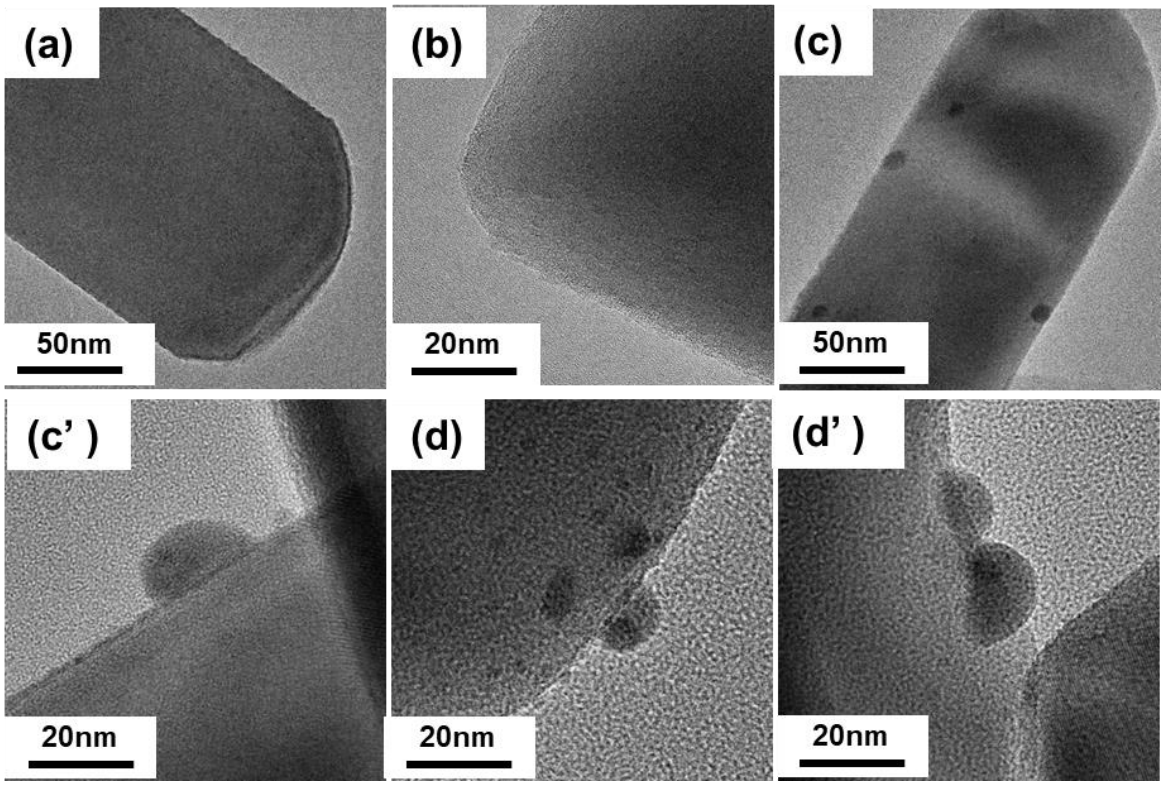


**Fig. 15** TEM images of the prepared samples, (a) bare KTO, (b) Mn(0.15)/KTO, (c,c') Ag(1.0)/KTO, and (d,d') Ag(1.0)-Mn(0.09)/KTO.

Fig. 16a and 16b show the TEM images of the prepared Ag(1.0)/KTO and Ag(1.0)-Mn(0.09)/KTO samples, respectively, where nanoparticles were observed on the surface of these two samples. As confirmed by EDS mapping shown at the right side of TEM images, the observed nanoparticles were assignable to Ag nanoparticles. Although some dots were found in each EDS mapping of Mn, they were assignable to not Mn species but the background noise because these dots are observed even in the area without any material, i.e., upper side in Fig. 16(a)

and upper middle area in Fig. 16(b). Therefore, the Mn species were not confirmed by the EDS mapping for both the Ag(1.0)/KTO and Ag(1.0)-Mn(0.09)/KTO samples, which may be due to the extremely low concentration as well as the amorphous and well dispersed structure.

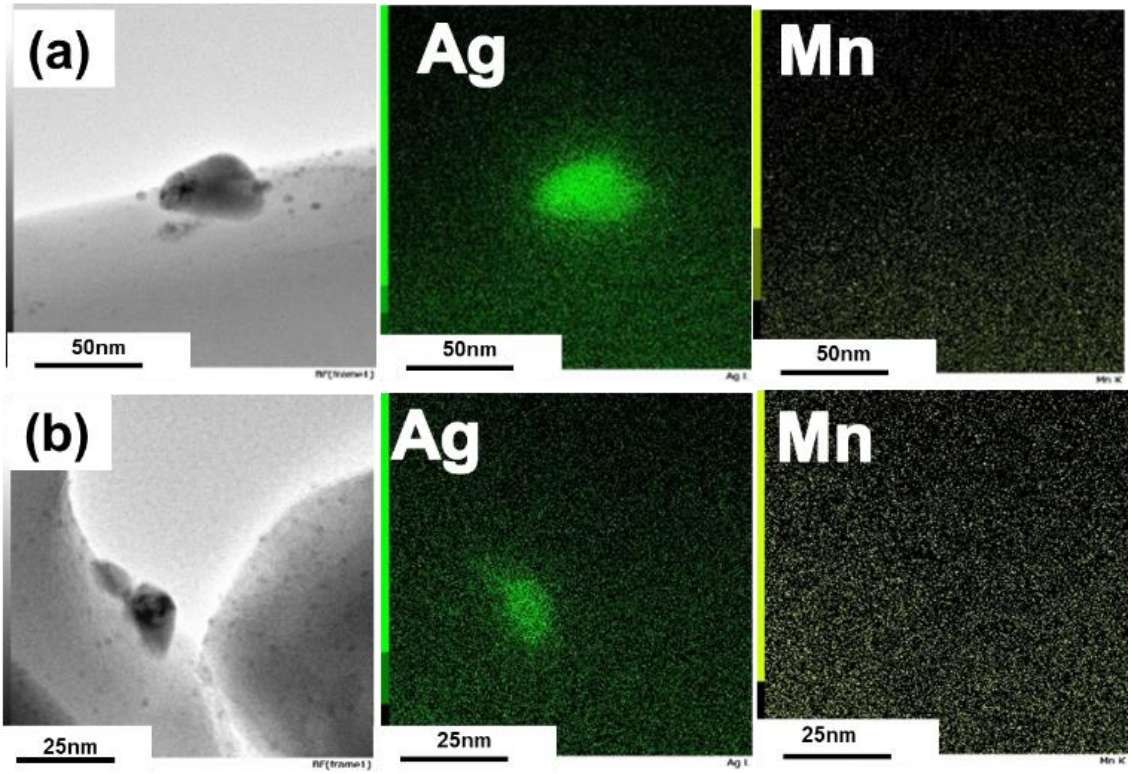


**Fig. 16** TEM images and EDS mappings of (a) the Ag(1.0)/KTO sample, and (b) the Ag(1.0)-Mn(0.09)/KTO sample.

## 4-3.6 Oxygen evolution

Finally, to clarify the role of the $MnO_x$ species, the photocatalytic tests of $O_2$ evolution from an aqueous solution of $Ag(NO_3)$ were conducted. Compared with the bare KTO and Ag(0.5)/KTO samples, the Mn(0.15)/KTO and Ag(0.5)-Mn(0.13)/KTO samples exhibited larger amount of $O_2$ evolutions with higher rates especially the Mn(0.15)/KTO sample in Fig. 17, even though the loading amount of the Mn species was very low. Here, it was clearly evidenced that the Mn species is beneficial to the $O_2$ evolution, which is supported by literatures.[42,43] In the present result, the photocatalyst with a Ag-Mn dual cocatalyst exhibited the highest activity for photocatalytic $CO_2$ reduction, while it showed lower activity than the photocatalyst with a single Mn cocatalyst for the oxygen evolution test, meaning that the addition of Ag nanoparticles seems to decrease the oxidative activity. A part of Ag species loaded on the

oxidative sites may react with holes competitively or change the state of the $MnO_x$ species.

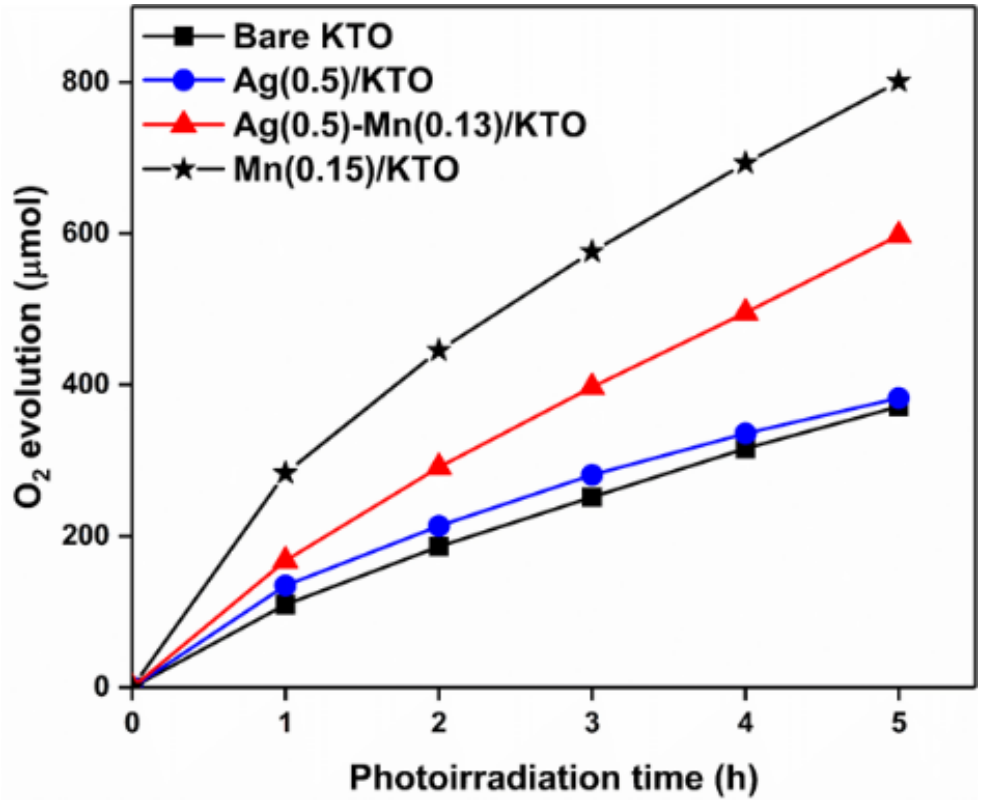


**Fig. 17** Time course of $O_2$ evolution over the prepared photocatalysts. Sacrificial reagents: 0.5 M of $AgNO_3$ solution. Light source: a 100 W high pressure Hg lamp.

## 4-4 Conclusion

In conclusion, it was found that the KTO sample loaded with both Ag metal and manganese oxide species such as Ag(0.5)-Mn(0.13)/KTO samples exhibited the highest activity (10 μmol $h^{-1}$) and the highest selectivity ($S_{CO}$=98%) with the stoichiometric production ratio of the oxidative and reductive products, which showed almost 2 times higher CO production rate than the Ag(1.0)/KTO sample. The $MnO_x$ cocatalyst can enhance the oxidative reaction, i.e., the $O_2$ evolution (Eq. 1), which leads to the improvement of CO evolution (Eq. 2) with synergistic effect of Ag cocatalyst. Here, the dual cocatalyst, i.e., the combination of Ag and $MnO_x$ species, simultaneously contribute to the reductive and oxidative reactions, respectively, realized the photocatalytic $CO_2$ reduction to CO with a higher reaction rate and a higher selectivity such as 98%.

$$H_2O + 2h^+ \rightarrow ½O_2 + 2H^+ \quad (1)$$

$$CO_2 + 2H^+ + 2e^- \rightarrow CO + H_2O \quad (2)$$

## References


1 M. Halmann, *Nature*, 1978, **275**, 115.

2 Ishitani, C. Inoue, Y. Suzuki, T. Ibusuki, O. Ishitani, C. Inoue, Y. Suzuki and T. Ibusuki, *J.Photoch. Photobio. A*, 1993, **72**, 269.

3 S. Sato, T. Arai, T. Morikawa, K. Uemura, T.M. Suzuki, H. Tanaka and T. Kajino, *J. Am. Chem. Soc.*, 2011, **133**, 15240

4 S.N. Habisreutinger, L. Schmidt-Mende and J.K. Stolarczyk, *Angew. Chem., Int. Ed.*, 2013, **52**, 7372.

5 K. Iizuka, T. Wato, Y. Miseki, K. Saito and A. Kudo, *J. Am. Chem. Soc.*, 2011, **133**, 20863.

6 M. Yamamoto, T. Yoshida, N. Yamamoto, H. Yoshida and S. Yagi, *E-Journal Surf. Sci. Nanotechnol.*, 2014, **12**, 299.

7 N. Yamamoto, T. Yoshida, S. Yagi, Z. Like, T. Mizutani, S. Ogawa, H. Nameki and H. Yoshida, *E-Journal Surf. Sci. Nanotechnol.*, 2014, **12**, 263.

8 H. Tatsumi, K. Teramura, Z. Huang, Z. Wang, H. Asakura, S. Hosokawa and T. Tanaka. *Langmuir*, 2017, **33**, 13929.

9 Z. Wang, K. Teramura, S. Hosokawa and T. Tanaka, *Appl. Catal. B Environ.*, 2015, **163**, 241.

10 T. Takayama, K. Tanabe, K. Saito, A. Iwase and A. Kudo, *Phys. Chem. Chem. Phys.*, 2014, **16**, 24417.

11 H. Yoshida, L. Zhang, M. Sato, T. Morikawa, T. Kajino, T. Sekito, S. Matsumoto and H. Hirata, *Catal. Today*, 2015, **251**, 132.

12 H. Yoshida, M. Sato, N. Fukuo, L. Zhang, T. Yoshida, Y. Yamamoto, T. Morikawa, T. Kajino, M. Sakano, T. Sekito, S. Matsumoto and H. Hirata, *Catal. Taday*, 2018, **303**, 296.

13 Z. Wang, K. Teramura, Z. Huang, S. Hosokawa, Y. Sakata and T. Tanaka, *Catal. Sci. Technol.*, 2016, **6**, 1025.

14 Z. Huang, K. Teramura, H. Asakura, S. Hosokawa and T. Tanaka, *J. Mater. Chem. A*, 2017, **5**, 19351.

15 Anzai, N. Fukuo, A. Yamamoto and H. Yoshida, *Catal. Commun.*, 2017, **100**, 134.

16 R. Pang, K. Teramura, H. Asakura, S. Hosokawa and T. Tanaka, *Appl. Catal. B Environ.,* 2017, **218**, 770.

17 X. Zhu, A. Anzai, A. Yamamoto and H. Yoshida, *Appl. Catal. B Environ.*, 2019, **243**, 47.

18 R.I. Bickley, F.S. Stone, *J. Catal.*, 1973, **31**, 389.

19 T. Berger, M. Sterrer, O. Diwald and E. Knozinger, *ChemPhysChem*, 2005, **6** ,2104.

20 Y. F. Li, Z. P. Liu, L. Liu and W. Gao, J. Am. Chem. Soc., 2010, 132, 13008.

21 R. Abe, J. Photochem. Photobiol. C Photochem. Rev., 2010, 11, 179.

22 Vojvodic and J.K. Norskov, *Science*, 2011, **334**, 1355.

23 Kudo and Y. Miseki, *Chem. Soc. Rev.*, 2009, **38**, 253.

24 J. Yang, D. Wang, H. Han and C. Li, *Acc. Chem. Res.*, 2013, **46**, 1900.

25 Z. Chang, S. Huo, W. Zhang, J. Fang and H. Wang, *J. Phys. Chem. C*, 2017, **121**, 11368.

26 Q. Zhai, S. Xie, W. Fan, Q. Zhang, Y. Wang, W. Deng and Y. Wang, *Angew. Chem.*, Int. Ed., 2013, **52**, 5776.

27 R. Pang, K. Teramura, H. Tatsumi, H. Asakura, S. Hosokawa and T. Tanaka, *Chem. Commun.*, 2018, **54**, 1053.

28 K. Maeda, A. Xiong, T. Yoshinaga, T. Ikeda, N. Sakamoto, T. Hisatomi, M. Takashima, D. Lu, M. Kanehara, T. Setoyama, T. Teranishi and K. Domen, *Angew. Chem., Int. Ed.*, 2010, **49**, 4096.

29 J. Zhu, S. Pang, T. Dittrich, Y. Gao, W. Nie, J. Cui, R. Chen, H. An, F. Fan and C. Li, *Nano Lett.*, 2017, 17, 6735.

30 Z. Jiang, D. Ding, L. Wang, Y. Zhang and L. Zan, *Catal. Sci. Technol.*, 2017, **7**, 3065.

31 L. Wang, Q. Chen, J. Hu, H. Li, Y. F. Hu and L. M. Peng, *Chem. Phys. Lett.*, 2005, **406**, 95.

32 Q. Zhang, Y. Guo, K. Guo, T. Zhai and H. Li, *Chem. Commun.*, 2006, **52**, 6229.

33 K.Byrappa, S.Gali, B.M.R. Wanklyn, A.B.Kulkarni, S.K. Patil and G.Narendranath, *J. Mater. Sci. Lett.*, 1990, **9**, 898.

34 K. Shimura, H. Kawai, T. Yoshida and H. Yoshida, *ACS Catal.*, 2012, **2**, 2126.

35 H. Yoshida, M. Takeuchi, M. Sato, L. Zhang and T. Teshima, *Catal. Today*, 2014, **232**, 158.

36 P. Ponce-peña, M. A. González-lozano, M. A. Escobedo-bretado and P. De Lira-gómez, *Ceram. Int.*, 2015, **41**, 10051.

37 L.F. Garay-Rodríguez, L.M.T. Martínez and E. Moctezuma, *J. Energy Chem.*, 2019, **37**, 18.

38 E. A. Davis and N. F. Mott, *Philos. Mag.*, 1970, **22**, 903.

39 Y. Ma, R. Chong, F. Zhang, Q. Xu, S. Shen, H. Han and C Li. *Phys.Chem.Chem.Phys.*,2014, **16**, 17734.

40 R. Li, F. Zhang, D. Wang, J. Yang, M. Li, J. Zhu, X. Zhou, H. Han and C. Li, *Nat. Commun.*, 2013, **4**, 1432.

41 J. Yang, D. Wang, H. Han and C. Li, *Acc. Chem. Res.*, 2013, **46**, 1900.

42 R. Li, H. Han, F. Zhang, D Wang and Can Li, *Energy Environ. Sci.*, 2014, **7**, 1369.

43 S. Xie, Y. Wang, Q. Zhang, W. Deng and Y. Wang, *Chem. Commun.*, 2015, **51**, 3430.

# Chapter 5 Facet-selective deposition of a bifunctional silver-manganese cocatalyst on potassium hexatitanate photocatalyst for selective photocatalytic reduction of carbon dioxide by water


## Abstract

In our previous study, a silver-manganese oxide dual cocatalyst deposited on a potassium hexatitanate photocatalyst (Ag-$MnO_x$/$K_2Ti_6O_{13}$) was found to significantly promote photocatalytic $CO_2$ reduction to CO with very high selectivity by using $H_2O$ as an electron donor, owing to the properties of Ag and $MnO_x$ species for promoting CO and $O_2$ formation, respectively. In the present study, the different deposition methods for loading the dual cocatalyst were investigated to figure out the functional states of the Ag and $MnO_x$ species. A core-shell structure of the dual cocatalyst gave less activity towards $CO_2$ reduction. On the other hand, when the Ag and $MnO_x$ species were loaded by a simultaneous photodeposition method, they were separately deposited on the long and short facets of the rod-like $K_2Ti_6O_{13}$ crystal, respectively, and these species functioned as efficient promoters for CO formation from $CO_2$ and $O_2$ evolution from $H_2O$, respectively.


## 5-1 Introduction

The development of technologies to convert carbon dioxide ($CO_2$), one of the greenhouse gases, to useful products is critically required to solve global warming problem. Especially, heterogeneous photocatalysis has attracted much attention since it can transform $CO_2$ into valuable compounds, such as CO, $CH_4$, and $CH_3OH$, by using solar energy.[1–6] Among these possible reduced products from $CO_2$, CO would be considered as the most useful product since it is a valuable chemical intermediate in industry for further chemical syntheses and easily separable from the aqueous reaction media to the gas phase.[7] In the typical photocatalytic $CO_2$ reduction to produce CO by using water as an electron donor, two reactions competitively occurred, i.e., photocatalytic reduction of $CO_2$ to form CO and photocatalytic water splitting into $H_2$ and $O_2$ in aqueous solution, where the reductive products are CO and $H_2$ and the oxidative product is $O_2$ in common, [7] i.e., photocatalytic reduction of $CO_2$ to form CO (Eq. 1) and photocatalytic water splitting into $H_2$ and $O_2$ (Eq. 2). But, the redox potential of $H^+/H_2$ is

more positive than that of $CO_2$/CO, so the reduction of $CO_2$ to CO is thermodynamically harder than that of protons ($H^+$) to $H_2$. Thus, it seems basically difficult to selectively reduce only carbon dioxide in an aqueous solution in principle.

$$CO_2 + 2H^+ + 2e^- \rightarrow CO + H_2O \quad (1)$$

$$H_2O + 2h^+ \rightarrow ½O_2 + 2H^+ \quad (2)$$

For over a decade, deposited Ag nanoparticles was found to function as the active cocatalyst for $CO_2$ reduction to form CO.[7] and various semiconductors have been studied as photocatalysts for $CO_2$ reduction to CO, such as $TiO_2$,[5,8–10] $BaLa_4Ti_4O_{15}$,[7] $La_2Ti_2O_7$,[11] $Ga_2O_3$,[12–15] $SrNb_2O_6$,[16] $KCaSrTa_5O_{15}$,[17] $CaTiO_3$,[18,19] $Na_2Ti_6O_{13}$,[20,21] $Ba_2Li_{2/3}Ti_{16/3}O_{13}$,[22] and so on. However, the practical applications of these photocatalysts for $CO_2$ reduction are still limited because of the low $CO_2$ conversion efficiency due to fast electrons and holes recombination, low light utilization, and so on.

For enhancing the photocatalytic $CO_2$ reduction performance, diverse strategies such as bandgap tuning, doping, morphology controlling, surface modification, and cocatalyst loading have been explored.[7,12,14,23–29] Deposition of cocatalysts could significantly improve the performance of the photocatalyst for $CO_2$ reduction, where the co-catalysts can function as trapping sites for the electrons or providing active sites, thus promoting the charge separation and altering the selectivity of the products. And the deposition of dual cocatalysts (reduction cocatalyst and oxidation cocatalyst) can quickly trap the photoexcited electrons and holes to improve the charge-separation and charge-utilization efficiencies. And some dual cocatalysts were reported to enhance the photocatalytic activity in $H_2O$ splitting or $CO_2$ reduction.[26,30–35] Many reported papers had proposed the possible reasons for the nonstoichiometric formation of $O_2$, such as high overpotential required for $O_2$ evolution and some side reactions,[21,36] and it has also been reported that some metal oxides (such as $IrO_2$, $RuO_2$, $CoO_x$, $MnO_x$, etc.) can act as the water oxidation cocatalyst for water splitting,[37] but they have rarely applied for $CO_2$ reduction so far. Recently, some cocatalysts with core-shell structures particles such as Ag/Cu,[38] Pt/$Cu_2O$,[39] and Ag/$CrO_x$[26] ($CO_2$ reduction) and Cr/Rh[40] (water splitting), and two separated metal/oxide particles, such as Pt/$MnO_x$[41] (water splitting) have been proved to enhance the activity by taking advantage of the synergistic function of dual active sites for both reductive and oxidative reactions simultaneously, or the modification of the cocatalyst

surface suppressed the backward reaction.[42]

Crystal of photocatalysts covered with several facets has been noticed to provide reductive and oxidative reaction field separately, which was firstly reported by Ohno et al. using facet-selective photodeposition of Pt and $PbO_2$ on rutile $TiO_2$.[43] Li et al. have reported this phenomenon on several photocatalysts[41,44,45] such as a $BiVO_4$ photocatalyst and explained that the difference of energy levels of these facets enables the facet selective photocatalysis.[41] Recently, a combination of Ag and $MnO_x$ was examined as a dual cocatalyst deposited on each facet of $TiO_2$ crystal photocatalyst to promote CO formation from a mixture of $NaHCO_3$ and $H_2SO_4$ in an aqueous solution although $O_2$ evolution was not clearly mentioned.[46] In our previous study, a silver-manganese oxide dual cocatalyst deposited on potassium hexatitanate ($K_2Ti_6O_{13}$) crystal photocatalyst significantly enhances photocatalytic $CO_2$ reduction to produce CO with extremely high selectivity by using $H_2O$ as an electron donor, owing to the properties of Ag and $MnO_x$ species for promoting CO and $O_2$ formation, respectively.[47] However, the structures and properties of these species in the dual cocatalyst and relation to the facets on the crystal have been clarified yet. In the present study, we investigate and discussed these points by testing different methods for the deposition of dual cocatalyst.

## 5-2 Experimental

### 5-2.1 Photocatalyst preparation

Potassium titanate ($K_2Ti_6O_{13}$, KTO) sample was prepared by a flux method.[21] The precursors, $K_2CO_3$ (Kishida) and $TiO_2$ (rutile, Kojundo), and a flux reagent KCl (Kishida) were mixed, where the molar ratio of $K_2CO_3$ to $TiO_2$ was 1:6, and 70% of flux was used, which was calculated as; 70 [mol%] = 100 × (amount of KCl [mol])/(amount of KTO [mol]+ amount of KCl [mol]). The mixture was heated at 1273 K for 10 h in the furnace. The obtained powder was thoroughly washed with hot water and filtrated, then dried at 323 K for 24 hours.

For a Ag(PD)/KTO sample, a Ag cocatalyst was loaded on the surface by a photodeposition method (PD), where 1 g of the prepared KTO sample was dispersed ion-exchanged water containing a required amount of $Ag(NO_3)$ as a cocatalyst precursor, and the suspension was irradiated under a 100 W high-pressure Hg lamp with a bubbling flow of argon for 2 hours, followed by filtration and drying at 353K in the oven. Ag and $MnO_x$ dual cocatalysts were loaded on the surface by four different methods including a facile simultaneously PD method,

impregnation (IMP) method, and their combination. As for a Ag(PD)-$MnO_x$(PD)/KTO sample prepared by a simultaneous PD method, ion-exchanged water containing required amounts of cocatalyst precursors, Ag($NO_3$) and Mn($NO_3$)$_2$, were used and other procedure was the same as that for the PD method. As for a Ag(IMP)-$MnO_x$(IMP)/KTO sample prepared by a simultaneous IMP method, 1 g of the prepared KTO sample was suspended in 150 mL of ion exchange water with the desired amounts of Ag($NO_3$) and Mn($NO_3$)$_2$, followed by evaporation at 358 K to remove water, drying for 24 h at 373 K, and calcination at 723 K for 2 h in air. For a $MnO_x$(IMP)/Ag(PD)/KTO sample, the Ag cocatalyst was first loaded by the PD method, followed by loading $MnO_x$ species in the IMP method. And for a Ag(PD)/$MnO_x$(IMP)/KTO sample, the $MnO_x$ species was loaded on the KTO sample by the IMP method, followed by loading Ag species in the PD method. To show the loading amount of the components, the samples are referred to as e.g., Ag(PD,*x*)-$MnO_x$(PD,*y*)/KTO, where *x* and *y* mean the actual loading amount of Ag and Mn (wt %) determined by X-ray florescence analysis (XRF) as mentioned below.

### 5-2.2 Characterization

The loading amount of cocatalyst on the samples was evaluated by X-ray florescence analysis with an EDX-8000 (Shimadzu) using each experimentally obtained calibration curve, where the samples loaded by the impregnation method were used as a reference. The crystal structure of the samples was determined by powder X-ray diffraction with a Lab X XRD-6000 (Shimazu). Morphologies of the samples were observed by scanning electron microscopy (SEM) with a JSM-890 (JEOL). Images of transmission electron microscopy (TEM) and scanning transmission electron microscopy (STEM) were taken by a JEOL JEM-2100F at 200 kV in the Joint Research Centre of Kindai University. The samples were dispersed in methanol, dropped onto a carbon-coated copper grid, and dried at ambient temperature for 5 h. The diffuse reflectance UV-Vis spectrum was recorded by a V-670 (JASCO). Ag and Mn K-edge X-ray absorption fine structures (XAFS) were recorded at NW-10C and BL-12C of the Photon Factory (KEK, Tsukuba, Japan), respectively. Most of the samples including the references were measured in a transmission mode, while the Mn K-edge XAFS spectra of the prepared samples were measured in a fluorescence mode due to the small amount of Mn species.

## 2.3 Photocatalytic reaction

The photocatalytic activity test of $CO_2$ reduction with water was carried out using a bubbling flow system with an inner-irradiation photochemical reaction vessel (Fig. S1).[19] The

photocatalyst powder sample (0.3 g) was dispersed in ion-exchanged water (400 mL) containing 0.5 M $NaHCO_3$ (pH=8), and suspended by magnetically stirring. Then, $CO_2$ was bubbled into the solution at a flow rate of 30 mL $min^{-1}$ without irradiation for 1.5 hours to exclude the air from the reactor. The photocatalytic reaction was conducted under photoirradiation from a 100 W high-pressure mercury lamp located in the center of the reactor. The light intensity was measured to be 22 mW $cm^{-2}$ at a detecting wavelength of 254±10 nm. The reaction temperature was set at 290 K with cooling water. The amount of the products ($H_2$, $O_2$, and CO) in the outlet gas from the reactor were determined by using an on-line gas chromatograph (Shimadzu, GC-8A, TCD, a Shincarbon ST column, argon carrier). Since no other reductive products than CO and $H_2$ were observed, the selectivity toward CO evolution (%), and the ratio of the consumed electron and hole ($e^-/h^+$), were calculated according to Equations (3) and (4), respectively,[16,48] where the production rate of CO, $H_2$, and $O_2$ are referred to as $R_{CO}$, $R_{H2}$, and $R_{O2}$, respectively.

$$S_{CO}\ (\%) = 100 \times R_{CO} / (R_{CO} + R_{H2}) \quad (3)$$

$$\text{Consumed } e^-/h^+ = (2R_{CO} + 2R_{H2})/4R_{O2} \quad (4)$$

# 5-3 Results and Discussions

## 5-3.1 Prepared photocatalysts

Fig. 1 shows XRD patterns of the obtained KTO sample and that of a $K_2Ti_6O_{13}$ reference from a database (ICSD#25712). The XRD pattern of the prepared KTO sample was consistent with that of the reference. It gives no diffraction lines corresponding to other impurity phases, confirming that the prepared potassium hexatitanate was correctly fabricated by the flux method. Fig. 2 shows that the KTO sample consisted of rod-like crystals with similar morphology and size. As was shown in Fig. 3a, the bandgap of the bare KTO was estimated to be 3.56 eV by a diffuse reflectance (DR) UV-visible spectrum and the Davis–Mott equation.[49]
The actual loaded amounts of cocatalysts determined by XRF were shown in Table 1. The desired amount of cocatalyst was successfully loaded over the prepared sample, except for the Ag(PD,1.0)-$MnO_x$(PD,0.09)/KTO sample, since the $MnO_x$ cocatalyst is difficult to loaded via a PD method.

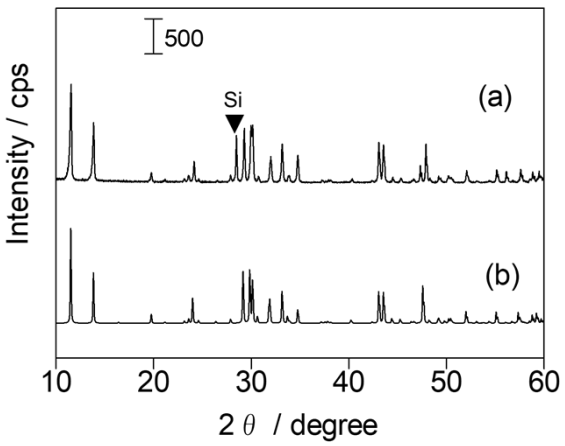


**Fig. 1** XRD patterns of (a) the prepared KTO sample and (b) a reference data #25712 from ICSD database for $K_2Ti_6O_{13}$. A closed triangle indicates a diffraction from silicon powder mixed with the KTO sample to calibrate the angle.

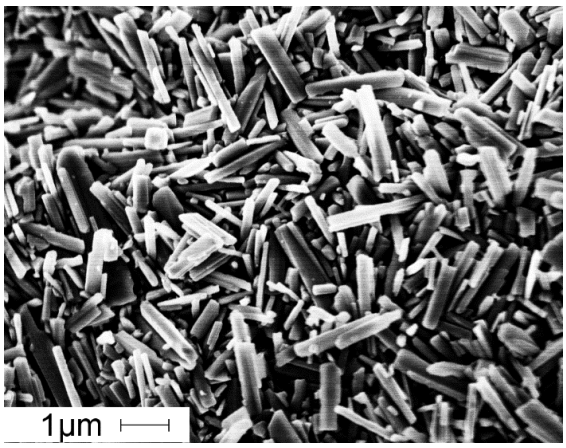


**Fig. 2** SEM image of the prepared KTO sample.

**Table 1. Actual loaded amount of cocatalysts over the prepared samples.**

| Prepared samples | Ag loaded amount (wt%) | $MnO_x$ loaded amount (wt%) |
|---|---|---|
| Ag/KTO | 1.0 | – |
| Ag(PD)-Mn(PD)/KTO | 1.0 | 0.09 |
| Ag(IMP)-$MnO_x$(IMP)/KTO | 1.0 | 1.0 |
| $MnO_x$(IMP)/Ag(PD)/KTO | 1.0 | 1.0 |
| Ag(PD)/$MnO_x$(IMP)/KTO | 1.0 | 1.0 |
| Ag(PD($CH_3OH$))/KTO | 5.0 | – |
| $MnO_x$(PD($NaIO_3$))/KTO | – | 5.0 |
| $MnO_x$(PD($NaIO_3$))/Ag(PD($CH_3OH$))/KTO | 5.0 | 5.0 |

The Ag(PD,1.0)/KTO and Ag(PD,1.0)-$MnO_x$(PD,0.09)/KTO samples (Fig. 3b, c) showed clearly a large broad band at almost the same position around the 530 nm assignable to localized

surface plasmon resonance (LSPR) of Ag nanoparticles, suggesting that Ag nanoparticles were present on the KTO surface.[50–52] While for the $MnO_x$(IMP,1.0)-Ag(IMP,1.0)/KTO and $MnO_x$(IMP,1.0)/Ag(PD,1.0)/KTO samples (Fig. 3d, e), a broad absorption band was observed instead of the LSPR adsorption band, meaning that the Ag species on these samples have different from metallic nanoparticles in their structure and properties. These samples showed grey color, which would originate from manganese oxide ($MnO_x$) species. And the Ag(PD,1.0)/$MnO_x$(IMP,1.0)/KTO showed the small amount of LSPR adsorption band assignable to Ag nanoparticles over the broad band due to the MnOx species (Fig. 3f).

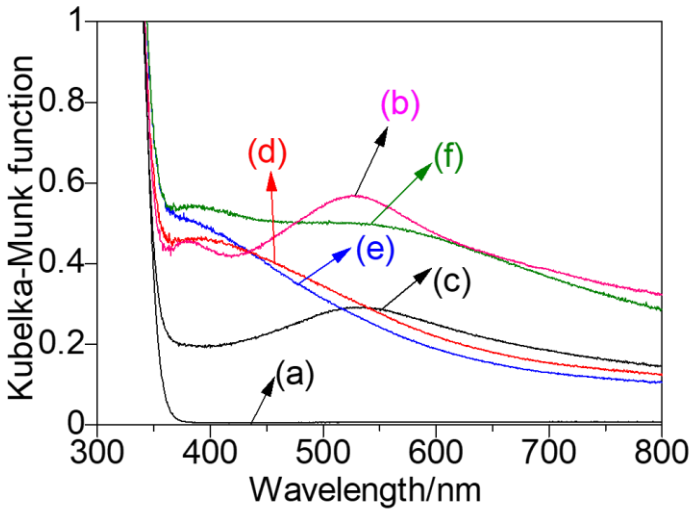


**Fig. 3** DR UV-vis spectra of the samples prepared with different methods, (a) bare KTO, (b) Ag/KTO, (c) Ag(PD,1.0)-$MnO_x$(PD,0.09)/KTO, (d) Ag(IMP,1.0)-$MnO_x$(IMP,1.0)/KTO, (e) $MnO_x$(IMP,1.0)/Ag(PD,1.0)/KTO, and (f) Ag(PD,1.0)/$MnO_x$(IMP,1.0)/KTO.

## 5-3.2 Photocatalytic reduction of $CO_2$

As was shown in Fig. 4, the $CO_2$ reduction tests were conducted for the prepared samples. The bare KTO sample without any cocatalyst mainly produced hydrogen and oxygen through water splitting (Fig. 4a), where CO was also produced although the formation rate was very low. Compared with the bare KTO sample, the production rate of CO was much more enhanced by loading the Ag cocatalyst (Fig. 4b). This means that the Ag nanoparticles functioned as the active sites for $CO_2$ reduction to form CO. The selectivity toward CO evolution in the reduction products ($S_{CO}$) was quite high such as 96.5%. When the dual cocatalysts consisting of Ag and $MnO_x$ species were loaded, the performance of these four samples much varied with the

methods. The Ag(PD,1.0)-$MnO_x$(PD,0.09)/KTO sample prepared by the simultaneous PD method (Fig. 4c) gave quite high CO evolution (7.2 μmol $h^{-1}$) with a high selectivity toward CO evolution (96%). But the Ag(IMP,1.0)-$MnO_x$(IMP,1.0)/KTO and $MnO_x$(IMP,1.0)/Ag(PD,1.0)/KTO samples exhibited very low activity for the $CO_2$ reduction (Fig. 4d and 4e). The former sample was prepared by the simultaneous IMP method and the latter was prepared by two-step method, first the PD method and then the IMP method, i.e., these samples were prepared by calcination at the last step of the preparation procedure and they exhibited no LSPR bands due to Ag nanoparticles (Fig. 5d and 5e), suggesting that the Ag species would be of oxidized state and less active for $CO_2$ reduction with a lower selectivity to CO formation. The Ag(PD,1.0)/MnOx(IMP,1.0)/KTO sample showed a high photocatalytic activity for $CO_2$ reduction with a high selectivity (Fig. 4f). On this sample, the Ag species was loaded by the PD method at the final step in the preparation procedure. The sample exhibited the LSPR band due to Ag nanoparticles overlapping to the broad band of $MnO_x$ species. The results mentioned above suggest that the metallic Ag nanoparticles are necessary for the selective formation of CO and the simultaneous PD method is excellent for this purpose. However, since the loading amount of $MnO_x$ species was low (0.09 mol%) only for the sample prepared by the simultaneous PD method, the effect of the loading amount of Mn species were examined as follows.

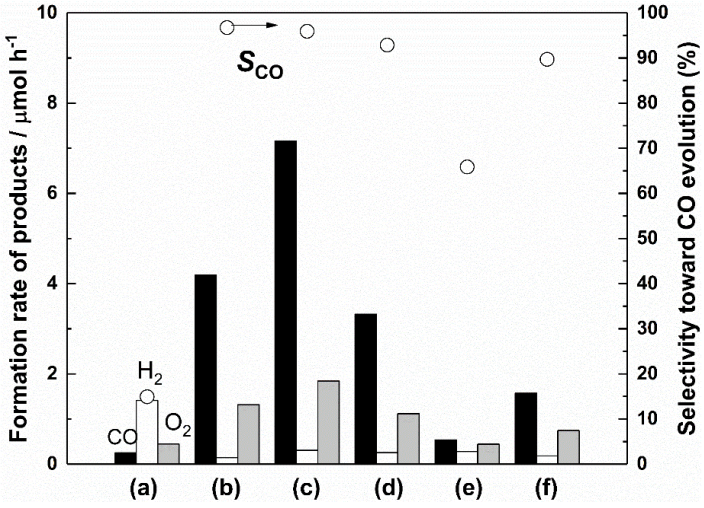


**Fig. 4** Photocatalytic reduction of $CO_2$ over the prepared samples loaded with different methods, (a) bare KTO, (b) Ag/KTO, (c) $MnO_x$(PD, 0.09)-Ag(PD, 1.0)/KTO, (d) $MnO_x$(IMP, 1.0)/Ag(PD, 1.0)/KTO, (e) Ag(PD, 1.0)/$MnO_x$(IMP, 1.0)/KTO, and (f) $MnO_x$(IMP, 1.0)-Ag(IMP,1.0)/KTO.

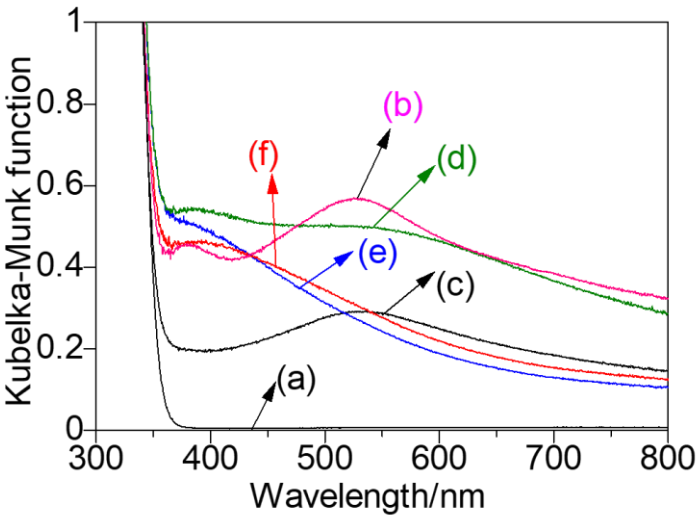


**Fig. 5** DR UV-vis spectra of the prepared samples loaded with different methods, (a) bare KTO, (b) Ag/KTO, (c) $MnO_x$(PD, 0.09)-Ag(PD, 1.0)/KTO, (d) $MnO_x$(IMP, 1.0)/Ag(PD, 1.0)/KTO, (e) Ag(PD,1.0)/$MnO_x$(IMP, 1.0)/KTO, and (f) $MnO_x$(IMP, 1.0)-Ag(IMP, 1.0)/KTO.

In a photodeposition method, the cocatalyst species can be loaded when the photocatalyst reduces or oxidizes the cocatalyst precursor in the solution. Although it is useful to deposit precious metal cocatalyst such as Ag metal nanoparticles, the photodeposition of transition metal oxide species may be relatively difficult compared with precious metals. Actually, the amount of the $MnO_x$ cocatalyst of the Ag(PD,1.0)-$MnO_x$(PD,0.09)/KTO sample was lower than the Ag species, where the irradiation time (2 h) would be enough for the deposition of Ag species but not for the $MnO_x$ species. In a photodeposition method, $Mn^{2+}$ cation is oxidized and deposited to form the $MnO_x$ species,[46] suggesting that the rate of water oxidation was higher than that of $Mn^{2+}$ oxidation in the aqueous solution. On the other hand, the loading amount of the $MnO_x$ species can be exactly controlled by the IMP method. So that, to confirm the loading amount effect of the $MnO_x$ species on the photocatalytic activity, a series of experiments were conducted with the Ag(PD,1.0)/$MnO_x$(IMP,*x*)/KTO samples with different loading amounts of $MnO_x$ cocatalyst. This preparation method can provide both metallic Ag nanoparticles and $MnO_x$ species, which is supported by the DR UV-visible spectra (Fig. 6). The photocatalytic reaction tests (Fig. 7) revealed that, the activity was decreased with the decrease of $MnO_x$ loading amount from 0.1 to 1.0 mol%, and the activity of

Ag(PD,1.0)/$MnO_x$(IMP,0.1)/KTO sample was lower than the Ag(PD,1.0)-$MnO_x$(PD,0.09)/KTO sample (Fig. S6c and S6d). This indicates that the key factor to determine the photocatalytic activity between these two groups was not the amount of $MnO_x$ species but the preparation method and the resulting structure, property, and location, as discussed later.

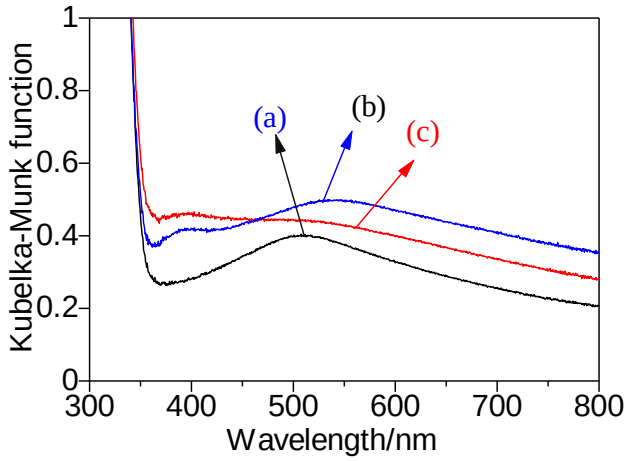


**Fig. 6** DR UV-vis spectra of the prepared samples with different loading amount of $MnO_x$ species, (a) Ag(PD,1.0)/$MnO_x$(IMP, 0.1)/KTO, (b) Ag(PD,1.0)/$MnO_x$(IMP, 0.3)/KTO, and (c) Ag(PD,1.0)/$MnO_x$ (IMP,0.5)/KTO.

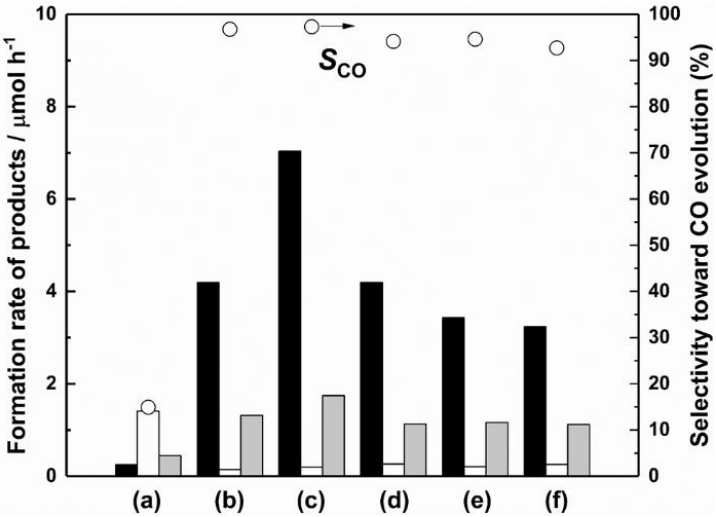


**Fig. 7** Photocatalytic reduction of $CO_2$ over the prepared samples with different loading amount of $MnO_x$ species, (a) Bare KTO, (b) Ag(PD,1.0)/KTO, (c) Ag(PD,1.0)-Mn(PD,0.09)/KTO, (d) Ag(PD,1.0)/$MnO_x$(IMP,0.1)/KTO, (e) Ag(PD,1.0)/$MnO_x$(IMP,0.5)/KTO, and (f) Ag(PD,1.0)/$MnO_x$ (IMP,1.0)/KTO.

Additional sample was prepared by a successive PD method, the Ag species were first deposited by the PD method, followed by the photodeposition of $MnO_x$ species. It was found that no matter whether the $MnO_x$ and Ag cocatalyst were loaded by a PD method simultaneously or separately, the photocatalytic activity was very equal to each other in Fig. 8, which suggested that the effect $MnO_x$ cocatalyst over the KTO sample was independence of the order in the photodeposition. As reported on $TiO_2$ photocatalyst,[46] Ag cocatalyst and the $MnO_x$ cocatalyst may be deposited at different sites on the KTO photocatalyst also.

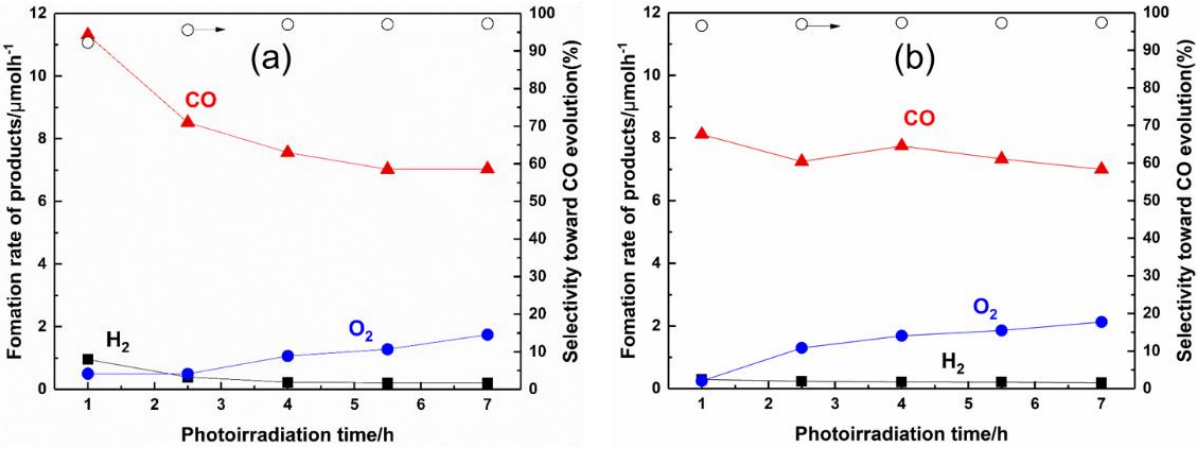


**Fig. 8** Formation rate of CO, $H_2$, and $O_2$ and $R(e^-/h^+)$ in the photocatalytic $CO_2$ reduction over the Ag(PD)-Mn(PD)/KTO samples, (a) by a PD method simultaneously, (b) by a PD method separately.

The Ag(PD,1.0)/$MnO_x$(IMP,1.0)/KTO sample having the metallic Ag species and $MnO_2$ species exhibited the second higher activity toward CO evolution among the tested samples (Fig. 4f). The Ag(PD,1.0)-$MnO_x$(PD,0.09)/KTO sample having the metallic Ag species and the unique $MnO_x$ species exhibited the highest photocatalytic performance. This suggests that the highest activity might originate from the state of loaded $MnO_x$ species on the surface.

It has been reported that the metallic Ag cocatalyst can promote the photocatalytic $CO_2$ reduction to CO in many cases. Also, the effect of the MnOx species loading amount difference was excluded according to the results of Fig.7. In our previous study,[47] the $MnO_x$ species were proved to enhance the $O_2$ evolution, and then accelerate the photocatalytic $CO_2$ reduction to CO. Here, $O_2$ evolution experiments were conducted with five different prepared samples having similar amount of $MnO_x$ species in the presence of a sacrificial oxidant ($AgNO_3$), where the initial formation rate should be compared. As shown in Fig. 9, the addition of $MnO_x$ cocatalyst both in PD and IMP methods on the photocatalyst can enhance the $O_2$ evolution,

and the Ag(PD,0.5)/$MnO_x$(IMP,0.15)/KTO sample also gave more $O_2$ evolution than that of the Ag(PD,0.5)/KTO sample and bare KTO sample. These results concluded that the chemical state of $MnO_x$ has a small effect on the function of $MnO_x$ cocatalyst as for the enhancement of $O_2$ evolution. Other explanation should be responsible for the high activity.

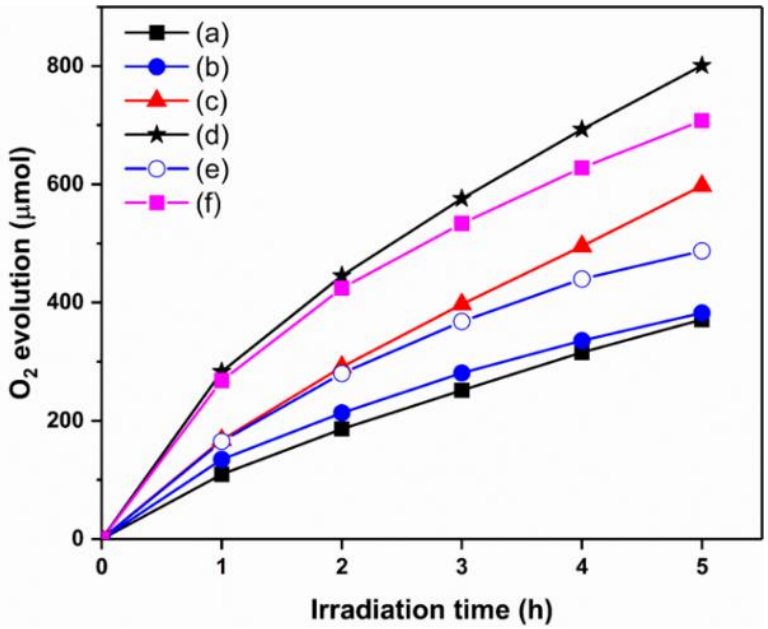


**Fig. 9** Time course of $O_2$ evolution over the prepared photocatalysts. Sacrificial reagent: $AgNO_3$ (0.5 M). Light source: a 100 W high pressure Hg lamp, (a) bare KTO, (b) Ag(PD,0.5/KTO, (c) Ag(PD,0.5)-Mn(PD,0.13)/KTO, (d) $MnO_x$(PD,0.15)/KTO, (e) Ag(PD,0.5)/$MnO_x$(IMP,0.15)/KTO, and (f) $MnO_x$(IMP,0.15) /KTO.

## 3.3 Chemical state, local structure, and function of the dual cocatalyst

The chemical state and local structure of the dual cocatalyst consisting of the Ag and $MnO_x$ species were investigated by using X-ray absorption fine structure (XAFS). Fig. 10A shows Ag K-edge X-ray absorption near edge structures (XANES) of the four prepared samples and two reference samples. For the Ag(PD,1.0)/KTO, Ag(PD,1.0)-$MnO_x$(PD,0.09)/KTO and Ag(PD,1.0)/$MnO_x$(IMP,1.0)/KTO samples (Fig. 10A c, d and g), the absorption edges (25519 eV) in the spectra of the photocatalyst samples were consistent with that of Ag foil (25519 eV) but different from that of $Ag_2O$ (25521 eV), and the spectral feature of XANES for the photocatalyst samples is similar to that for Ag foil. These facts indicate that the Ag species loaded on the surface in these samples were metallic. Thus, it was revealed that the coexistence of Mn species over these samples did not vary the metallic state of Ag cocatalyst. On the other hand,

for the Ag(IMP,1.0)-$MnO_x$(IMP,1.0)/KTO and $MnO_x$(IMP,1.0)/Ag(PD,1.0)/KTO samples (Fig. 10A e, f), the absorption edges in the spectra of the photocatalyst samples were neither consistent with that of Ag foil nor with $Ag_2O$. Since the samples were calcined at 723 K in the last step of the preparation procedure, the Ag species would be oxidized. Thus, it is suggested that the Ag species were not metallic but of unique structure. The Fourier transforms of EXAFS spectra also suggest almost the same feature for the photocatalyst samples (Fig. 10B). The spectra of the Ag(IMP,1.0)-$MnO_x$(IMP,1.0)/KTO and $MnO_x$(IMP,1.0)/Ag(PD,1.0)/KTO samples were very weak, suggesting that the Ag species did not have uniformed local structure. and the XRD results shown in Fig. 11 was failed to detect the Ag patterns.

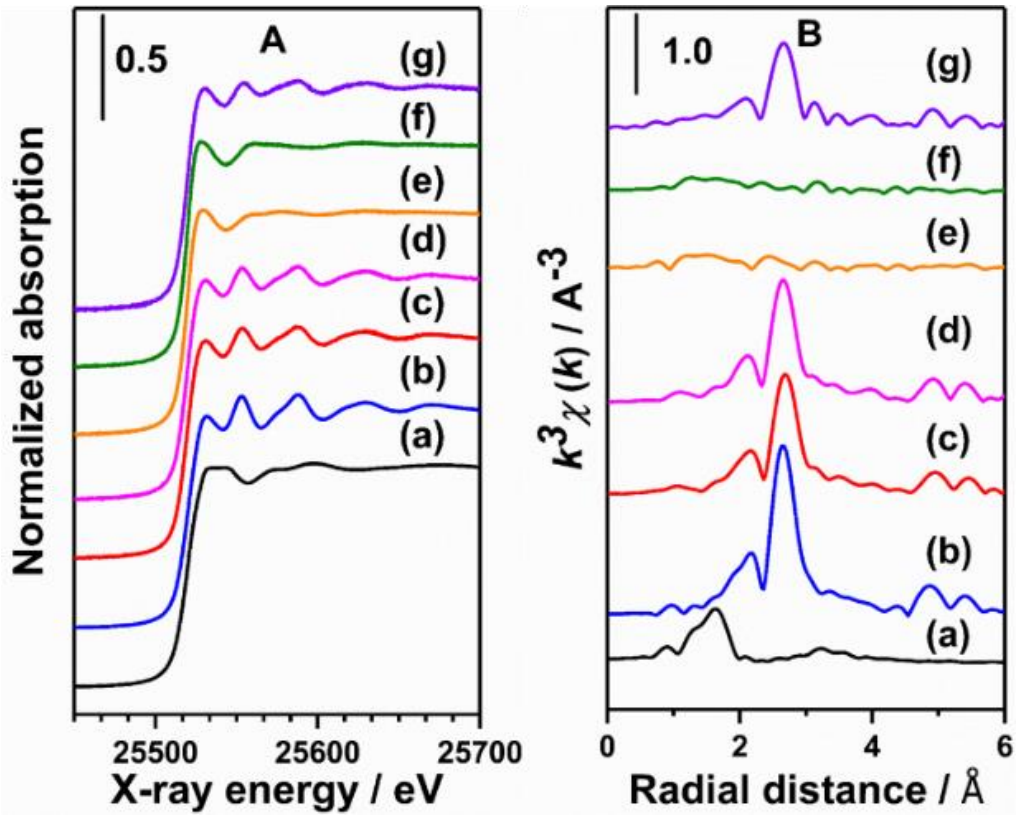


**Fig. 10** Ag K-edge XANES (A) and Fourier-transformed EXFAS (B) of the reference samples, (a) $Ag_2O$ and (b) Ag foil, and the prepared samples, (c) Ag(PD,1.0)/KTO, (d) Ag(PD,1.0)-$MnO_x$(PD,0.09)/KTO, (e) Ag(IMP,1.0)-$MnO_x$(IMP,1.0)/KTO, (f) $MnO_x$(IMP,1.0)/Ag(PD,1.0)/KTO, and (g) Ag(PD,1.0)/$MnO_x$(IMP,1.0)/KTO.

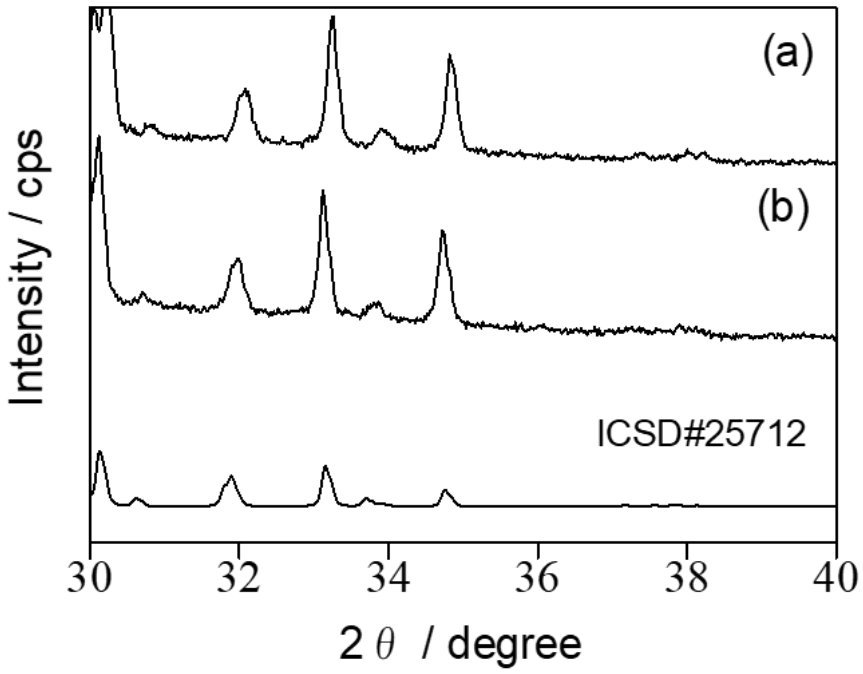


**Fig. 11** XRD patterns of prepared sample and database for KTO (ICSD#25712), (a) Ag(IMP,1.0)-$MnO_x$(IMP,1.0)/KTO and (b) $MnO_x$(IMP,1.0)/Ag(PD,1.0)/KTO.

Fig. 12A shows Mn K-edge XANES of the prepared samples and some reference compounds such as Mn foil, MnO, $Mn_2O_3$, and $MnO_2$. Except for the Ag(PD,1.0)-$MnO_x$(PD,0.09)/KTO sample (Fig. 10Ae), the absorption edges for other three prepared samples (Fig. 12A f, g, and h) were strictly consistent with those for $MnO_2$ (Fig. 12d), meaning that the $Mn^{2+}$ precursor was oxidized by calcination to become $MnO_2$ species deposited on the photocatalyst surface. The Fourier transforms of EXAFS spectra of these three photocatalyst samples also support the formation of $MnO_2$ species. While for the Ag(PD,1.0)-$MnO_x$(PD,0.09)/KTO sample, it had clearly different local structures from these typical manganese oxides. In detail, the edge position of the spectrum for the Ag(PD,1.0)-$MnO_x$(PD,0.09)/KTO sample (Fig. 12Ae) was close to that for $Mn_2O_3$ (Fig. 12Ac). The Fourier transforms of the EXAFS spectra of the photocatalyst samples also showed different features from those of the reference oxides (Fig. 12Be). Thus, the Mn species deposited on the KTO surface by the simultaneous PD method would have the unique local structures, suggesting that they are not aggregated as a single phase of manganese oxide particles but well dispersed on the surface with unique local structure and valences.

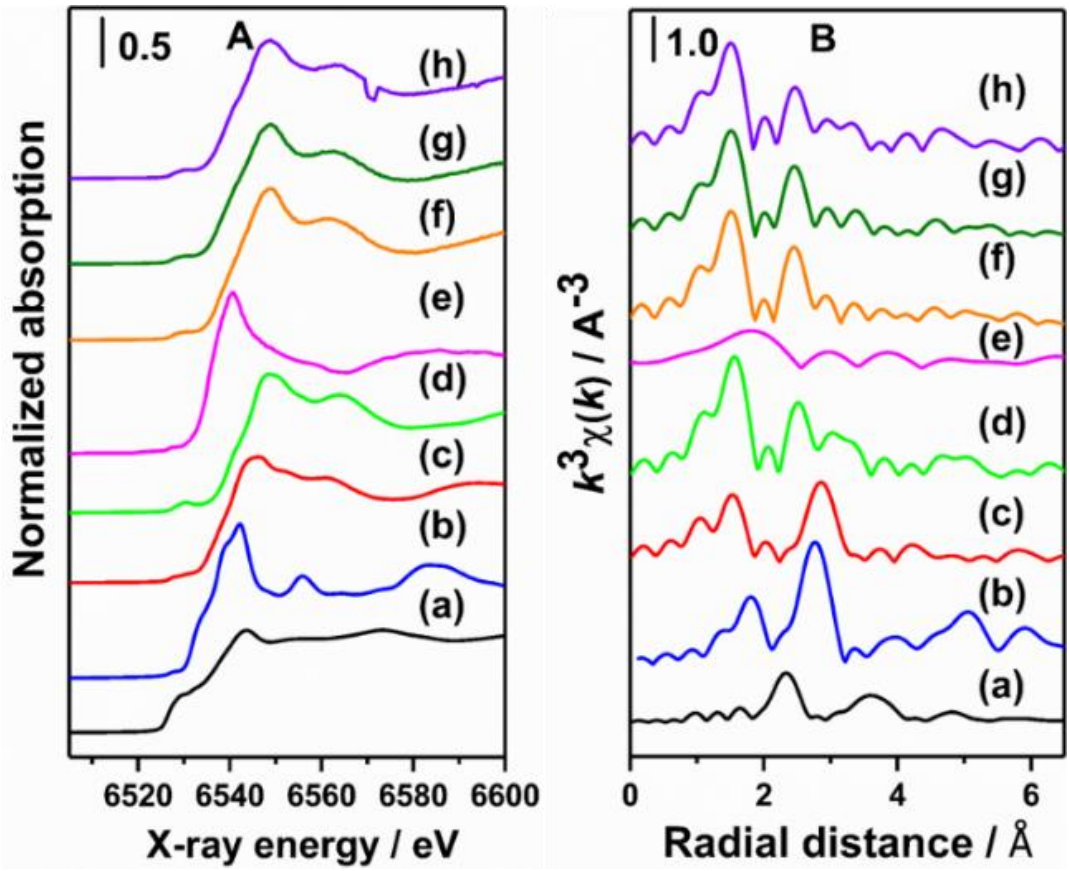


**Fig. 12** Mn K-edge XANES (A) and Fourier-transformed EXFAS (B) of the reference samples, (a) Mn foil, (b) MnO, (c) $Mn_2O_3$, and (d) $MnO_2$, and the prepared samples, (e) Ag(PD,1.0)-$MnO_x$(PD,0.09)/KTO, (f) Ag(IMP,1.0)-$MnO_x$(IMP,1.0)/KTO, (g) $MnO_x$(IMP,1.0)/Ag(PD,1.0)/KTO, and (h) Ag(PD,1.0)/$MnO_x$(IMP,1.0)/KTO.

## 3.3 Location of the dual cocatalyst

TEM images of the Ag(PD,1.0)/KTO and Ag(PD,1.0)-$MnO_x$(PD,0.09)/KTO samples confirmed the presence of Ag nanoparticles on the KTO crystals. However, since Mn species was not detected on the latter sample by TEM and EDS mapping, it was proposed that the Mn species were well dispersed on the surface. Also in the present study, although both TEM and EDS mapping were recorded on the Ag(PD,1.0)-$MnO_x$(PD,0.12)/KTO clear information was not obtained (Fig. 13).

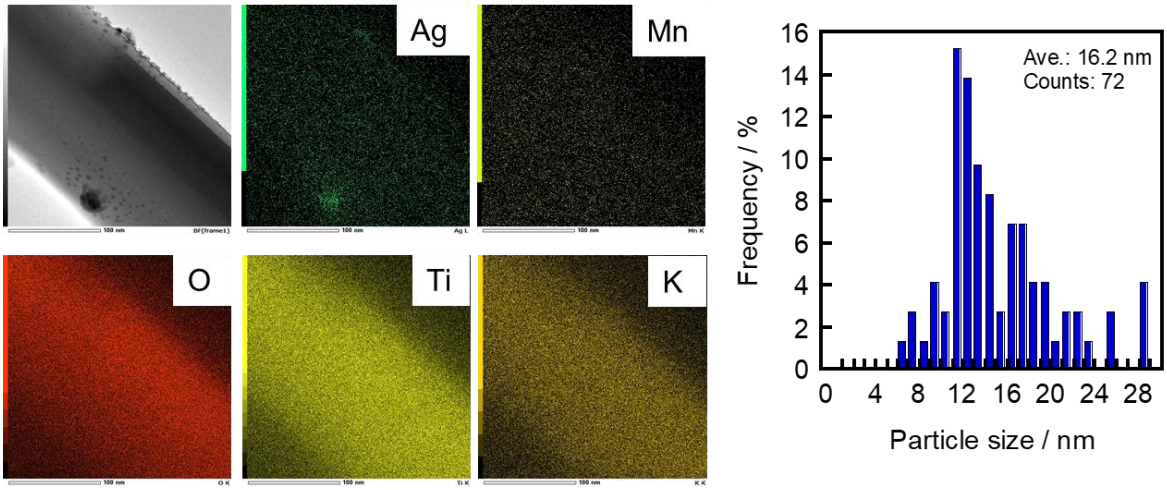


**Fig. 13** STEM EDS mapping and size distribution of Ag nanoparticles of prepared Ag(PD,1.0)-Mn(PD,0.12)/KTO sample.

Fig. 14 shows the TEM images and size distribution of Ag nanoparticle over several samples. The average particle size of the Ag nanoparticles on the Ag(PD,1.0)/KTO, Ag(PD,1.0)-$MnO_x$(PD,0.09)/KTO, and Ag(PD,1.0)-$MnO_x$(PD,0.17)/KTO samples having the same loading amount of the Ag nanoparticles were 15.1 nm, 7.8 nm, and 17.1 nm respectively. It seems that the Ag particle size was not affected by the presence and the loading amount of the $MnO_x$ species. And most of Ag nanoparticles were found on the long facet instead of short facets, and this suggests that the active site for the $CO_2$ reduction were the long facets of potassium hexatitanate.

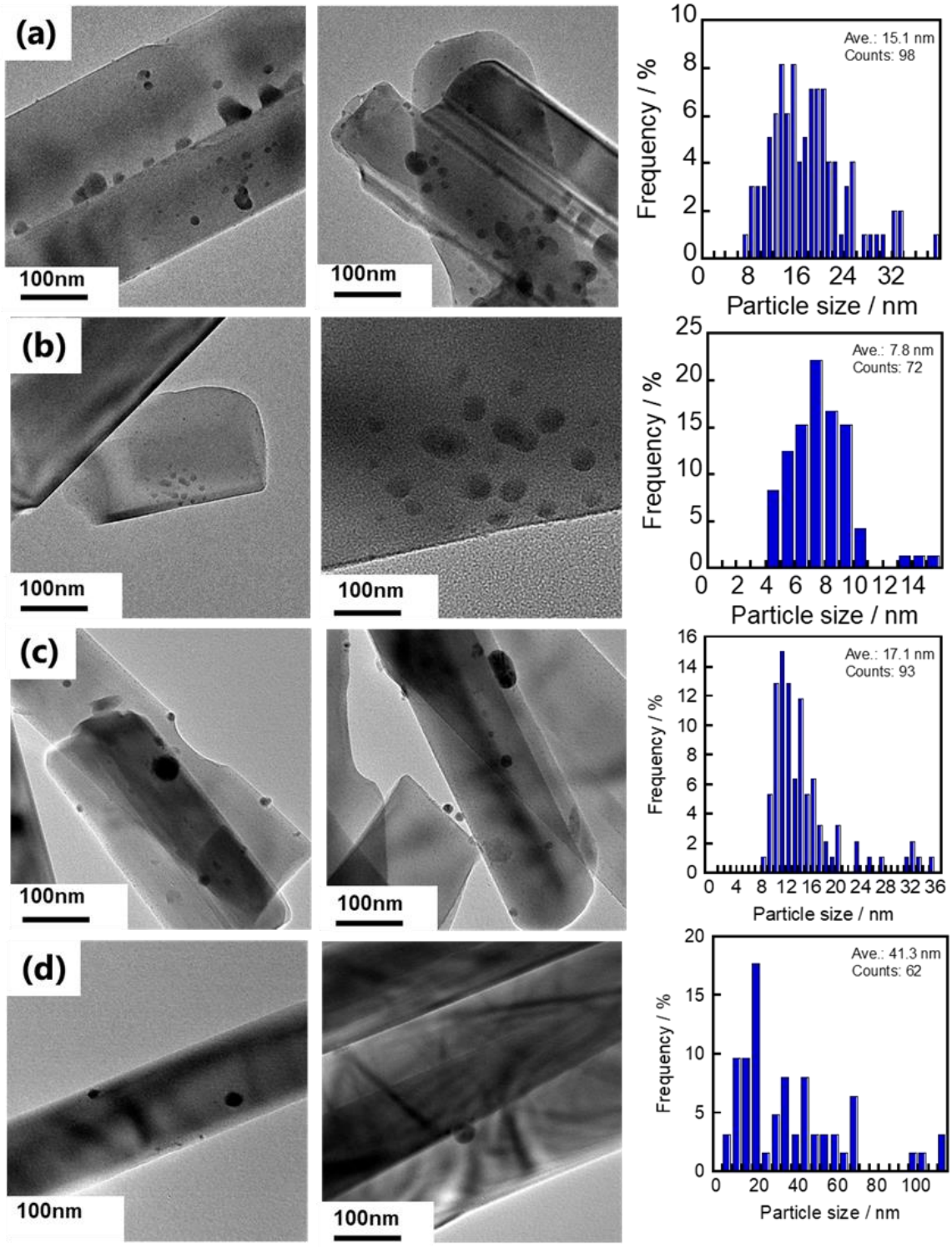


**Fig. 14** TEM images and size distribution of Ag nanoparticles of prepared Ag/KTO samples, (a)Ag(PD,1.0)/KTO, (b) Ag(PD,1.0)-$MnO_x$(PD,0.09)/KTO, (c) Ag(PD,1.0)-$MnO_x$(PD,0.17)/KTO, and (d) Ag(PD,0.5)- $MnO_x$(PD,0.13)/KTO.

To confirm which facets correspond to the reductive and oxidative facets, large amounts of the Ag and $MnO_x$ species were deposited by a photodeposition method as follows. The Ag species were

photodeposited in the presence of $CH_3OH$ as electron donor (referred to as $PD_{MeOH}$), while the $MnO_x$ species were photodeposited by using $IO_3^-$ as an electron acceptor (referred to as $PD_{IO3}$). The photoirradiation was carried out for 2 hours for each photodeposition. Three samples, the Ag($PD_{MeOH}$,5.0)/KTO, $MnO_x$($PD_{IO3}$,5.0)/KTO sample, and $MnO_x$($PD_{IO3}$,5.0)/Ag($PD_{MeOH}$,5.0)/KTO samples, were prepared, where the last one was prepared by a two-step photodeposition: Ag cocatalyst was loaded firstly by a $PD_{MeOH}$ method, followed by the $MnO_x$ loading by the $PD_{IO3}$ method. And it was confirmed by the XRF measurement that all the precursor was successfully deposited on the surface of KTO samples by the aid of the sacrificial reagents. The SEM and TEM images are shown in Fig. 15, where the Ag nanoparticles and the amorphous-like $MnO_x$ species were found on the long and short facets, respectively. Their structures and locations were further confirmed by the combination of TEM images and EDS mapping shown in Fig. 16. For the Ag($PD_{MeOH}$,5.0)/KTO sample (Fig. 16a), almost all Ag cocatalyst was loaded on the long facets, and no Ag nanoparticles were found on the short facets of the KTO sample. For the $MnO_x$($PD_{IO3}$,5.0) sample (Fig. 16b), many particles covering on the short facets were observed and only a few particles were found on the long facets. When both Ag and $MnO_x$ cocatalyst were loaded successively on the KTO sample (Fig. 16c), both the long facets and short facets were deposited by the Ag and $MnO_x$ species, respectively, which was evidenced by EDS mapping.

It was well known that oxidation cocatalyst was easy to be loaded on hole-rich facets, and reduction cocatalyst preferred to be loaded on the electron-rich facet.[41,53] In the present preparation condition without any sacrificial reagents, the following oxidation and reduction (eq. 5 and 6) would occur except for the reduction of proton and oxidation of water.[46]

$$Ag^+ + e^- \rightarrow Ag \quad (5)$$

$$Mn^{2+} + 2h^+ + 2H_2O \rightarrow \quad Mn(IV)O_2 + 4H^+ \quad (6)$$

$$2Mn^{2+} + 2h^+ + 3H_2O \rightarrow \quad Mn_2(III)O_3 + 6H^+ \quad (7)$$

The separately-located $MnO_x$ species and Ag nanoparticles can act as an oxidation cocatalyst and a reduction cocatalyst, respectively, on each facet, which provides the separately-located reaction fields for the photocatalytic reactions, limits the recombination of electrons and holes, and increases the photocatalytic activities.

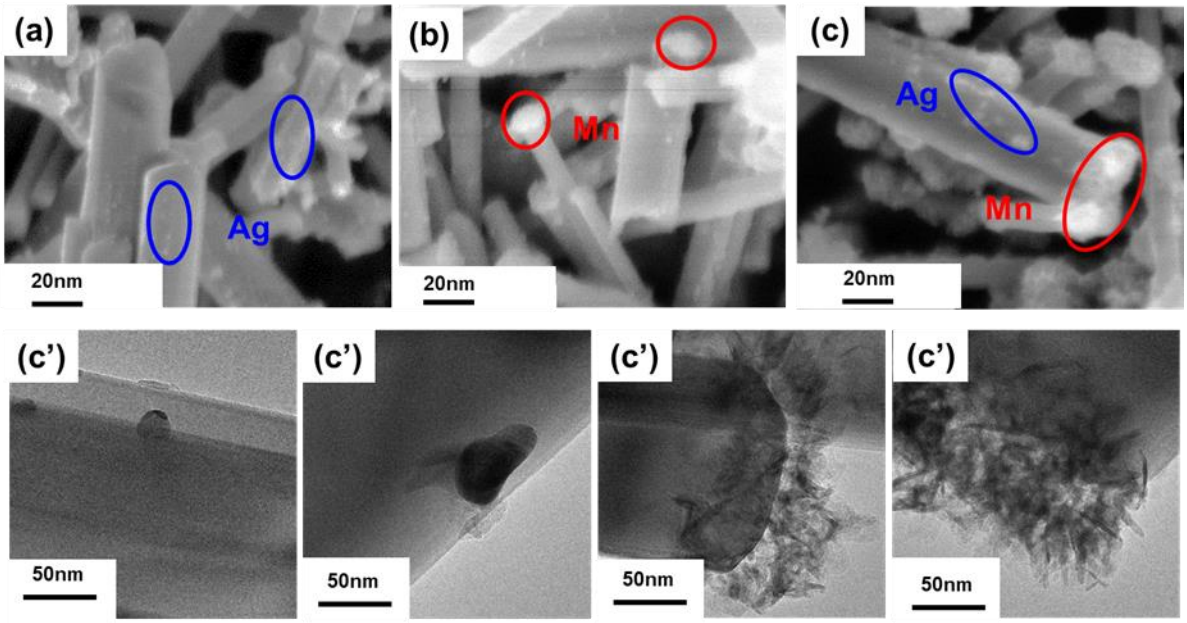


**Fig. 15** SEM and TEM images of the (a) Ag(PD($CH_3OH$),5.0)/KTO, (b) $MnO_x$(PD($NaIO_3$),5.0)/KTO and (c) $MnO_x$(PD($NaIO_3$),5.0)/Ag(PD($CH_3OH$),5.0)/KTO samples, and c' was the TEM images of sample c, here $NaIO_3$ was used as sacrificial reagent for loading the $MnO_x$ cocatalyst.

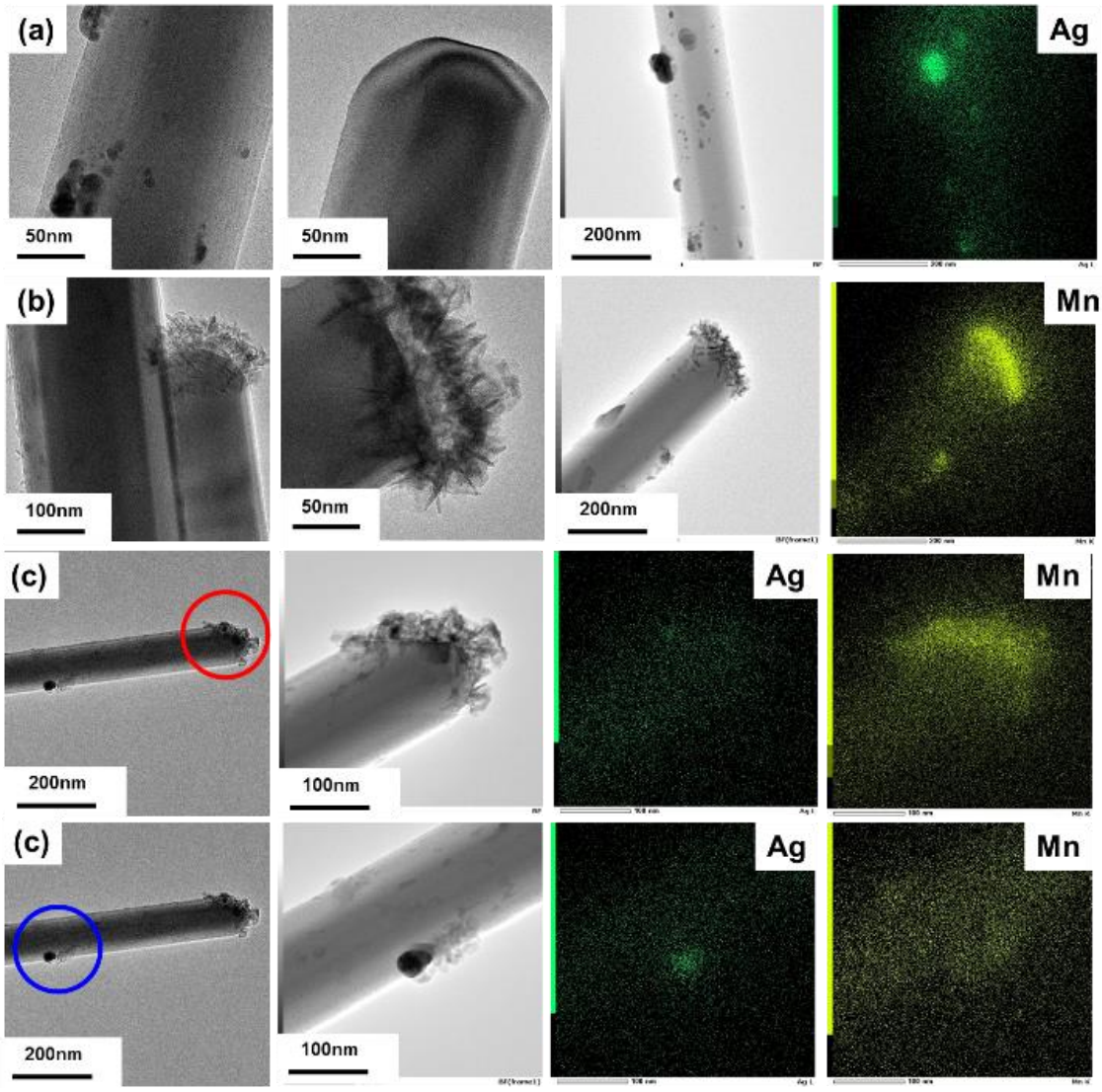


**Fig. 16** TEM images and EDS mapping of the (a) Ag(PD($CH_3OH$),5.0)/KTO, (b) $MnO_x$(PD($NaIO_3$),5.0)/KTO and (c) $MnO_x$(PD($NaIO_3$),5.0)/Ag(PD($CH_3OH$),5.0)/KTO samples, here $NaIO_3$ was used as sacrificial reagent for loading the $MnO_x$ cocatalyst.

Fig. 17 shows TEM images and EDS mappings of the $MnO_x$(IMP,1.0)/Ag(PD,1.0)/KTO sample, in which different structure of cocatalyst were observed. Firstly, an apparent core-shell structure was found. It was supposed that the particles of core-shell structure consisted of Ag and $MnO_x$ moieties, since the Ag species usually existed as a particle, and $MnO_x$ species would be loaded on the surface of the photocatalyst in the form of amorphous structure. On the other hand, some aggregates of Ag nanoparticles were also found even on the short facets. Since it is not dark in TEM image, these aggregated Ag particles would be oxidized, which consisted with the results from XAFS (Fig. 10). During the preparation procedure for this sample, the Ag cocatalyst

was loaded first by a PD method, followed by the $MnO_x$ was loaded via an IMP method. This means that the sample were finally calcined at 723 K, and during the calcination process the first-produced Ag nanoparticles should be oxidized and migrate even to short facet. The activity of this sample was quite low due to two reasons; one is the oxidation of Ag species, and the other one is the decreased number of Ag cocatalyst due to coverage of the $MnO_x$ cocatalyst and aggregation. The core-shell structure in this study as well as Ag oxide cocatalyst were proved to give a negative effect on the photocatalytic reduction of $CO_2$ with $H_2O$.

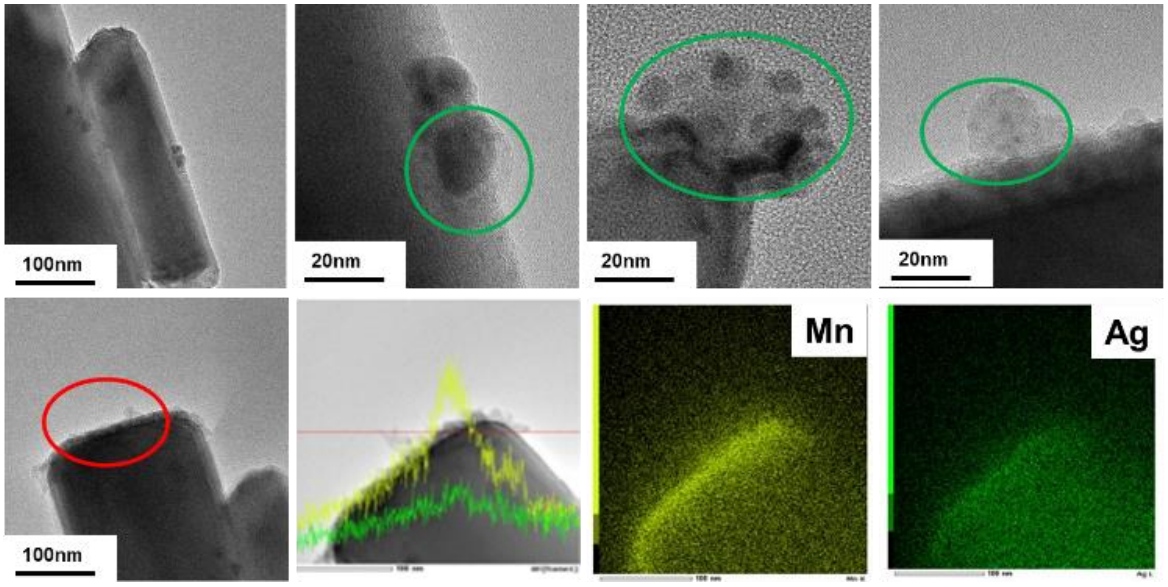


**Fig. 17** TEM images and EDS mappings of $MnO_x$(IMP,1.0)/Ag(PD,1.0)/KTO sample.

Finally, Fig. 18 shows TEM images and EDS mapping of the Ag(PD,1.0)/$MnO_x$(IMP,1.0)/KTO sample. The combination of TEM image and EDS mapping shows that both the Ag and $MnO_x$ species was well dispersed on the surface of the KTO sample, this is the reason why the activity of this sample is high but not the highest. Although the Ag nanoparticles loaded in the PD method predominantly exist on the long facets, the $MnO_x$ species are present everywhere. Although the $MnO_x$ species loaded by the IMP method can enhance the photocatalytic oxidation as shown in Fig. 4, the $MnO_x$ species closed to the Ag species on the long facets may disturb the photocatalytic reduction.

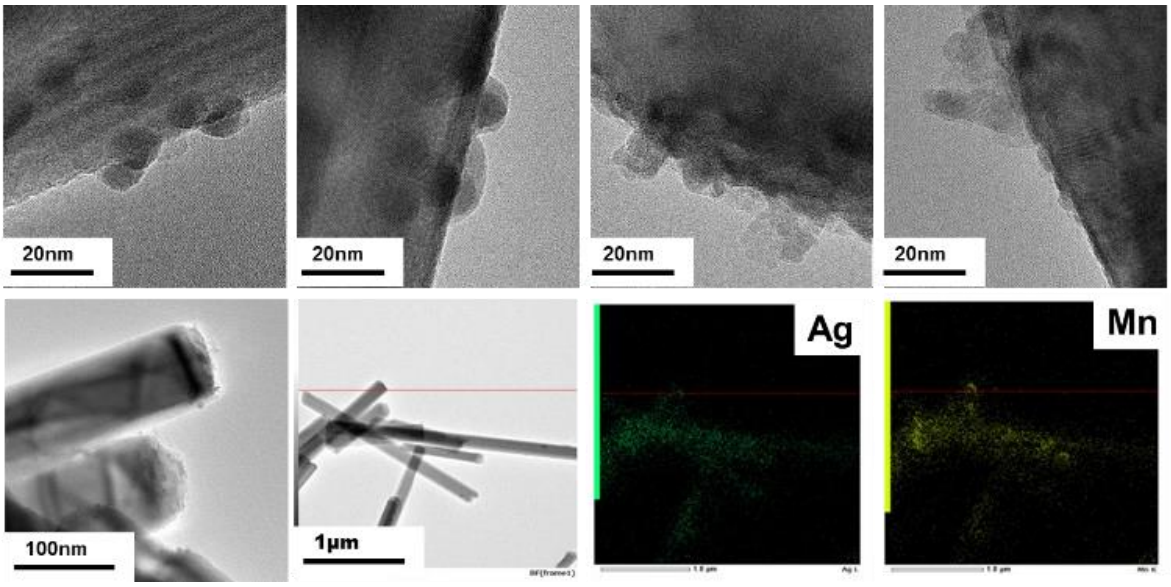


**Fig. 18** TEM images and EDS mappings of Ag(PD,1.0)/$MnO_x$(IMP,1.0)/KTO samples.

## 4. Conclusion

In this study, the different deposition methods for loading dual cocatalysts were investigated to figure out the relationship between the $MnO_x$ and Ag cocatalyst. It was found that the deposition method could affect not only the chemical state, particle size of Ag cocatalyst, but also the structure of loaded cocatalyst shown in Fig. 19, and it resulted in the different effect on the photocatalytic activity. Here it was proved that metallic Ag cocatalyst and the suitable nanoparticle size of Ag cocatalyst are both essential to promote the reaction occurrence on the surface of Ag cocatalyts in the photocatalytic reduction of $CO_2$ system. Also, a core-shell structure of dual cocatalyst was evidence to inhibit the activity towards $CO_2$ reduction due to the block of active sites of Ag cocatalyst. While we successfully found a valuable method, dual cocatalysts loaded by a simultaneous method, could maintain nanoparticle size of Ag cocatalyst and deposited Ag and $MnO_x$ cocatalyst on the long facets and short facets separately, indicates the reductive facets and oxidative facets, respectively, which was the other explanation of high activity of CO reduction as well as the enhancement of $O_2$ evolution reported in our previous study.

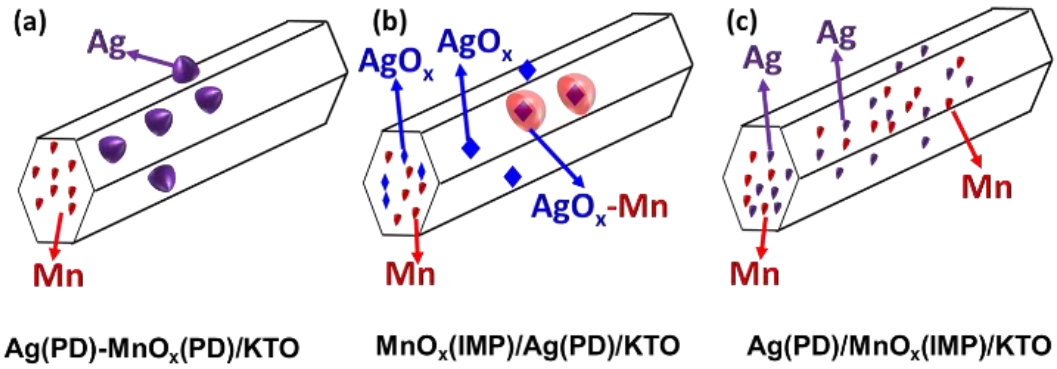


**Fig. 19** Different deposited sites on a sliver-manganese loaded potassium hexatitanate photocatalyst surface, (a)Ag(PD)-$MnO_x$(PD)/KTO; (b) $MnO_x$(IMP)/Ag(PD)/KTO; (c) Ag(PD)/$MnO_x$(IMP)/KTO.

**References**


1 W. Fan, Q. Zhang and Y. Wang, *Phys. Chem. Chem. Phys.*, 2013, **15**, 2632–2649.

2 G. Zhao, X. Huang, X. Wang and X. Wang, *J. Mater. Chem. A*, 2017, **5**, 21625–21649.

3 K. Li, X. An, K. H. Park, M. Khraisheh and J. Tang, *Catal. Today*, 2014, **224**, 3–12.

4 B. Kumar, M. Llorente, J. Froehlich, T. Dang, A. Sathrum and C. P. Kubiak, *Annu. Rev. Phys. Chem.*, 2012, **63**, 541–569.

5 S. N. Habisreutinger, L. Schmidt-Mende and J. K. Stolarczyk, *Angew. Chemie - Int. Ed.*, 2013, **52**, 7372–7408.

6 J. Low, B. Cheng and J. Yu, *Appl. Surf. Sci.*, 2017, **392**, 658–686.

7 K. Iizuka, T. Wato, Y. Miseki, K. Saito and A. Kudo, *J. Am. Chem. Soc.*, 2011, **133**, 20863–20868.

8 S. Xie, Y. Wang, Q. Zhang, W. Deng and Y. Wang, *ACS Catal.*, 2014, **4**, 3644–3653.

9 K. Kočí, L. Obalová, L. Matějová, D. Plachá, Z. Lacný, J. Jirkovský and O. Šolcová, *Appl. Catal. B Environ.*, 2009, **89**, 494–502.

10 A. Hammad, A. Anzai, X. Zhu, A. Yamamoto, D. Ootsuki, T. Yoshida, A. EL-Shazly, M. Elkady and H. Yoshida, *Catal. Letters*, , DOI:10.1007/s10562-019-02997-z.

11 Z. Wang, K. Teramura, S. Hosokawa and T. Tanaka, *Appl. Catal. B Environ.*, 2015, **163**, 241–247.

12 H. Tatsumi, K. Teramura, Z. Huang, Z. Wang, H. Asakura, S. Hosokawa and T. Tanaka, *Langmuir*, 2017, **33**, 13929–13935.

13 K. Teramura, Z. Wang, S. Hosokawa, Y. Sakata and T. Tanaka, *Chem. - A Eur. J.*, 2014, **20**, 9906–9909.

14 S. Iguchi, Y. Hasegawa, K. Teramura, S. Kidera, S. Kikkawa, S. Hosokawa, H. Asakura and T. Tanaka, *Sustain. Energy Fuels*, 2017, **1**, 1740–1747.

15 M. Yamamoto, T. Yoshida, N. Yamamoto, T. Nomoto, Y. Yamamoto, S. Yagi and H. Yoshida, *J. Mater. Chem. A*, 2015, **3**, 16810–16816.

16 R. Pang, K. Teramura, H. Asakura, S. Hosokawa and T. Tanaka, *Appl. Catal. B Environ.*, 2017, **218**, 770–778.

17 Z. Huang, S. Yoshizawa, K. Teramura, H. Asakura, S. Hosokawa and T. Tanaka, *ACS Sustain. Chem. Eng.*, 2018, **6**, 8247–8255.

18 H. Yoshida, L. Zhang, M. Sato, T. Morikawa, T. Kajino, T. Sekito, S. Matsumoto and H. Hirata, *Catal. Today*, 2015, **251**, 132–139.

19 A. Anzai, N. Fukuo, A. Yamamoto and H. Yoshida, *Catal. Commun.*, 2017, **100**, 134–138.

20 H. Yoshida, M. Sato, N. Fukuo, L. Zhang, T. Yoshida, Y. Yamamoto, T. Morikawa, T. Kajino, M. Sakano, T. Sekito, S. Matsumoto and H. Hirata, *Catal. Today*, 2018, **303**, 296–304.

21 X. Zhu, A. Anzai, A. Yamamoto and H. Yoshida, *Appl. Catal. B Environ.*, 2019, **243**, 47–56.

22 L. F. Garay-Rodríguez, H. Yoshida and L. M. Torres-Martínez, *Dalt. Trans.*, 2019, **48**, 12105–12115.

23 V. Jeyalakshmi, S. Tamilmani, R. Mahalakshmy, P. Bhyrappa, K. R. Krishnamurthy and B. Viswanathan, *J. Mol. Catal. A Chem.*, 2016, **420**, 200–207.

24 S. Iguchi, K. Teramura, S. Hosokawa and T. Tanaka, *Appl. Catal. A Gen.*, 2016, **521**, 160–167.

25 C. Xin, M. Hu, K. Wang and X. Wang, *Langmuir*, 2017, **33**, 6667–6676.

26 26 R. Pang, K. Teramura, H. Tatsumi, H. Asakura, S. Hosokawa and T. Tanaka, *Chem. Commun.*, 2018, **54**, 1053–1056.

27 H. Nakanishi, K. Iizuka, T. Takayama, A. Iwase and A. Kudo, *ChemSusChem*, 2017, **10**, 112–118.

28 M. Asadi, K. Kim, C. Liu, A. V. Addepalli, P. Abbasi, P. Yasaei, P. Phillips, A. Behranginia, J. M. Cerrato, R. Haasch, P. Zapol, B. Kumar, R. F. Klie, J. Abiade, L. A. Curtiss and A. Salehi-Khojin, *Science (80-. ).*, 2016, **353**, 467–470.

29 K. Teramura, H. Tatsumi, Z. Wang, S. Hosokawa and T. Tanaka, *Bull. Chem. Soc. Jpn.*, 2015, **88**, 431–437.

30 J. Yang, H. Yan, X. Wang, F. Wen, Z. Wang, D. Fan, J. Shi and C. Li, *J. Catal.*, 2012, **290**, 151–157.

31 Y. Ma, R. Chong, F. Zhang, Q. Xu, S. Shen, H. Han and C. Li, *Phys. Chem. Chem. Phys.*, 2014, **16**, 17734–17742.

32 M. Yoshida, K. Takanabe, K. Maeda, A. Ishikawa, J. Kubota, Y. Sakata, Y. Ikezawa and K. Domen, *J. Phys. Chem. C*, 2009, **113**, 10151–10157.

33 Y. Bai, L. Ye, L. Wang, X. Shi, P. Wang and W. Bai, *Environ. Sci. Nano*, 2016, **3**, 902–909.

34 Z. Xiong, Z. Lei, C. C. Kuang, X. Chen, B. Gong, Y. Zhao, J. Zhang, C. Zheng and J. C. S. Wu, *Appl. Catal. B Environ.*, 2017, **202**, 695–703.

35 J. Yang, D. Wang, H. Han and C. Li, *Acc. Chem. Res.*, 2013, **46**, 1900–1909.

36 Y. F. Li, Z. P. Liu, L. Liu and W. Gao, *J. Am. Chem. Soc.*, 2010, **132**, 13008–13015.

37 A. Kudo and Y. Miseki, *Chem. Soc. Rev.*, 2009, **38**, 253–278.

38 Z. Chang, S. Huo, W. Zhang, J. Fang and H. Wang, *J. Phys. Chem. C*, 2017, **121**, 11368–11379.

39 Q. Zhai, S. Xie, W. Fan, Q. Zhang, Y. Wang, W. Deng and Y. Wang, *Angew. Chemie - Int. Ed.*, 2013, **52**, 5776–5779.

40 K. Maeda, A. Xiong, T. Yoshinaga, T. Ikeda, N. Sakamoto, T. Hisatomi, M. Takashima, D. Lu, M. Kanehara, T. Setoyama, T. Teranishi and K. Domen, *Angew. Chemie - Int. Ed.*, 2010, **49**, 4096–4099.

41 41 R. Li, F. Zhang, D. Wang, J. Yang, M. Li, J. Zhu, X. Zhou, H. Han and C. Li, *Nat. Commun.*, 2013, **4**, 1432–1437.

42 J. Zhu, S. Pang, T. Dittrich, Y. Gao, W. Nie, J. Cui, R. Chen, H. An, F. Fan and C. Li, *Nano Lett.*, 2017, **17**, 6735–6741.

43 T. Ohno, K. Sarukawa and M. Matsumura, *New J. Chem.*, 2002, **26**, 1167–1170.

44 Z. Li, L. Zhang, Y. Liu, C. Shao, Y. Gao, F. Fan, J. Wang, J. Li, J. Yan, R. Li and C. Li, *Angew. Chemie Int. Ed.*, 2019, 935–942.

45 K. Khan, X. Tao, Y. Zhao, B. Zeng, M. Shi, N. Ta, J. Li, X. Jin, R. Li and C. Li, *J. Mater. Chem. A*, 2019, **7**, 15607–15614.

46 Z. Jiang, D. Ding, L. Wang, Y. Zhang and L. Zan, *Catal. Sci. Technol.*, 2017, **7**, 3065–3072.

47 X. Zhu, A. Yamamoto, S. Imai, A. Tanaka, H. Kominami and H. Yoshida, *Chem. Commun.*,

2019, **55**, 13514–13517.

48 S. Iguchi, K. Teramura, S. Hosokawa and T. Tanaka, *Phys. Chem. Chem. Phys.*, 2015, **17**, 17995–18003.

49 E. A. Davis and N. F. Mott, *Philos. Mag.*, 1970, **22**, 903–922.

50 M. Rycenga, C. M. Cobley, J. Zeng, W. Li, C. H. Moran, Q. Zhang, D. Qin and Y. Xia, *Chem. Rev.*, 2011, **111**, 3669–3712.

51 S. Linic, P. Christopher and D. B. Ingram, *Nat. Mater.*, 2011, **10**, 911–921.

52 L. Lu, A. Kobayashi, K. Tawa and Y. Ozaki, *Chem. Mater.*, 2006, **18**, 4894–4901.

53 Q. Wang and K. Domen, *Chem. Rev.*, , DOI:10.1021/acs.chemrev.9b00201.

# Chapter 6 Modification of silver-loaded potassium titanate photocatalyst by adding metal ions for carbon dioxide reduction with water


## Abstract

Potassium hexatitanate has been studied as an attractive photocatalyst for not only photocatalytic degradation but also water splitting and $CO_2$ reduction. And it has also been reported that the addition of metal ions into photocatalysts is one of the techniques to improve photocatalytic activity. In this study, a screening tests of potassium hexatitanate modified with various metal ions were synthesized by three different methods and examined for the $CO_2$ reduction. It was found that modification of $Sn^{4+}$, $Zr^{4+}$ and $Rb^{+}$ ions improved the activity for photocatalytic $CO_2$ reduction selectively to CO by water. Further optimization revealed that tiny addition of $Ca^{2+}$ such as 0.1 mol% most enhanced CO evolution.


## 6-1 Introduction

The annual $CO_2$ emission steadily increased in the past 35 years due to the tremendous consumption of fossil fuels, which lead to an increase of the average global surface temperature simultaneously. Therefore, the current energetic shortage and climatic problem urge the scientific community to search for environmentally friendly solutions for the long-term development of human society. Among various possibilities, photocatalytic $CO_2$ reduction into green solar fuels has been known as one of the most promising technologies because it can simultaneously produce useful solar fuels and reduce the $CO_2$ concentration in the atmosphere.[1–9] Among these possible reductive products from carbon dioxide, CO is the most useful product since it is a valuable chemical intermediate for further chemical syntheses and easily separable from the aqueous reaction media to the gas phase. Ag cocatalyst was discovered to improve the CO evolution,[10] which has been widely studied in recent years.[11–18] Ensuring the conversion of $CO_2$ into carbon sources as the main products is vital because water splitting to form $H_2$ and $O_2$ is thermodynamically more favorable than $CO_2$ conversion when using $H_2O$ as the electron donor for photocatalysts. However, only a few heterogeneous

photocatalysts, including $BaLa_4Ti_4O_{15}$,[10,19] $Ga_2O_3$,[14,20–23] $ZnTa_2O_6$,[12] $ZnGa_2O_4$,[24] $CaTiO_3$,[25] $SrNb_2O_6$,[11,26] and $K_2Ti_6O_{13}$,[27] and et al. have been clearly demonstrated as suitable photocatalysts for the stoichiometric produce the CO, $O_2$ and $H_2$. However, the photocatalytic activity has not been enough for the practical application. Thus, it is still imperative to develop highly efficient photocatalysts for this reaction.

The low ability of charge separation, wide bandgap and migration and low capacity of $CO_2$ adsorption over surface of the photocatalysts are the three main limitations for the practical application. However, controlling charge separation and immigration is critical because the band structure and crystallographic character of each semiconducting material are unique. The movement of excited electrons and holes, and thus the photocatalytic activity, can be significantly affected by the crystallinity, particle size, and doping. Here, extending the light absorption range of photocatalyst and surface modification are highly desirable.

Generally, the introduction of metallic impurities introduces additional binding functions, which endows the doped system with unique photocatalytic properties by lowering the bandgap and enhancing the absorption of visible light.[28–30] Whether the metal ions are present in the lattice or on the surface is dependent on two vital factors: the preparation conditions and homogeneity of the metal ions in its host oxide. The ionic radius ratio of the cation/anion determines the preference of cations to occupy specific interstitial sites. Interstitial sites may consist of cations with coordination numbers such as 4 (tetrahedral), 6 (octahedral), etc., so both the radius and coordination numbers should be taken into consideration.

Some researchers have reported that the introduction of functional basic sites on the surface of photocatalysts was proved to improve $CO_2$ adsorption and activation.[31–33] Ye and co-workers demonstrated that the addition of MgO to the Pt−$TiO_2$ catalyst significantly increased the selectivity for $CO_2$ reduction, although the rate of electron consumption for reductive reactions did not change dramatically. The presence of MgO remarkably suppressed the $H_2$ evolution and accelerated the reduction of $CO_2$. The synergistic effect between the enhanced $CO_2$ chemisorption and electron density on the surface of MgO and Pt co-promoted $TiO_2$ is proposed to be responsible for the improvement of the selectivity for $CO_2$ reduction.[33] Also, it was demonstrated that the $ZnGa_2O_4$ layer has a particular function to suppress the reduction of $H^+$ in the photocatalytic conversion of $CO_2$ with $H_2O$ over the Ag-loaded Zn-modified $Ga_2O_3$ photocatalyst. Since the generation ratio of $H_2$ to CO can be finely tuned by using the Ag-loaded

Zn-modified $Ga_2O_3$ photocatalyst.[14]

In these reaction systems, the reduction of $CO_2$ and protons with the photoexcited electrons proceed to form CO and $H_2$, respectively on the reductive sites of the photocatalyst surface (Eqs. 1 and 2), while the oxidation of water with positive holes into $O_2$ and protons occurs on the oxidative sites (Eq. 3).

$$CO_2 + 2\ H^+ + 2\ e^- \rightarrow CO + H_2O \quad (1)$$

$$2\ H^+ + 2\ e^- \rightarrow H_2 \quad (2)$$

$$2\ H_2O + 4\ h^+ \rightarrow O_2 + 4\ H^+ \quad (3)$$

When no other reductive products than CO and $H_2$ are observed in the reaction system, the selectivity toward CO evolution, $S_{CO}$(%), and the ratio of the consumed electron and hole, $R(e^-/h^+)$, can be calculated according to Eqs. 4 and 5, respectively, [11,25] where the production rate of CO, $H_2$ and $O_2$ are referred to as $R_{CO}$, $R_{H2}$ and $R_{O2}$, respectively. The value of $R(e^-/h^+)$ should be unity if the two competitive reactions, Eqs. 1, 2 and 3, take place ideally in any balance.

$$S_{CO}\ (\%) = 100 \times R_{CO} / (R_{CO} + R_{H2}) \quad (4)$$

$$R(e^-/h^+) = (2R_{CO} + 2R_{H2})/4R_{O2} \quad (5)$$

Potassium hexatitanate ($K_2Ti_6O_{13}$, referred to as KTO) has been studied as an attractive photocatalyst for not only photocatalytic degradation but also water splitting and $CO_2$ reduction.[34–36] And it has also been reported that the addition of metal ions into photocatalysts is one of the techniques to improve photocatalytic activity.[37] However, few studies have been reported the effects of the addition of metal ions into KTO photocatalyst for the photocatalytic $CO_2$ reduction by water so far. In this study, KTO samples modified with various metal ions by different methods were synthesized and examined for the $CO_2$ reduction.

# 6-2 Experimental

## 6-2.1 Sample preparation

Potassium titanate samples were prepared by a flux method,[38] where the KCl was used as a flux. The prepared KTO sample was treated with KCl flux including a starting material for additional metal (M) ion in the same way to obtain a modified KTO:M sample. The mixture was

put into a platinum crucible, heated in an electric muffle furnace with a rate of 200 K $h^{-1}$ to 1273 K for 10 hours, and then cooled at a rate of −100 K $h^{-1}$ to 773 K, followed by being naturally cooled to room temperature in the furnace. The obtained powder was thoroughly washed with hot water (353 K) for 4 times to remove the residual salt, then dried at 323 K for 24 hours. And some KTO-M samples were prepared by a solid state reaction method (SSR), where the ratio of raw materials $K_2CO_3$, $TiO_2$ and added metal ions was 1.05 : 6 : X%(atom%). The precursors were well mixed for around 30min by using ethanol and heated in the same temperature program as mentioned above.

The surface modification of KTO_M samples was prepared via an IMP method, 1 g of the KTO sample was suspended in 100 mL of ion exchange water with the desired amount of precursor, followed by evaporation at 353 K to remove water, drying for 12 h at 373 K, and calcination at different temperature for 2 h in air.

Dual cocatalysts or Ag cocatalyst was loaded on the surface by a photodeposition method (PD). Here, 1 g of the KTO sample was dispersed in 400 mL of ion-exchanged water containing a required amount of precursors, and a bubbling flow of Ar gas was used to empty the air for 1 hour before photoirradiation. Then the suspension was photoirradiated using a 100 W high-pressure Hg lamp with a bubbling flow of Ar gas for 2 h, followed by filtration and drying at room temperature.

## 6-2.2 Characterization

The added amount of metal ions was evaluated by X-ray florescence analysis with an EDX-8000 (Shimadzu) using an experimentally obtained calibration curve. The crystal structure of the samples was determined by powder X-ray diffraction with Lab X XRD-6000 (Shimazu). Morphologies of the samples were observed by scanning electron microscopy (SEM) images with JSM-890 (JEOL). The diffuse reflectance UV-Vis spectrum was recorded by a V-670 (JASCO). The bandgap was estimated according to the Davis–Mott equation using the Kubelka–Munk function $F(R\infty)$ obtained from the diffuse-reflectance spectrum.[39] The Brunauer–Emmett–Teller (BET) specific surface area was calculated from the amount of N2 adsorption at 77 K, which was measured by a Monosorb (Quantachrome).

## 6-2.3 Photocatalytic reaction

The photocatalytic $CO_2$ reduction tests over the prepared samples (0.3 g) were carried out in an aqueous solution of $NaHCO_3$ by using an inner-irradiation-type reaction vessel equipped

with a 100 W high-pressure mercury lamp, where $CO_2$ was introduced by bubbling with a flow rate of 30mlmin$^{-1}$. The amount of the products ($H_2$, $O_2$, and CO) were determined by using an on-line gas chromatograph.

# 6-3 Results and discussion

## 6-3.1 KTO samples prepared via an IMP method

$Zn^{4+}$ ion added $Ga_2O_3$ combined with proper cocatalyst was reported to show the remarkably high photocatalytic activity to the overall $H_2O$ splitting and $CO_2$ reduction with $H_2O$.[14,21] Particularly, further improvement of photocatalytic performance in $H_2O$ splitting was confirmed on Zn added $Ga_2O_3$ prepared using dilute $CaCl_2$ solution.[40] And it was reported that the addition of some metal ions (such as $Li^+$, $Na^+$, $K^+$, $Rb^+$, $Cs^+$, $Mg^{2+}$, $Al^{3+}$, $Ga^{3+}$, and $In^{3+}$) by an IMP method was effective for significant improvement of the photocatalytic activity of $SrTiO_3$ to overall $H_2O$ splitting.[41] In these cases, it was proved that the addition of metal ions on the photocatalytic materials is one of the effective ways for improving photocatalytic activity. In the current study, the KTO samples were modified with some metal ions by an IMP method, and the photocatalytic activities were tested over the samples loaded with dual cocatalyst. It was found in Fig.1 that although alkali metal ions addition is more effective than the addition of alkaline-earth metal ions, the addition of all tested metal ions gave the negative effects for the $CO_2$ reduction with $H_2O$. These results may be due to the fact that these metal ions were challenging to be added on the surface of the KTO sample by an IMP method or it was effortless to be dissolved during the procedure of cocatalyst loading. And the dual cocatalyst could make the strategy more complicated.

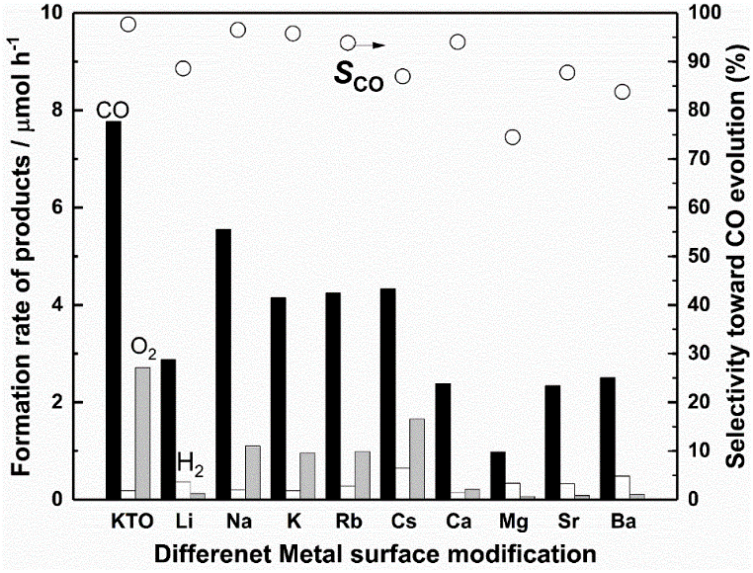


**Fig. 1** Formation rates of CO (black bar), $H_2$ (white bar), and $O_2$ (gray bar) and the CO selectivity ($S_{CO}$%, open circles) in the photocatalytic reaction tests over the $MnO_x$-Ag/KTO_M(1 mol%) samples, where the metal ions were modified by an IMP method, loading amount of $MnO_x$ and Ag cocatalyst was both 1 wt%.

The morphology of most modified samples was recorded in Fig.2, for the KTO_Li sample, some amorphous particles were observed, since the $Li^+$ ion was very active and can react with the KTO sample even at low temperature. Also, some small particles on the surface of the KTO_Mg sample were found. For the other modified samples, no obvious changes were observed, and it was showed that they consisted of same rod-like particles as same as the bare KTO samples.

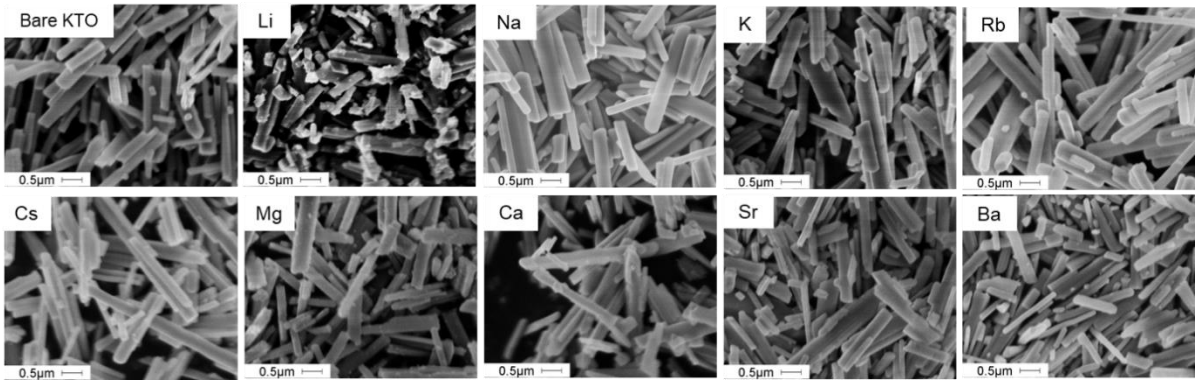


**Fig. 2** SEM images of KTO_M(1 mol%) samples, where the metal ions were modified by an IMP method.

Although the improvement of photocatalytic was not observed in this part, the sodium ion exhibited the highest activity among the tested samples. The effect of the modification

amounts of $Na^+$ ion was also investigated, and the results in Fig.3 show that the activity of $CO_2$ reduction decreased when the amount of $Na^+$ ion was increased. The active surface of the photocatalyst was very significant for the occurrence of photocatalytic reaction, too high modification amount may lead to the decrease of the active surface, which was supposed to be valuable sites for the $CO_2$ reduction.

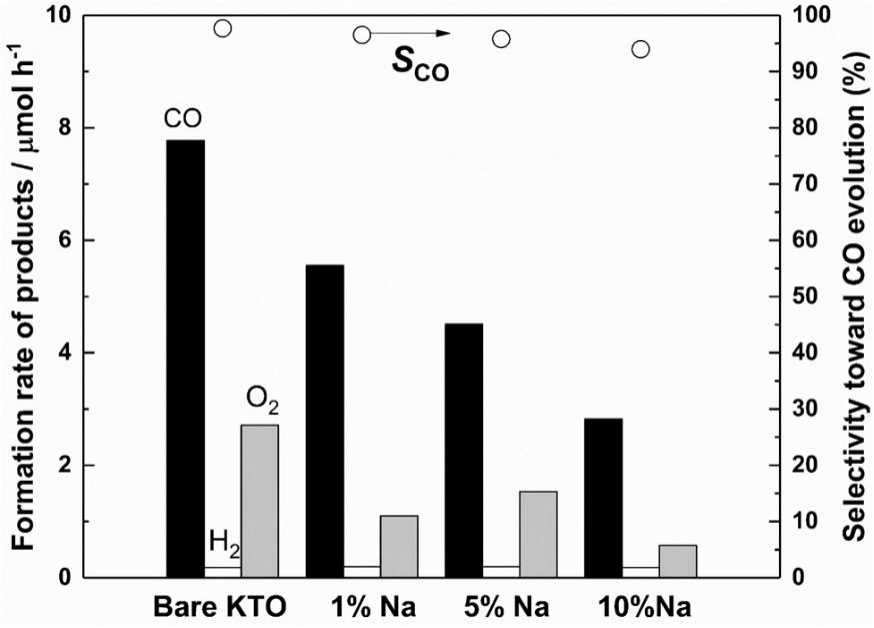


**Fig. 3** Formation rates of CO (black bar), $H_2$ (white bar), and $O_2$ (gray bar) and the CO selectivity ($S_{CO}$%, open circles) in the photocatalytic reaction tests over the $MnO_x$-Ag/KTO_Na(*x* mol%) samples, where loading amount of $MnO_x$ and Ag cocatalyst was both 1 wt%.

## 6-3.2 KTO samples prepared via a flux mediate method

The above discussion indicated that the surface modification of KTO samples by an IMP method seems not effective for the enhancement of photocatalytic activity. Therefore, a screening test was carried out by using the KTO:M samples with 2 mol% of metal ions via a flux mediate method (Fig. 4). And to make it easier to clarify the reason, only Ag cocatalyst instead of dual cocatalyst was loaded on the followed samples. Among the examined metal cations, only $Sn^{4+}$ and $Zr^{4+}$ ions improved the photocatalytic activity of KTO, and the addition of $Zr^{4+}$ ion showed the highest activity for CO evolution. It is considered that only the $Sn^{4+}$ and $Zr^{4+}$ ions could substitute for the $Ti^{4+}$ ions in the KTO sample, since the ionic radius of $Sn^{4+}$ (0.69 Å) and $Zr^{4+}$ cations (0.72 Å) are very close to $Ti^{4+}$ cation (0.61 Å), as shown in table 1. Other metal ions might be difficult to insert into KTO photocatalyst with monoclinic structure and improve the activity.

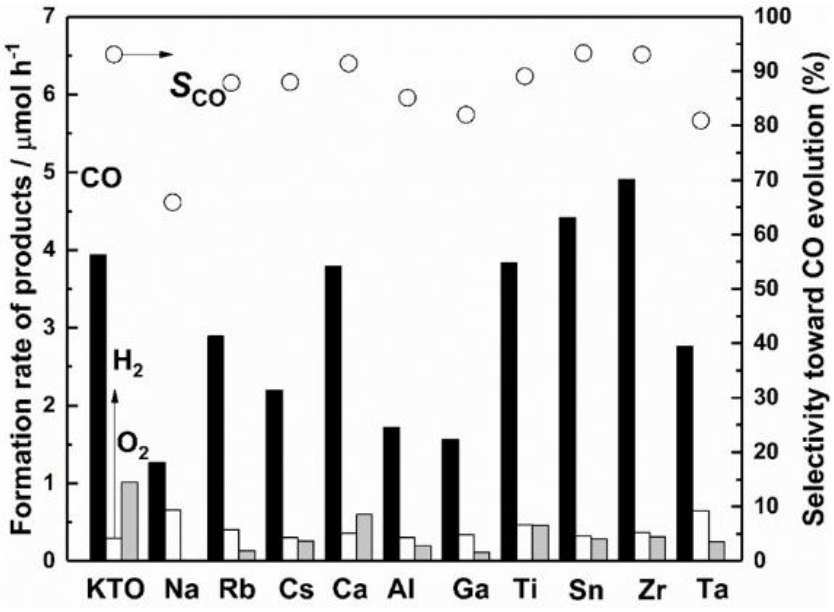


**Fig. 4** Formation rates of CO (black bar), $H_2$ (white bar), and $O_2$ (gray bar) and the CO selectivity ($S_{CO}$%, open circles) in the photocatalytic reaction tests over the 1 wt% Ag/KTO:M(2 mol%) samples, where the metal ions were modified by a flux mediate method.

**Table 1** The coordination number and ionic radius of some metal ions.

| Metal ions | Coordination number | Ionic Radius | Metal ions | Coordination number | Ionic Radius |
|---|---|---|---|---|---|
| $K^+$ | 9 | 1.55 | $Ga^{3+}$ | 6 | 0.62 |
| $Na^+$ | 9 | 1.38 | $Al^{3+}$ | 6 | 0.54 |
| $Rb^+$ | 9 | 1.63 | $Ti^{4+}$ | 6 | 0.61 |
| $Cs^+$ | 9 | 1.78 | $Sn^{4+}$ | 6 | 0.69 |
| $Ba^{2+}$ | 9 | 1.47 | $Zr^{4+}$ | 6 | 0.72 |
| $Sr^{2+}$ | 9 | 1.31 | $Nb^{5+}$ | 6 | 0.64 |
| $Ca^{2+}$ | 6 | 1.00 | $Ta^{5+}$ | 6 | 0.64 |

Since addition of $Ca^{2+}$ ion did not decrease the activity, another series of experiments were also carried out (Fig. 5). It was revealed that the tiny addition of $Ca^{2+}$ enhanced CO evolution, which may be due to the improvement of $CO_2$ adsorption because of the basic property of Ca species. But too much $Ca^{2+}$ ion could introduce some impurity, which decreases the formation rate of CO evolution. Further experiments on the effect of $Ca^{2+}$ ion will also be conducted to explain the mechanism.

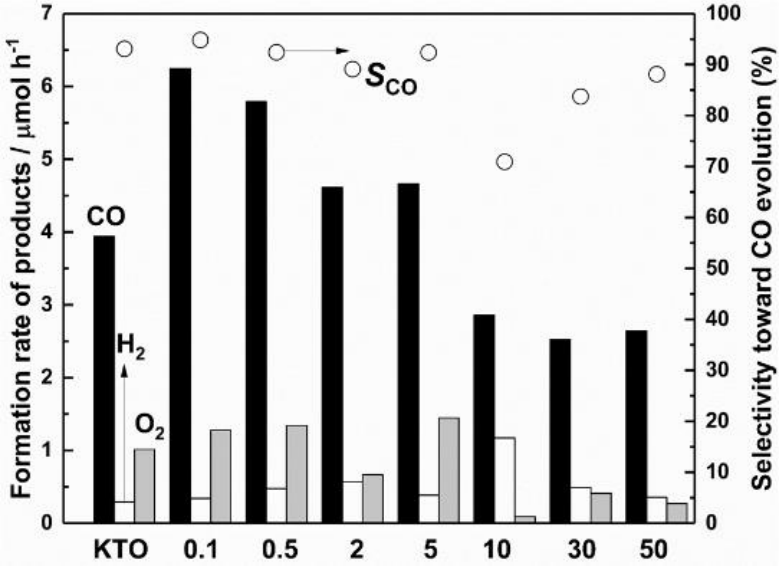


**Fig. 5** Formation rates of CO (black bar), $H_2$ (white bar), and $O_2$ (gray bar) and the selectivity to CO ($S_{CO}$%, open circles) in the photocatalytic reaction tests over the 1 wt% Ag/KTO modified with $Ca^{2+}$ by a flux mediate method.

Whether the $Ca^{2+}$ ion was doped into the lattice or on the surface is still not clear, so further experiments were conducted. Here, some samples modified by the $CaCO_3$ by an IMP method with different amounts were also prepared, and Fig.6 shows that the modification by the IMP method gave lower activity to $CO_2$ reduction. And the activity cannot be increased by change the calcination temperature (Fig. 7).

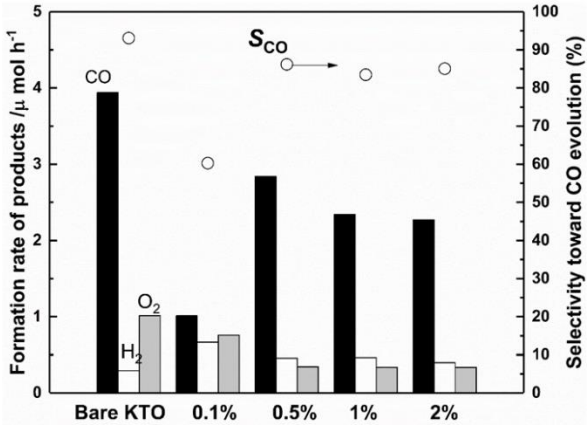


**Fig. 6** Formation rates of CO (black bar), $H_2$ (white bar), and $O_2$ (gray bar) and the selectivity to CO ($S_{CO}$%, open circles) in the photocatalytic reaction tests over the 1 wt% Ag/KTO modified with $Ca^{2+}$ ion by an IMP method (873K).

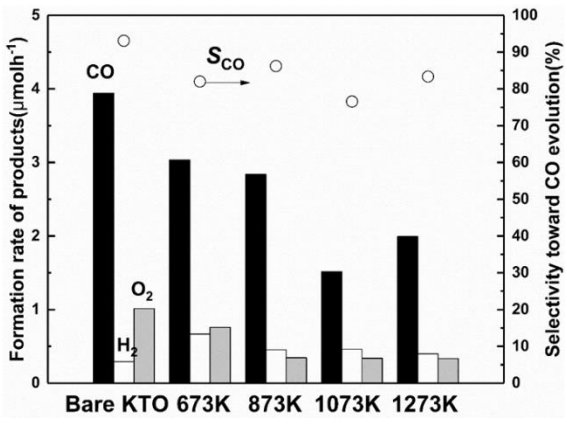


**Fig. 7** Formation rates of CO (black bar), $H_2$ (white bar), and $O_2$ (gray bar) and the selectivity to CO ($S_{CO}$%, open circles) in the photocatalytic reaction tests over the 1 wt% Ag/KTO modified with $Ca^{2+}$ ion by an IMP method calcined at different temperature.

The XRD patterns of prepared samples were shown in Fig.8, and the KTO patterns were clearly

showing of the samples doped with the $Ca^{2+}$ ion varies from 0.1 mol% and 50 mol%. No visible impurity pattern was observed in current XRD patterns measured by scanning mode.

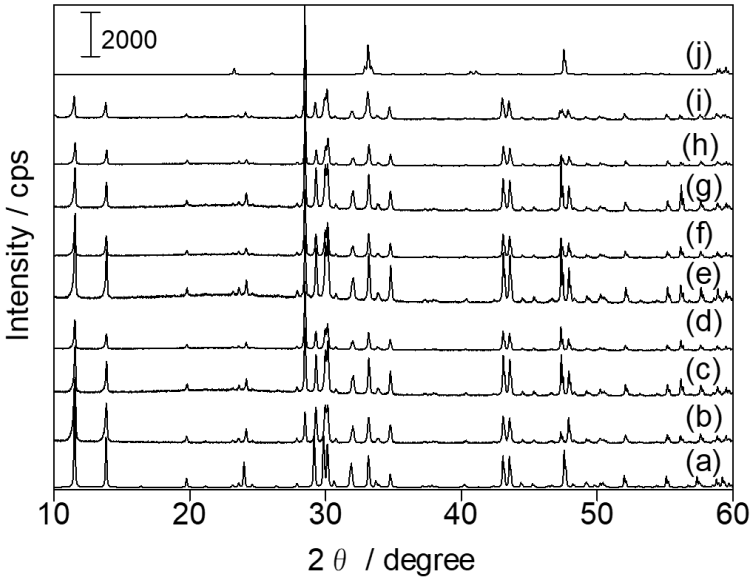


**Fig. 8** XRD patterns of prepared KTO:M doped with different amount of $Ca^{2+}$ by a flux mediate method, (a) ICSD#25712# for KTO, (b)bare KTO, (c)0.1 mol%, (d)0.5 mol%, (e)2 mol%, (f)5 mol%, (g)10 mol%, (h)20 mol%, (i)50 mol%, (j) ICSD#16688# for $CaTiO_3$.

The XRD patterns measured via step by step are shown in Fig.9, some impurity patterns and shift were observed. A new peak was observed around 28.5º over $Ca^{2+}$ ions doped sample, which may be due to the $Ca_2Ti_3O_7$ contamination, and a new peak corresponded to $CaTiO_3$ patterns at 39.2º was observed over the KTO: Ca (50%) sample. Also, the peak shifted were observed for all samples around 34.7º. All of these results indicated that the $Ca^{2+}$ ions should be inserted into the lattices of the KTO sample.

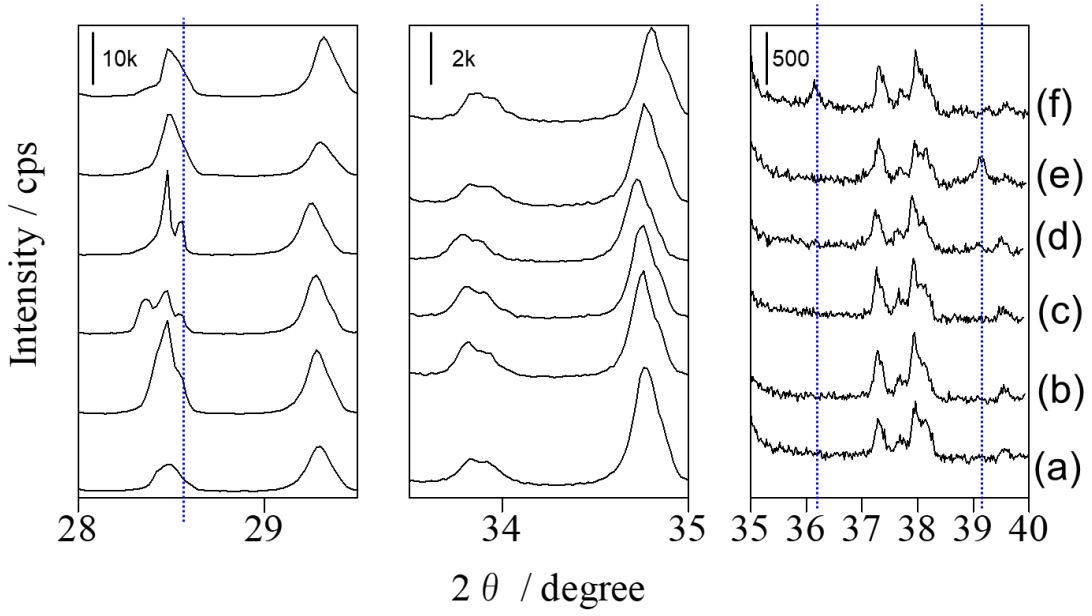


**Fig. 9** XRD patterns of prepared KTO:Ca samples, (a) bare KTO, (b)0.1 mol%, (c)0.5 mol%, (d)10 mol%, (e)50 mol%, (f)KTO_Ca(2 mol%).

In Fig. 10, the red shifted was observed over the samples doped with $Ca^{2+}$ ions with the amount from 0.1 mol% to 5 mol%, this shift should be caused by the addition of $Ca^{2+}$ ions, and lead to the enhancement of the photocatalytic activity of $CO_2$ reduction.

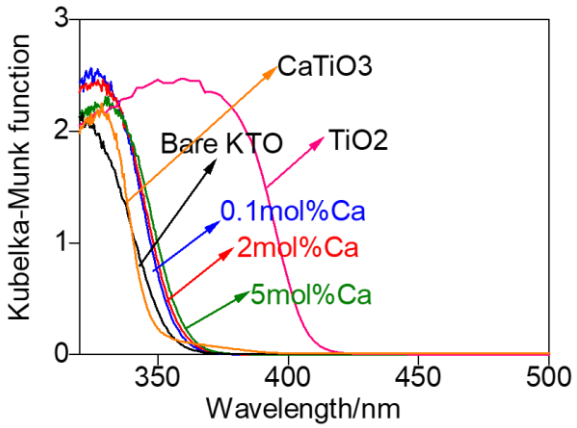


**Fig. 10** DR UV-Vis spectra of prepared KTO samples.

Since $Zr^{4+}$ ion addition exhibited higher activity for CO evolution, further optimization was carried out (Fig. 11). It was revealed that the addition of $Zr^{4+}$ enhanced CO evolution, when the added amount is in the range of 0.5 mol%-5 mol%, and the 0.5 mol% added sample exhibited the highest activity toward the CO evolution. But neither XRD patterns measured via

step by step mode shows no difference between the samples, nor does the DR UV-vis spectra. One possible reason could be that the addition of new metal ion can cause some defects, and these defects can trap the holes and electrons and slow down the recombination rate of holes and electrons. Also, further study should be conducted to clarify the effect of $Zr^{4+}$ ions.

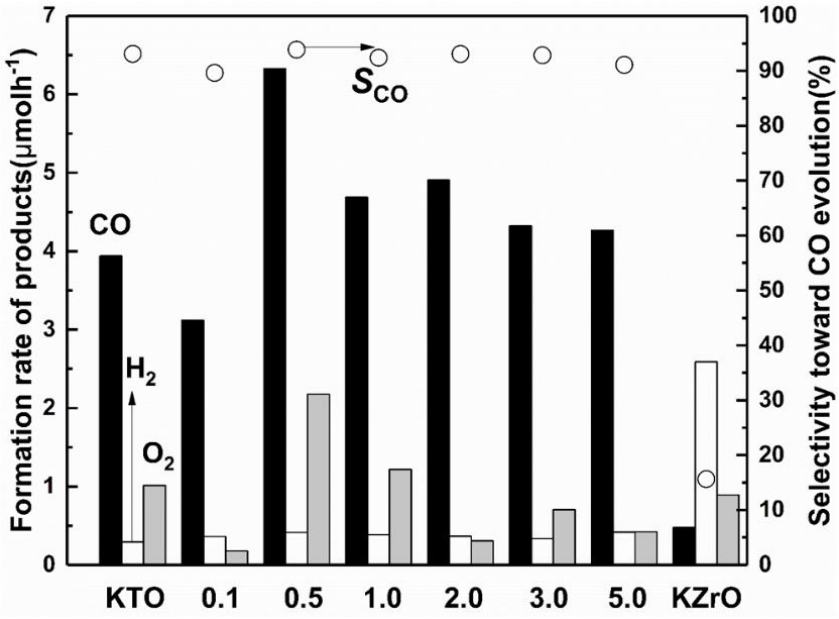


**Fig. 11** Formation rates of CO (black bar), $H_2$ (white bar), and $O_2$ (gray bar) and the selectivity to CO ($S_{CO}$%, open circles) in the photocatalytic reaction tests over the 1 wt% Ag/KTO:Zr(0.1–5 mol%) and K*x*Zr*y*O*z* samples.

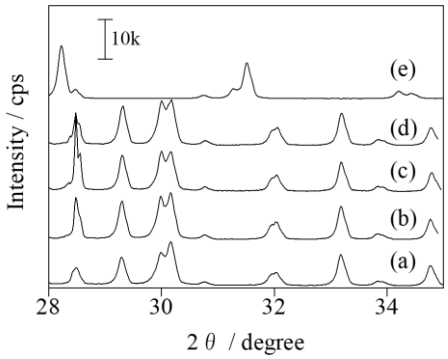


**Fig. 12** XRD patterns of prepared KTO:Zr samples, (a) bare KTO, (b)0.5 mol%, (c)2 mol%, (d)5 mol%, (e) K*x*Zr*y*O*z*.

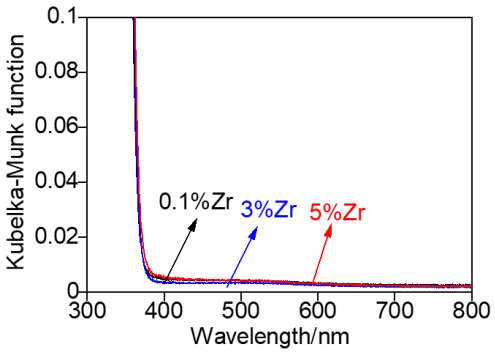


**Fig. 13** DR UV-Vis spectra of prepared KTO:Zr samples.

## 6-3.3 KTO samples prepared via a SSR method

The fabrication method plays a key role in the structure and activity of photocatalysts. Thus, in this study, several Ag-loaded cation-doped KTO photocatalysts were prepared via a SSR method as well, and they were examined for the photocatalytic $CO_2$ reduction with $H_2O$. Among the 1 wt% Ag-loaded samples doped with a metal ion (3 mol%), Among all tested samples, Ag/KTO-Rb, Ag/KTO-Cs and Ag/KTO-Zr samples showed higher photocatalytic activity toward the production of CO with high selectivity than Ag-loaded bare KTO. And the Ag/KTO-Rb exhibited the highest activity toward CO evolution (Fig. 14).

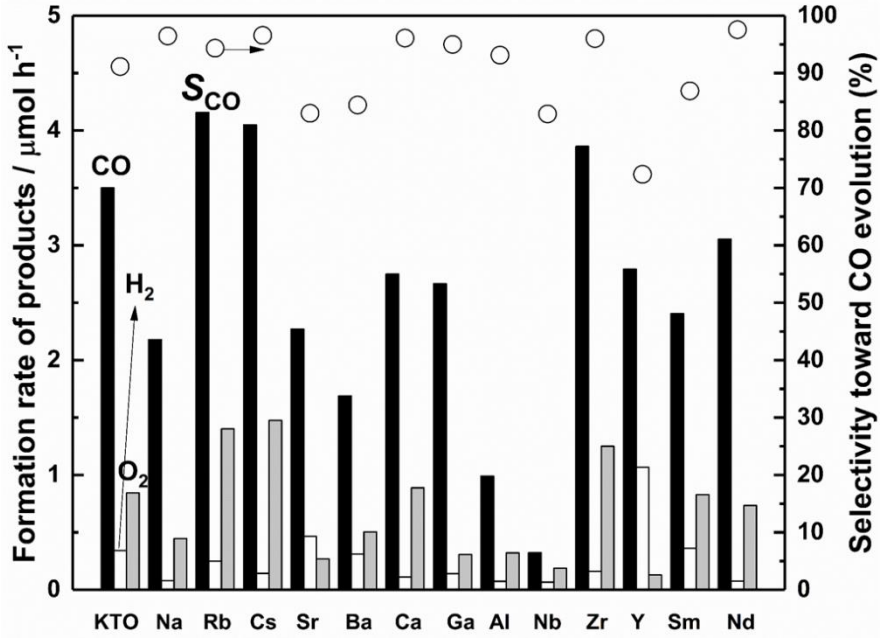


**Fig. 14** Formation rates of CO (black bar), $H_2$ (white bar), and $O_2$ (gray bar) and the CO selectivity ($S_{CO}$%, open circles) in the photocatalytic reaction tests over the Ag/KTO-M(3 mol%) samples prepared by a SSR method.

Besides, the cation doping amount much influenced the photocatalytic performance. As shown in Fig. 15, among a series of Ag/KTO-Rb samples with different doping amounts, Ag/KTO-Rb (1 mol%) sample showed the highest activity, which was 1.4 times higher than bare KTO with a high CO selectivity (91.4%).

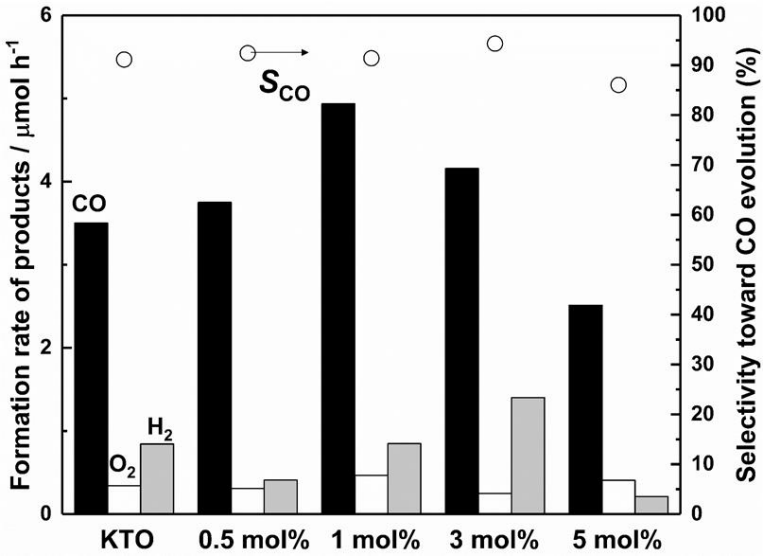


**Fig. 15** Formation rates of CO (black bar), $H_2$ (white bar), and $O_2$ (gray bar) and the CO selectivity ($S_{CO}$%, open circles) in the photocatalytic reaction tests over the 1 wt%Ag/KTO-Rb samples prepared by a SSR method with different amount of Rb.

XRD patterns (Fig. 16) and UV spectra (Fig. 17) measurements suggested that Rb-loaded KTO samples prepared successfully via a SSR method. That is, $Rb^+$ cation (163 pm) substituted to $K^+$ cation (155 pm) in the KTO crystals without forming the impurity phase, and successfully modified the structure of the KTO microcrystals.

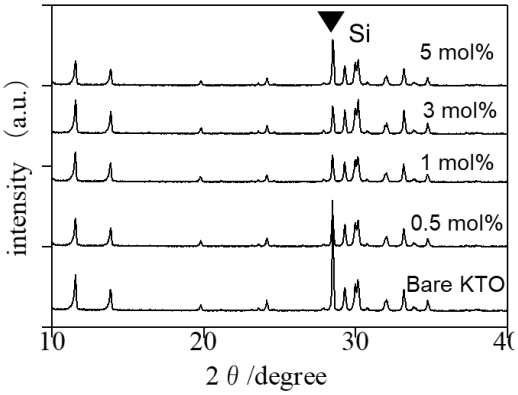


**Fig. 16** XRD patterns of the KTO-Rb samples prepared by a SSR method with different amount of Rb.

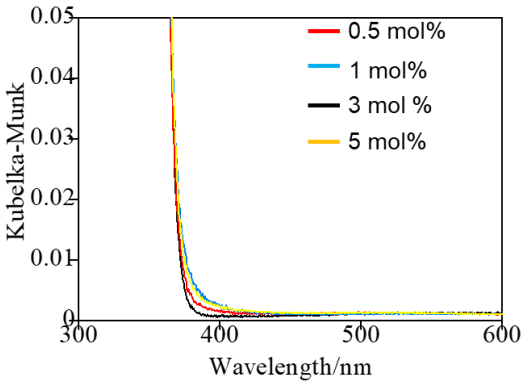


**Fig. 17** DR UV-vis spectra of the KTO-Rb samples prepared by a SSR method with different amount of Rb.

In SEM images (Fig. 18), both the bare KTO and KTO-Rb samples predominantly consisted of rod-like particles with some amorphous particles. And all the Rb-KTO particles' sizes are bigger than bare KTO with similar surface areas listed in Table 2.

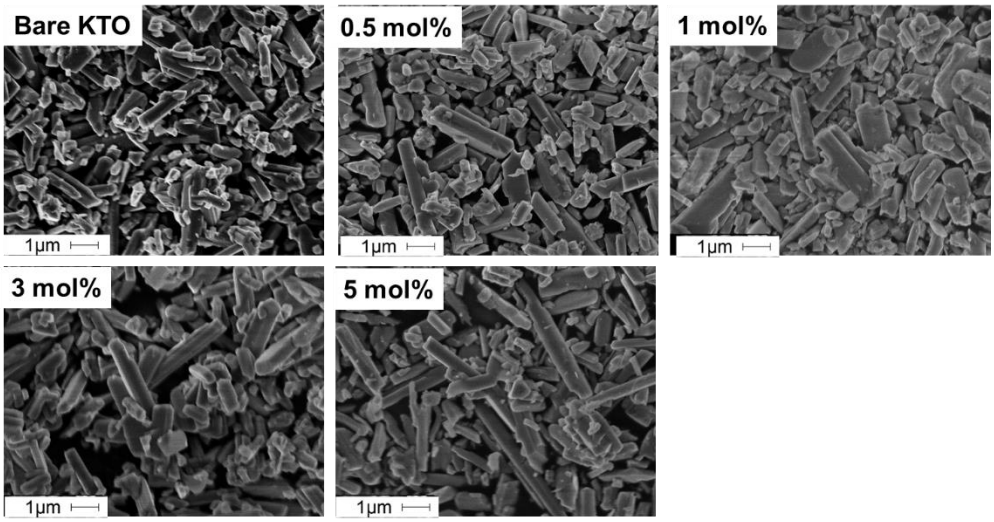


**Fig. 18** SEM images of the KTO-Rb samples prepared by a SSR method with different amount of Rb.

**Table 2** The specific surface area of the KTO:Rb samples and formation rate of CO over 1wt%Ag/KTO:Rb samples.

| Dopant (Rb) | Specific surface area($m^2/g$) | Production rate of CO(μmol/h) |
|---|---|---|
| Bare KTO | 2.93 | 3.50 |
| 0.5 mol% | 2.84 | 3.75 |
| 1 mol% | 2.81 | 4.94 |
| 3 mol% | 2.66 | 4.16 |
| 5 mol% | 2.86 | 2.51 |

## 6-3.4 Some other photocatalyst.

Some other photocatalysts(Fig. 20 a-e) were also prepared by a SSR method. For the $TiO_2$@$K_2Ti_6O_{13}$ sample, 1 g KTO was dispersed uniformly in 100 ml alcohol, mixed with 0.30 ml concentrated ammonia solution (28 wt%) under ultrasound for 15 min. Subsequently, 0.50 ml tetrabutyl titanate($Ti(OC_4H_9)_4$) was added to the suspension dropwise. The reactions were carried out at 40◦C for 24 h under continuous stirring. The products were washed by alcohol and deionized water several times, dried at 100◦C in an oven overnight and annealed at 500◦C in air for 2 h to remove the organic species and improve crystallinity.[42]

In Fig. 19, it was found that the morphology of these samples was quite different from each other, and activity shown in Fig. 20 for $CO_2$ reduction is lower than the Ag loaded KTO samples. This result indicated that the rod-like particles are beneficial to the CO evolution in this system.

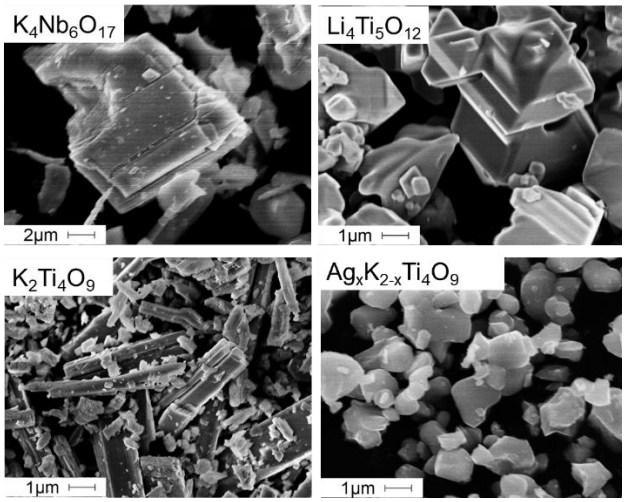


**Fig. 19** SEM image of four prepared photocatalyst.

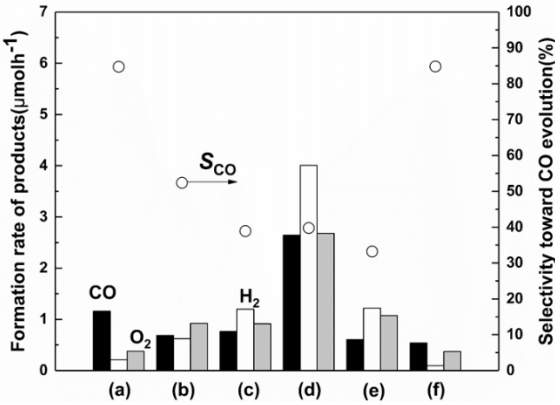


**Fig. 20** Formation rates of CO (balck bar), $H_2$ (white bar), and $O_2$ (grey bar) and the $S_{CO}$ evolution (open circles) in the photocatalytic reaction tests over the 1 wt% Ag loaded samples. (a) $K_2Ti_4O_9$, (b) $Ag_xK_{2-x}Ti_4O_9$, (c) $Li_4Ti_5O_{12}$, (d) $K_4Nb_6O_{17}$, (e) $KTaO_3$, (f)$TiO_2$@$K_2Ti_6O_{13}$, where 1wt% Ag cocatalyst was loaded.

## 6-4 Conclusion

In this study, KTO samples modified by an IMP method, a flux mediate method and a SSR method, it was found that surface modification by an IMP method was not effective for enhancement of $CO_2$ reduction in the current study. While for the flux mediate method, which is possible to insert the metal ion into the lattices of KTO bulk, only $Sn^{4+}$ and $Zr^{4+}$ ions improved the activity for photocatalytic $CO_2$ reduction selectively to CO by water. Further optimization revealed that a tiny addition of $Ca^{2+}$ such as 0.1 mol% most enhanced CO evolution, the improvement of $CO_2$ adsorption could be one reason for improvement of photocatalytic activity. Besides, the Rb-loaded KTO samples prepared successfully via a SSR method were proved to improve the photocatalytic activity. It was concluded that $Rb^+$ cation substituted to $K^+$ cation in the KTO crystals without forming impurity phase, and successfully modified the structure of the KTO microcrystals.

# Reference


1 J. Low, B. Cheng and J. Yu, *Appl. Surf. Sci.*, 2017, **392**, 658–686.

2 J. L. White, M. F. Baruch, J. E. Pander, Y. Hu, I. C. Fortmeyer, J. E. Park, T. Zhang, K. Liao, J. Gu, Y. Yan, T. W. Shaw, E. Abelev and A. B. Bocarsly, *Chem. Rev.*, 2015, **115**, 12888–12935.

3 J. Low, J. Yu and W. Ho, *J. Phys. Chem. Lett.*, 2015, **6**, 4244–4251.

4 B. Kumar, M. Llorente, J. Froehlich, T. Dang, A. Sathrum and C. P. Kubiak, *Annu. Rev. Phys. Chem.*, 2012, **63**, 541–569.

5 X. Chang, T. Wang and J. Gong, *Energy Environ. Sci.*, 2016, **9**, 2177–2196.

6 H. Mistry, A. S. Varela, C. S. Bonifacio, I. Zegkinoglou, I. Sinev, Y. W. Choi, K. Kisslinger, E. A. Stach, J. C. Yang, P. Strasser and B. R. Cuenya, *Nat. Commun.*, 2016, **7**, 1–8.

7 M. Asadi, K. Kim, C. Liu, A. V. Addepalli, P. Abbasi, P. Yasaei, P. Phillips, A. Behranginia, J. M. Cerrato, R. Haasch, P. Zapol, B. Kumar, R. F. Klie, J. Abiade, L. A. Curtiss and A. Salehi-Khojin, *Science (80-. ).*, 2016, **353**, 467–470.

8 K. Li, X. An, K. H. Park, M. Khraisheh and J. Tang, *Catal. Today*, 2014, **224**, 3–12.

9 O. Ola and M. M. Maroto-Valer, *J. Photochem. Photobiol. C Photochem. Rev.*, 2015, **24**, 16–42.

10 K. Iizuka, T. Wato, Y. Miseki, K. Saito and A. Kudo, *J. Am. Chem. Soc.*, 2011, **133**, 20863–20868.

11 R. Pang, K. Teramura, H. Asakura, S. Hosokawa and T. Tanaka, *Appl. Catal. B Environ.*, 2017, **218**, 770–778.

12 S. Iguchi, K. Teramura, S. Hosokawa and T. Tanaka, *Catal. Sci. Technol.*, 2016, **6**, 4978–4985.

13 T. Takayama, K. Tanabe, K. Saito, A. Iwase and A. Kudo, *Phys. Chem. Chem. Phys.*, 2014, **16**, 24417–24422.

14 Z. Wang, K. Teramura, Z. Huang, S. Hosokawa, Y. Sakata and T. Tanaka, *Catal. Sci. Technol.*, 2016, **6**, 1025–1032.

15 H. Nakanishi, K. Iizuka, T. Takayama, A. Iwase and A. Kudo, *ChemSusChem*, 2017, **10**, 112–118.

16 R. Pang, K. Teramura, H. Tatsumi, H. Asakura, S. Hosokawa and T. Tanaka, *Chem.*

*Commun.*, 2018, **54**, 1053–1056.

17 K. Teramura, Z. Wang, S. Hosokawa, Y. Sakata and T. Tanaka, *Chem. - A Eur. J.*, 2014, **20**, 9906–9909.

18 X. Zhu, A. Anzai, A. Yamamoto and H. Yoshida, *Appl. Catal. B Environ.*, 2019, **243**, 47–56.

19 T. Takayama, K. Tanabe, K. Saito, A. Iwase and A. Kudo, *Phys. Chem. Chem. Phys.*, 2014, **16**, 24417–24422.

20 H. Tatsumi, K. Teramura, Z. Huang, Z. Wang, H. Asakura, S. Hosokawa and T. Tanaka, *Langmuir*, 2017, **33**, 13929–13935.

21 Y. Sakata, Y. Matsuda, T. Nakagawa, R. Yasunaga, H. Imamura and K. Teramura, *ChemSusChem*, 2011, **4**, 181–184.

22 R. Pang, K. Teramura, H. Tatsumi, H. Asakura, S. Hosokawa and T. Tanaka, *Chem. Commun.*, 2018, **54**, 1053–1056.

23 S. Iguchi, Y. Hasegawa, K. Teramura, S. Kidera, S. Kikkawa, S. Hosokawa, H. Asakura and T. Tanaka, *Sustain. Energy Fuels*, 2017, **1**, 1740–1747.

24 Z. Wang, K. Teramura, S. Hosokawa and T. Tanaka, *J. Mater. Chem. A*, 2015, **3**, 11313–11319.

25 A. Anzai, N. Fukuo, A. Yamamoto and H. Yoshida, *Catal. Commun.*, 2017, **100**, 134–138.

26 R. Pang, K. Teramura, H. Asakura, S. Hosokawa and T. Tanaka, *ACS Appl. Energy Mater.*, 2019, **2**, 5397–5405.

27 X. ZHU, A. Yamamoto, S. Imai, A. Tanaka, H. Kominami and H. Yoshida, *Chem. Commun.*, , DOI:10.1039/c9cc06038c.

28 T. Xiong, W. Cen, Y. Zhang and F. Dong, *ACS Catal.*, 2016, **6**, 2462–2472.

29 S. Tonda, S. Kumar, S. Kandula and V. Shanker, *J. Mater. Chem. A*, 2014, **2**, 6772–6780.

30 Y. Zheng, L. Lin, B. Wang and X. Wang, *Angew. Chemie - Int. Ed.*, 2015, **54**, 12868–12884.

31 S. Yoshizawa, Z. Huang, K. Teramura, H. Asakura, S. Hosokawa and T. Tanaka, *ACS Appl. Mater. Interfaces*, 2019, **11**, 37875–37884.

32 J. Luo, S. Zhang, M. Sun, L. Yang, S. Luo and J. C. Crittenden, *ACS Nano*, 2019, **13**, 9811–9840.

33 S. Xie, Y. Wang, Q. Zhang, W. Deng and Y. Wang, *ACS Catal.*, 2014, **4**, 3644–3653.

34 S. J. He, X. Y. Chen, S. M. Shang, J. Shen and C. F. Guo, *Russ. J. Appl. Chem.*, 2016, **89**,

1520–1527.

35 H. Yoshida, M. Takeuchi, M. Sato, L. Zhang, T. Teshima and M. G. Chaskar, *Catal. Today*, 2014, **232**, 158–164.

36 C. Liu, H. Yin, Y. Liu, M. Ren, A. Wang, C. Ge, H. Yao, H. Feng, J. Chen and T. Jiang, *Mater. Res. Bull.*, 2009, **44**, 1173–1178.

37 A. Iwase, H. Kato and A. Kudo, *ChemSusChem*, 2009, **2**, 873–877.

38 H. Yoshida, M. Sato, N. Fukuo, L. Zhang, T. Yoshida, Y. Yamamoto, T. Morikawa, T. Kajino, M. Sakano, T. Sekito, S. Matsumoto and H. Hirata, *Catal. Today*, 2018, **303**, 296–304.

39 E. A. Davis and N. F. Mott, *Philos. Mag.*, 1970, **22**, 903–922.

40 Y. Sakata, T. Hayashi, R. Yasunaga, N. Yanaga and H. Imamura, *Chem. Commun.*, 2015, **51**, 12935–12938.

41 Y. Sakata, Y. Miyoshi, T. Maeda, K. Ishikiriyama, Y. Yamazaki, H. Imamura, Y. Ham, T. Hisatomi, J. Kubota, A. Yamakata and K. Domen, *Appl. Catal. A Gen.*, 2016, **521**, 227–232.

42 X. Zhou, D. Zhong, H. Luo, J. Pan and D. Zhang, *Appl. Surf. Sci.*, 2018, **427**, 1183–1192.

# Chapter 7 General Summary

In this thesis, the author focused on deveolping high active and selectivity photocatalytic conversion of $CO_2$ with $H_2O$ over alkila hexatitanate by optimimization of preparation condition, dual cocatalysts and surface modification. It was found that the crystal stucture, morphology, the different cocatalyst, the stucture of dual cocatalyst and surface modification have great effect on the photocatalytic reduction of $CO_2$ with $H_2O$. The general conclusion of this thesis is as follows:

In chapter 2, two remained problems in the previous work, one of which is low activity toward CO evolution and low selectivity, and the other is nonstoichiometric $O_2$ evolution, were much improved and explained, respectively. First, it was found that the Ag/NTO sample, with 1.0 wt% of Ag cocatalyst loaded by a photodeposition method, exhibited the highest CO production rate (4.6 μmol $h^{-1}$) and the highest CO selectivity (74%) among the examined samples in the current reaction conditions. These values are more than 29 times higher production rate and more than 2.7 times higher selectivity than those obtained in the previous study, which would originate from the optimization of the photocatalyst and the improved reaction conditions. In addition, among three Ag/NTO samples, on which 1.0 wt% of the Ag cocatalyst nanoparticles were loaded by different methods, the Ag/NTO sample provided by the PD method gave the highest activity and selectivity for $CO_2$ reduction. Since the PD method tends to form the metallic Ag nanoparticles on the reductive facets of the rod-like NTO crystals, which can efficiently promote the CO evolution. Second, although the evolution rate of $O_2$ was not enough in the induction period, it increased with time and reached to the stoichiometric formation ratio of the oxidative and reductive products after a long time, such as 24 or 50 h, depending on the samples. Furthermore, it was confirmed that the chloride residues and the photoadsorption of $O_2$ on the surface are responsible for the insufficient $O_2$ evolution less than stoichiometric ratio among the products at the initial period.

In chapter 3, after comparing four types of alkali titanates, the further development of potassium hexatitanate photocatalyst prepared in the flux method was examined. KTO

samples prepared with different ratios of KCl flux gave quite different morphology of crystals, and the KTO sample prepared with 70% KCl consisting of rod-like particles showed higher activity than the others. With the increase of holding temperature, both the length and size of KTO particles increased, and when the holding temperature was at 1523 K and higher or holding time is less than 5 h, $TiO_2$ particles were observed as an impurity phase in SEM images, which gave negative effect on the photocatalytic activity of the $CO_2$ reduction. As a result, the Ag/KTO sample consisting of the suitable size of rod-like KTO crystals prepared at 1273 K with holding time of 10 h gave the highest activity for CO evolution and the highest selectivity toward CO (96%), which is superior to the $Na_2Ti_6O_{13}$ catalyst of similar rod-like structure. In addition, although the $Na_2Ti_6O_{13}$ catalyst showed a long induction period to produce oxygen with enough production rate compared to that expected from the production rates of CO and $H_2$ in our previous study, the KTO sample produced expected amount of $O_2$ after only a shorter induction period, i.e., the ratio of $e^-/h^+$ became close to 1 after 4 h.

In chapter 4, it was found that the KTO sample loaded with both Ag metal and manganese oxide species such as Ag(0.5)-Mn(0.13)/KTO samples exhibited the highest activity (10 μmol $h^{-1}$) and the highest selectivity ($S_{CO}$=98%) with the stoichiometric production ratio of the oxidative and reductive products, which showed almost 2 times higher CO production rate than the Ag(1.0)/KTO sample. The $MnO_x$ cocatalyst can enhance the the $O_2$ evolution, which leads to the improvement of CO evolution with synergistic effect of Ag cocatalyst. Here, the dual cocatalyst, i.e., the combination of Ag and $MnO_x$ species, simultaneously contribute to the reductive and oxidative reactions, respectively, realized the photocatalytic $CO_2$ reduction to CO with a higher reaction rate and a higher selectivity such as 98%.

In chapter 5, the different deposition methods for loading dual cocatalysts were investigated to figure out the relationship between the $MnO_x$ and Ag cocatalyst. It was found that the core-shell structure of dual cocatalyst inhibits the activity towards $CO_2$ reduction, and the suitable particle size of Ag cocatalyst is necessary to support the reaction occurrence on the surface of the photocatalyst. And the addition of dual cocatalyst by a simultaneous method can maintain nanoparticle size of Ag cocatalyst and deposited Ag and $MnO_x$ cocatalyst on the long facets and short facets separately, which indicated the reductive facets and oxidative facets respectively.

In chapter 6, In this study, KTO samples modified by an IMP method, a flux mediate method and a SSR method, it was found that surface modification by an IMP method was not effective for enhancement of $CO_2$ reduction in the current study. While for the flux mediate method, which is possible to insert the metal ion into the lattices of KTO bulk, only $Sn^{4+}$ and $Zr^{4+}$ ions improved the activity for photocatalytic $CO_2$ reduction selectively to CO by water. Further optimization revealed that a tiny addition of $Ca^{2+}$ such as 0.1 mol% most enhanced CO evolution, the improvement of $CO_2$ adsorption could be one reason for improvement of photocatalytic activity. Besides, the Rb-loaded KTO samples prepared successfully via a SSR method were proved to improve the photocatalytic activity. It was concluded that $Rb^{+}$ cation substituted to $K^{+}$ cation in the KTO crystals without forming impurity phase, and successfully modified the structure of the KTO microcrystals.

In summary, the photocatalytic activity of reduction of $CO_2$ with $H_2O$ photocatalyst were proved to be related to the crystal stucture, morphology, the different cocatalyst, the stucture of dual cocatalyst and surface modification. The photocatalyst with suitable stucture such as nano rod-like particles, loading with the suitable amount of cocatalyst by suitable method such as Ag cocatalyst loade by PD method, proper combination of dual cocatalyst such as $MnO_x$-Ag cocatalyst, and suitable doptant or surface modification were shown to enhance the photocatalytic activity for $CO_2$ reduction with $H_2O$. Moreover, it should be noted that the formation rate of products deeply depends on the reaction conditions including reactor design, the employed lamp and so on. It is somewhat difficult to explain the correlation between the reaction conditions and the formation rate by a simple equation. The present comprehensive study has provided some solutions to improve both the CO evolution and the $S_{CO}$ over the alkali hexatitanate samples, and it is hopeful that these solutions can be applied into other photocatalyst in future.

# List of Publication

## Chapter 2

1. Silver-loaded sodium titanate photocatalysts for selective reduction of carbon dioxide to carbon monoxide with water.

**Xing. Zhu**, A. Anzai, Akira. Yamamoto, Hisao. Yoshida, *Appl. Catal. B*, 243 (2019) 47-56.

## Chapter 4

2. A silver–manganese dual co-catalyst for selective reduction of carbon dioxide into carbon monoxide over a potassium hexatitanate photocatalyst with water.

**Xing Zhu**, Akira Yamamoto, Shota Imai, Atsuhiro Tanaka, Hiroshi Kominami and Hisao Yoshida, *Chemical Communications*, 2019, 55, 13514—13517.

## Chapter 3

3. Enhancement of selective reduction carbon dioxide with water by controlling the shape of potassium hexatitanate by a flux method.

**Xing. Zhu**, Akira. Yamamoto, Hisao. Yoshida.

*To be submitted.*

## Chapter 5

4. Facet-selective deposition of a bifunctional silver-manganese cocatalyst on potassium hexatitanate photocatalyst for selective photocatalytic reduction of carbon dioxide by water.

**Xing Zhu**, Akira Yamamoto, Shota Imai, Atsuhiro Tanaka, Hiroshi Kominami and Hisao Yoshida.

*To be submitted.*

## Chapter 6

5. Modification of silver-loaded potassium titanate photocatalyst by adding metal ions for carbon dioxide reduction with water

**Xing. Zhu**, Akira. Yamamoto, Hisao. Yoshida.

*To be submitted.*

***Other pubilicaton as a co-author***

5. Photodeposition conditions of silver cocatalyst on titanium oxide photocatalyst directing product selectivity in photocatalytic reduction of carbon dioxide with water.

Ahmed Hammad, Akihiko Anzai, **Xing Zhu**, Akira Yamamoto, Daiki Ootsuki, Teppei Yoshida, Ahmed EL-Shazly, Marwa Elkady and Hisao Yoshida. *Catalysis Letters*, accepted. [DOI: 10.1007/s10562-019-02997-z].

## Attended Conferences

1. **(Poster)** ○ Xing Zhu, Akira Yamamoto, Shota Imai, Atsuhiro Tanaka, Hiroshi Kominami and Hisao Yoshida. A silver-manganese dual cocatalyst for selective carbon dioxide reduction into carbon monoxide over potassium hexatitanate photocatalyst with water. OKCAT2019, 2019.10.25-26. Osaka(Japan), No.PS-03.

2. **(Oral)** ○ Xing Zhu, Akira Yamamoto, Shota Imai, Atsuhiro Tanaka, Hiroshi Kominami and Hisao Yoshida. Enhancement of CO evolution over $K_2Ti_6O_{13}$ by loading $MnO_x$/Ag dual catalysts for the photocatalytic reduction of $CO_2$ with $H_2O$**.** EuropaCat2019, 2019.08.18-23. Aachen(Germany).

3. **(Oral)** ○ Xing Zhu, Akira Yamamoto, Shota Imai, Atsuhiro Tanaka, Hiroshi Kominami and Hisao Yoshida. Modification of silver-loaded potassium titanate photocatalyst by adding metal ions for carbon dioxide reduction with water. 第 124 回触媒討論会, 2019.09.18-22. Nagasaki(Japan), No.2D12.

4. **(Oral)** ○ Xing Zhu, Akira Yamamoto, Shota Imai, Atsuhiro Tanaka, Hiroshi Kominami and Hisao Yoshida. A silver-manganese oxide dual cocatalyst for selective reduction of carbon dioxide to carbon monoxide with water over potassium hexatitanate photocatalyst. 第 17 回触媒化学ワークショップ姫路, 2019.07.25-27. Kimeji(Japan), No.C01.

5. **(Poster)**○Xing Zhu, Akira Yamamoto and Hisao Yoshida. Modification of silver-loaded potassium titanate photocatalyst by adding metal ions for carbon dioxide reduction with water. 第 38 回光がかかわる触媒化学シンポジウム, 2019.06.30. Nagoya(Japan), No.PS-10.

6. **(Poster)** ◯Xing Zhu, Akihiko Anzai, Akira Yamamoto, Hisao Yoshida, Optimization of silver-loaded sodium titanate photocatalyst for the reduction of carbon dioxide with water. TOCAT8, 2018.08.05-10, Yokohama(Japan), No.PS-3106.

7. **(Oral)** ◯Xing Zhu, Akira Yamamoto, Hisao Yoshida, Potassium hexatitanate rod-like crystals prepared by a flux method for photocatalytic reduction of $CO_2$ with water. 第 37 回光がかかわる触媒化学シンポジウム, 2018.07.06, kinki(Japan), No. G06.

8. **(Oral)** ◯Xing Zhu, Akira Yamamoto, Hisao Yoshida, Synthesis and characteristics of potassium hexatitanate by a flux method and its photocatalytic performance of $CO_2$ reduction with water. 第 16 回触媒化学ワークショップ, 2018.09.23-25, Hokaido(Japan), No. A-04.

9. **(Oral)** ◯Xing Zhu, Akira Yamamoto, Hisao Yoshida, Potassium hexatitanate prepared by a flux method for photocatalytic reduction of $CO_2$ with water. 第 122 回触媒討論会, 2018.09.26-28 Hokaido(Japan), No. 1G08.

10. **(Poster)** ◯Xing Zhu, Akira Yamamoto, Hisao Yoshida. Enhancement of CO evolution over $K_2Ti_6O_{13}$ by loading MnOx/Ag dual catalysts for the photocatalytic reduction of $CO_2$ by $H_2O$. 第 123 回触媒討論会 2019.03.20-21, Osaka(Japan), No. 2P-62.

11. **(Oral)** ◯Zhu Xing, Akira Yamamoto, Hisao Yoshida. Optimization of silver-loaded sodium titanate photocatalyst for the reduction of carbon dioxide with water. 日本化学会第 98 春季年会, 2018.03.20-23, Tukuba(Japan), No. 1C1-56.

12. **(Oral)** ◯Xing Zhu, Akira Yamamoto, Hisao Yoshida. Photocatalytic conversion of $CO_2$ by water over Ag-modified $Na_2Ti_6O_{13}$. 第 36 回固体・表面光化学討論会, 2017.11.21-22, Shiga(Japan), No. 107.

13. **(Poster)** ◯Xing Zhu, Akira Yamamoto, Hisao Yoshida. Photoreduction of carbon dioxide with water over Ag-modified $Na_2Ti_6O_{13}$. OKCAT2017, 2017.10.27-28, Osaka(Japan), No. PS-9.

14. **(Poster)** ◯Xing Zhu, Akira Yamamoto, Hisao Yoshida. Sodium hexatitanate photocatalysts prepared by a flux method for reduction of carbon dioxide with water. 第 15 回触媒化学ワークショップ, 2017.07.31-08.02, Takaoka (Japan), No. PS-18.

# Copyright（著作権等）

1. Silver-loaded sodium titanate photocatalysts for selective reduction of carbon dioxide to carbon monoxide with water (Applied Catalysis B: Environmental, 2019,243, 47-56.) [DOI: 10.1016/j.apcatb.2018.10.021]

2. A silver-manganese dual cocatalyst for selective reduction of carbon dioxide into carbon monoxide over a potassium hexatitanate photocatalyst with water (Chemical Communications,2019, 55, 13514-13517.) [DOI: 10.1039/c9cc06038c]